UNIVERSITAT POLITÈCNICA
DE CATALUNYA
BARCELONATECH

Analysis of Q factor degradation mechanisms in BAW resonators

Carlos Udaondo Guerrero

ADVERTIMENT La consulta d'aquesta tesi queda condicionada a l'acceptació de les següents condicions d'ús: La difusió d'aquesta tesi per mitjà del repositori institucional UPCommons (http://upcommons.upc.edu/tesis) i el repositori cooperatiu TDX (http://www.tdx.cat/) ha estat autoritzada pels titulars dels drets de propietat intel·lectual **únicament per a usos privats** emmarcats en activitats d'investigació i docència. No s'autoritza la seva reproducció amb finalitats de lucre ni la seva difusió i posada a disposició des d'un lloc aliè al servei UPCommons o TDX. No s'autoritza la presentació del seu contingut en una finestra o marc aliè a UPCommons (*framing*). Aquesta reserva de drets afecta tant al resum de presentació de la tesi com als seus continguts. En la utilització o cita de parts de la tesi és obligat indicar el nom de la persona autora.

ADVERTENCIA La consulta de esta tesis queda condicionada a la aceptación de las siguientes condiciones de uso: La difusión de esta tesis por medio del repositorio institucional UPCommons (http://upcommons.upc.edu/tesis) y el repositorio cooperativo TDR (http://www.tdx.cat/?locale- attribute=es) ha sido autorizada por los titulares de los derechos de propiedad intelectual **únicamente para usos privados enmarcados** en actividades de investigación y docencia. No se autoriza su reproducción con finalidades de lucro ni su difusión y puesta a disposición desde un sitio ajeno al servicio UPCommons No se autoriza la presentación de su contenido en una ventana o marco ajeno a UPCommons (*framing)*. Esta reserva de derechos afecta tanto al resumen de presentación de la tesis como a sus contenidos. En la utilización o cita de partes de la tesis es obligado indicar el nombre de la persona autora.

WARNING On having consulted this thesis you're accepting the following use conditions: Spreading this thesis by the institutional repository UPCommons (http://upcommons.upc.edu/tesis) and the cooperative repository TDX (http://www.tdx.cat/?locale- attribute=en) has been authorized by the titular of the intellectual property rights **only for private uses** placed in investigation and teaching activities. Reproduction with lucrative aims is not authorized neither its spreading nor availability from a site foreign to the UPCommons service. Introducing its content in a window or frame foreign to the UPCommons service is not authorized (framing). These rights affect to the presentation summary of the thesis as well as to its contents. In the using or citation of parts of the thesis it's obliged to indicate the name of the author.

UNIVERSITAT POLITÈCNICA DE CATALUNYA

SIGNAL THEORY AND COMMUNICATIONS DEPARTMENT

ESCOLA D'ENGINYERIA DE TELECOMUNICACIÓ I AEROESPACIAL
DE CASTELLDEFELS

Ph.D. Thesis

Analysis of Q Factor Degradation Mechanisms in BAW Resonators

---

Author
Carlos UDAONDO GUERRERO

Supervisors
Prof. Juan Carlos COLLADO GÓMEZ
Prof. Jordi MATEU MATEU

COMPONENTS AND SYSTEMS FOR COMMUNICATIONS (CSC)
RESEARCH GROUP

UNIVERSITAT POLITÈCNICA DE CATALUNYA
BARCELONATECH
Departament de Teoria del Senyal
i Comunicacions

March 19, 2024

Contents

Acronyms **6**

List of figures **7**

1 Introduction **17**
- 1.1 Context . . . 17
- 1.2 Electroacoustic resonators . . . 17
- 1.3 BAW devices' state of the art . . . 19
- 1.4 Statement of contributions . . . 21

2 BAW Devices **22**
- 2.1 Fundamentals of electro-acoustic BAW devices . . . 22
- 2.2 Electric Impedance . . . 25
- 2.3 Effective electromechanical coupling . . . 27
- 2.4 Losses on BAW resonators . . . 30
  - 2.4.1 Sources of losses . . . 30
  - 2.4.2 Q factor of a resonator . . . 31
- 2.5 BAW models . . . 32
  - 2.5.1 Butterworth van Dyke (BvD) model . . . 32
  - 2.5.2 Mason model . . . 33
- 2.6 Summary . . . 35

3 Modeling Lamb Waves on BAW Resonators **36**
- 3.1 Lamb waves on BAW resonators . . . 37
  - 3.1.1 The main operating mode . . . 40
  - 3.1.2 Suppression methods . . . 43
- 3.2 BvD multi-branch . . . 46
- 3.3 Mason based models . . . 46
  - 3.3.1 Lateral transmission line . . . 47
  - 3.3.2 BR modes on SMR . . . 49
- 3.4 2nd Harmonic Emissions on BAW Resonators Exhibiting Lateral Spurious Resonances . . . 56

3.4.1 Nonlinear constitutive relations 56
3.4.2 Nonlinear Mason model 57
3.4.3 Devices and linear measurements 58
3.5 Nonlinear measurements 59
3.6 The Transmission Line Matrix (TLM) method 62
3.6.1 Quasi-2D model 62
3.6.2 Quasi-3D model 66
3.6.3 BAW resonators with Border Ring 76
3.7 Conclusions 85

4 Thermoelastic Damping Model **87**
4.1 Thermo-electro-mechanical behavior of BAW resonators 87
4.1.1 Relation between temperature coefficient of stress an linear thermal expansion 89
4.1.2 Thermoelastic damping in BAW resonators 89
4.2 Mason based model for TED 91
4.2.1 Non-piezoelectric layers 92
4.2.2 Piezoelectric layer 93
4.2.3 Thermal network 93
4.2.4 Model implementation 95
4.3 Calculation of the temperature coefficient of the stress 97
4.4 TED model on an AlN piezolayer 97
4.4.1 Effect of the room temperature and the coefficient of thermal expansion 97
4.4.2 Effect of the heat capacity 98
4.4.3 Effect of the thermal conductivity 98
4.5 Temperature dependence of the BAW resonator 99
4.5.1 Thermal expansion and material density 99
4.5.2 Temperature dependence of the piezoelectric constant 101
4.5.3 Temperature dependence of the electric permittivity 101
4.5.4 Temperature dependence of the heat capacity 101
4.5.5 Temperature dependence of the thermal conductivity 103
4.6 Temperature measurements of BAW resonators 105
4.6.1 Q factor degradation due to Bragg reflector 110
4.6.2 Q factor degradation due to thermoelastic damping (TED) . . 113
4.7 TED on the outband spurious resonances 116
4.7.1 Fitting of the spurious resonances 119
4.8 Conclusions 126

5 Conclusions and Future Work **127**
5.1 Future work 129

6 List of Author's Contributions **130**

6.1 Journals & Symposia Publications 130
6.2 Student works related to the research activities 131

Bibliography **132**

A Calculation of the temperature coefficient of stress by the thermal expansion **138**

B Temperature coefficient of stress on different class crystals **140**

Acronyms

4G fourth-Generation.
5G fifth-Generation.

ADS Advanced Design System.

BAW Bulk Acoustic Wave.
BR Border Ring.
BvD Butterworth-Van Dyke model.

CA Carrier Aggregation.

DoF Degrees of Freedom.

FBAR Film Bulk Acoustic Resonator.
FEM Finite Element Method.
FFT Fast Fourier Transform.

H2 Second Harmonic.

L Longitudinal acoustic waves.

MIMO Multiple-Input Multiple-Output.

NIST National Institute of Standards and Technology.

Q Quality Factor.

RF Radio-Frequency.

SAW Surface Acoustic Wave.
SMR Solidly Mounted Resonator.

TE Thickness Extensional.
TED Thermoelastic Damping.
TLM Transmission Line Matrix.
TS Thickness Shear.
TV Transverse Vertical acoustic waves.

VNA Vector Network Analyser.

List of Figures

1.1 BAW and SAW resonators. In the middle an equivalent circuital model for electroacoustic resonators. [4]. 16
1.2 (a) FBAR resonator. (b) SMR resonator. 17

2.1 Mechanical resonances on a plate of thickness $2d$. The stress fields associated with the resonances are plotted. [3]. 21
2.2 Magnitude (continuous line) and phase (dotted line) of the impedance of a resonator. The electromechanical coupling 26
2.3 Geometry of a resonator with electrodes of thickness t of the same material of the piezolayer. The stress field is shown with a solid line and the displacement with a dashed line [3]. 27
2.4 Geometry of a resonator with electrodes of thickness t with the acoustic impedance of the electrodes higher than the one of the piezolayer. The stress field is shown with a solid line and the displacement with a dashed line [3]. 27
2.5 Kelvin-Voigt model for viscous damping. 29
2.6 BvD model with a motional arm for the fundamental mode. [3] 31
2.7 mBvD model with a motional arm for the fundamental mode. [3] . . 31
2.8 T-network modeling an acoustic transmission line [3]. 32
2.9 Mason model. Below it can be seen its implementation for a multi-layer resonator. On the left it represents a stress free boundary (acoustic short) and on the right a thin substrate layer modeled by a load [3]. . 33

3.1 L and TV waves on a plate. When each of these incident waves arrives to a free surface, generates two reflected L and TV waves [13]. 35
3.2 Isotropic plate. 36
3.3 Symmetric and asymmetric modes of a Lamb wave [36]. 37
3.4 Dispersion curves on a plate. Symmetric modes are shown in grey, while asymmetric ones in black [37] 38

3.5 Nomenclature of the Lamb modes depending in its thickness standing wave pattern. The arrows show the displacement (u_i) directions on the plate's thickness, indicated by its subscript. The number of half-wavelengths is represented by the continuous line. 39
3.6 Dispersion curves of a ZNO piezoelectric plate exhibiting type I dispersion 39
3.7 (a) 2D BAW resonator. (b) Dispersion curves of the active and inactive regions. 40
3.8 2D BAW resonator exhibiting high spurious modes. The plot corresponds to a 2D FEM simulation of a ZnO membrane with a thickness of 1.74 μm, and a lateral dimension of 80 μm. Magnitude (continuous line) and phase (dotted line) of the impedance of a resonator. 42
3.9 (a) 2D BAW resonator with Border Ring. (b) Dispersion curves of the active, the inactive, and the Border Ring regions. 43
3.10 2D BAW resonator with Border Ring. The plot corresponds to a 2D FEM simulation of a ZnO membrane with a thickness of 1.74 μm, a lateral dimension of 80 μm, and a BR width of 7.5 μm. Magnitude (continuous line) and phase (dotted line) of the impedance of a resonator. 43
3.11 BvD equivalent circuit with a motional branch for each spurious resonance [3]. 44
3.12 Circuit model of a lateral transmission line for each physical direction connected to a conventional Mason model. 46
3.13 Input impedance of a ZnO rectangular resonator. Results of 3D FEM simulation are plotted in dotted blue line. The results of the circuit model are plotted in continuous black line [30]. 47
3.14 Different BR modes depending of the BR width (from 5.5 µm to 6.5 µm). 48
3.15 FEM simulation of a SMR. The displacement field on the thickness direction is shown. 49
3.16 Circuital model for the BR modes. The dispersion curves correspondents to each lateral transmission line section are shown on top. . . . 50
3.17 Phase of the input impedance of FEM simulated SMR (dotted traces), and adjustment of our model (solid traces). Blue traces correspond to a BR width of 5.5 µm, while red to 10.5 µm. 51
3.18 Phase of the input impedance of the two measured square resonators. 52
3.19 Phase of the input impedance of the two measured rectangular resonators. 53
3.20 Equivalent nonlinear lateral Mason model for the piezoelectric layer [55] 56
3.21 Stack configuration of the measured SMR-BAW devices [49] 57
3.22 Phase of the input impedance of R1 and R2. Measurements correspond to the red line, while simulation to the dashed blue line. 58
3.23 H2 measurement and simulation of R1 and R2. Measurements correspond to the red line, while simulation to the dashed blue line. 59

3.24 Two-dimensional resonator in the xz-plane. The x-dimension is discretized in N_x elements. 60
3.25 Equivalent Π-network of a dispersive transmission line in the x-direction 61
3.26 Magnitude and phase of the Impedance of the 2D FEM ZnO resonator (blue), and the Quasi-2D model (red). 63
3.27 Magnitude and phase of the Impedance of the 2D FEM AlN SMR resonator (blue), and the Quasi-2D model (red). 64
3.28 Equivalent Π-network of a dispersive transmission line on the x and y direction. Four nodes interconnected by different direction transmission lines are shown. 65
3.29 Schematic of a TLM mesh for a square resonator. The lateral dimensions a and b, and the number of discretizations in each direction (N_x and N_y) are indicated. 66
3.30 Magnitude and phase of the Impedance of the 3D FEM ZnO square resonator (blue), and the Quasi-3D model (red). 67
3.31 Magnitude and phase of the Impedance of the 3D FEM ZnO rectangular resonator (blue), and the Quasi-3D model (red). 68
3.32 Standing wave pattern of $|v_z|$ at the frequency of mode 311 and 131 in the square resonator. 69
3.33 Standing wave pattern of $|v_z|$ at the frequency of mode 311 in the rectangular resonator. 70
3.34 Magnitude and phase of the Impedance of the 3D FEM ZnO trapezoidal resonator (blue), and the Quasi-3D model (red). 70
3.35 Standing wave pattern of normalized $|v_z|$ for the first four resonant modes of the trapezoidal resonator. 71
3.36 Magnitude and phase of the Impedance of the measured square SMR (A=6400 μm^2) (blue), and the Quasi-3D model (red). 73
3.37 Magnitude and phase of the Impedance of the measured square SMR (A=12900 μm^2) (blue), and the Quasi-3D model (red). 73
3.38 Magnitude and phase of the Impedance of the measured rectangular SMR (A=6400 μm^2) (blue), and the Quasi-3D model (red). 74
3.39 Magnitude and phase of the Impedance of the measured rectangular SMR (A=12900 μm^2) (blue), and the Quasi-3D model (red). 74
3.40 Two-dimensional resonator in the xz-plane. The x-dimension is discretized in N_x elements. 75
3.41 Dispersive curves of the non-active region. 76
3.42 Magnitude and phase of the Impedance of the 2D FEM ZnO resonator (blue), and the Quasi-2D model (red). 77
3.43 Magnitude and phase of the Impedance of the 2D FEM ZnO with a BR of 7.5 µm (red). 78
3.44 Magnitude and phase of the Impedance of the 2D FEM ZnO with a BR of 10 µm (red). 78

3.45 Magnitude and phase of the Impedance of the 2D FEM ZnO with a BR of 12.5 µm (red). 79
3.46 Magnitude and phase of the Impedance of the 3D FEM ZnO square resonator (red). 80
3.47 Magnitude and phase of the Impedance of the 3D FEM ZnO square resonator with 7.5 μm BR (red). 81
3.48 Magnitude and phase of the Impedance of the 3D FEM ZnO rectangular resonator with 7.5 μm BR (red). 82
3.49 Magnitude and phase of the Impedance of the 3D FEM ZnO square resonator with 10 μm BR (red). 82
3.50 Magnitude and phase of the Impedance of the 3D FEM ZnO rectangular resonator with 10 μm BR (red). 83

4.1 Heckmann diagram showing the interaction between the intensive variables (T, E, and Θ), and the extensive ones (S, D, and σ) [18]. . . . 86
4.2 Longitudinal wave, the changes of temperature (Θ) at the compressed and expanded regions are illustrated [3]. 88
4.3 Block diagram of a piezoelectric cell coupled to the thermal network. For the thermoelastic damping case: $\Delta T = -\lambda d\Theta$ [18]. 90
4.4 Lumped transmission line model for acoustic waves with an added VCVS for modeling the TED [18]. 91
4.5 Lumped Mason model for the piezolayer with an added VCVS for modeling the TED [18]. 92
4.6 Implemented thermal network. The current source $Q_{\Delta z}$ models the current added to the mode [18]. 92
4.7 Block diagram that illustrates the circuit implementation of three layers of the BAW resonator. Each layer is constructed as a cascade of electro-thermo-mechanical cells. The electric losses are implemented as lumped resistors and their dissipated heat is coupled to the thermal domain [18]. 93
4.8 Piezoelectric cell showing the connection between the lumped Mason model and the thermal network. 94
4.9 The left plot shows the resonant frequency at different ambient temperatures. The right plot shows the maximum Q factor at different ambient temperatures. 95
4.10 The left plot shows the resonant frequency at different coefficient of thermal expansion α_3. The right plot shows the maximum Q factor at different coefficient of thermal expansion α_3. 96
4.11 The left plot shows the resonant frequency at different heat capacities C_v. The right plot shows the maximum Q factor at different heat capacities C_v. 96

4.12 The left plot shows the resonant frequency at different thermal conductivities k. The right plot shows the maximum Q factor at different thermal conductivities k. 97
4.13 Plots of the impedance of a BAW resonator. The magenta trace corresponds to the Mason model of a resonator at room temperature. Both red and blue traces are superposed, blue is the impedance at 100 K taking into account thermal expansion, and red taking into account the substrate clamping. 98
4.14 Impedance of a BAW resonator, blue trace is the impedance at room temperature, while the red one is the impedance at 100 K taking only into account the change of mass density. 98
4.15 Impedance of a BAW resonator, blue trace is the impedance at room temperature, while the red one is the impedance at 100 K taking only into account the temperature derivative of the piezoelectric constant. 99
4.16 Impedance of a BAW resonator, blue trace is the impedance at room temperature, while the red one is the impedance at 100 K taking only into account the temperature derivative of the electric permittivity. . 100
4.17 Heat capacity in function of the normalized temperature. 100
4.18 Thermal conductivity of different metals in function of temperature [59]. 102
4.19 Measurement setup at NIST. It can be seen a fragment of the wafer and the Cascade Microtech probe in blue. 103
4.20 Cross section of the series resonator SBO400, and the shunt resonator PBO400. The proportions of the figures are not on scale, and only intended for illustrative purposes. 104
4.21 Plot of the narrowband measured magnitude of the PBO400 impedance. The different traces correspond to measurements done from 100K to 298K 105
4.22 Plot of the narrowband measured phase of the PBO400 impedance. The different traces correspond to measurements done from 100K to 298K. 105
4.23 Plotted broadband measurements of the PBO400 impedance. The different traces correspond to measurements done from 100K to 298K. . 106
4.24 Plot of the narrowband measured magnitude of the SBO400 impedance. The different traces correspond to measurements done from 100K to 298K 106
4.25 Plot of the narrowband measured phase of the SBO400 impedance. The different traces correspond to measurements done from 100K to 298K. 107
4.26 Plotted broadband measurements of the SBO400 impedance. The different traces correspond to measurements done from 100K to 298K. . 107
4.27 108
4.28 Mason model for the PBO400 resonator implemented on ADS. 109

4.29 Q factor at different temperatures of the PBO400 resonator. Red traces correspond to the measurements, while blue traces to the simulations. Crosses stand for resonances and diamonds for antiresonances. 110
4.30 Implementation of the TED model on ADS. 111
4.31 Q factor at different temperatures of the PBO400 resonator. Red traces correspond to the measurements, while blue traces to the TED simulations. Crosses stand for resonances and diamonds for antiresonances. 112
4.32 Measurements (red) versus simulated TED model (blue) plots of the magnitude (right) and the phase (blue) of the impedance at 100 K. . 112
4.33 Adjustments of the heat capacity (right) and the thermal conductivity (left) of AlN layer in PBO400 on blue, in red it is plotted its linear regression. 113
4.34 Q factor at different temperatures of the SBO400 resonator. Red traces correspond to the measurements, while blue traces to the TED simulations. Crosses stand for resonances and diamonds for antiresonances. 113
4.35 Phase of the impedance of a BAW resonator. The spurious resonances can be seen as spikes above the fundamental resonance at about 1.8 GHz115
4.36 Circuit model of a RLC resonator. 116
4.37 Fitting of the Q circle for a spurious resonance. The extracted Q values can be seen on the inset. 116
4.38 Phase of the impedance of the PBO400 resonator at high frequencies. 118
4.39 Phase of the impedance of the SBO400 resonator at high frequencies. 120
4.40 Fitting of the Q circle. The measurement can be seen in blue, the RLC fitting is shown in yellow. 121
4.41 Phase of the impedance of the B30 resonator at high frequencies. . . 122

Abstract

The emergence of smartphones not only changed the way people uses its phone for, but it also changed the traffic amount that networks need to carry, increasing the demand of higher data rates. The overall result was the appearance of fourth-Generation (4G) networks, and nowadays, the current development of fifth-Generation (5G), implying the need for more frequency bands, and the application of new techniques such as Carrier Aggregation (CA), Multiple-Input Multiple-Output (MIMO) antennas, and so on. All these market driven necessities suppose a great challenge for the Radio-Frequency (RF) industry, which have been facing the necessity of miniaturization and band coexistence on its devices since the beginning of mobile communications.

Microwave filters based on Bulk Acoustic Wave (BAW) resonators, have been able to this day to overcome these limitations. These devices consist in a thin piezoelectric layer comprised by two metal electrodes, and an acoustic confinement method, which can be simply made of air or a Bragg reflector. The use of electroacoustic technology enables to reduce the filter size up to five orders of magnitude, allowing the integration of multiple filters in handsets. This thesis focuses on modeling some of different physical phenomena at the resonator level that affect the performance of the filters.

The first part of this thesis is the one regarding the spurious response of BAW resonators. This response is originated by acoustic waves traveling in the lateral dimension of the resonator. These waves couple electromechanically, degrading the filter response. BAW filters have been capable of overcoming this limitation suppressing them by the use of different electrode geometries (Apodization), or by surrounding the electrode by a decreased, or increased frame (Border Ring (BR)). The nature of these waves is studied through the thesis and several equivalent models are proposed in order to accurately predict them, helping to the design of the correspondent suppression structures.

One of this thesis contributions regarding the lateral spurious resonances, consists in making use of a modified Mason model to determine the origin of the additional spurious resonances generated by the BR. These resonances can be attributed to an acoustic mode, different from the fundamental, propagating across the resonator stack. By adding nonlinear sources to that model, the Second Harmonic (H2)

emissions and the impact of the spurious resonances in them, is also studied.

Finally, a new equivalent model based in the Transmission Line Matrix (TLM) method is proposed for the acoustic cavity of a BAW resonator. This new approach is able to model resonators with different electrode geometries, in a much faster way than traditionally used methods like the Finite Element Method (FEM). In addition, by determining different propagation regions, it can be used to model both the apodization and the Border Ring at the same time.

The second family of contributions are the ones regarding to the thermoelastic behavior of the BAW resonators. A solid heats up when compressed and vice versa. In a harmonic oscillation, when heat is able to flow through the solid regions, this flow from hotter to colder regions generates a relaxation of the acoustic wave. This is the Thermoelastic Damping (TED). A thermo-electro-mechanical Mason model is used for quantifying this source of losses on BAW resonators. The model is compared with experimental data taken at cryogenic temperatures and an analysis of losses of the broadband spurious resonances of the Bragg reflector has been performed.

Resumen

La emergencia de los teléfonos inteligentes no solo cambió la forma en que las personas usan sus teléfonos, sino que también modificó la cantidad de tráfico que las redes deben manejar, aumentando la demanda de tasas de datos más altas. El resultado general fue la aparición de las redes 4G y, en la actualidad, el desarrollo actual de las redes 5G, lo que implica la necesidad de más bandas de frecuencia y la aplicación de nuevas técnicas como la Carrier Agregation (CA), antenas MIMO, etc... Todas estas necesidades impulsadas por el mercado suponen un gran desafío para la industria de Radiofrecuencia (RF), que ha enfrentado la necesidad de miniaturización y coexistencia de bandas en sus dispositivos desde el inicio de las comunicaciones móviles.

Los filtros de microondas basados en resonadores de Onda Acústica de Volumen (BAW, por sus siglas en inglés) han logrado hasta el día de hoy superar estas limitaciones. Estos dispositivos consisten en una delgada capa piezoeléctrica compuesta por dos electrodos metálicos y un método de confinamiento acústico, que puede ser simplemente aire o un reflector de Bragg. El uso de tecnología electroacústica permite reducir el tamaño del filtro hasta en cinco órdenes de magnitud, lo que permite la integración de múltiples filtros en dispositivos móviles. Esta tesis se centra en modelar los diferentes comportamientos físicos a nivel de resonador que afectan el rendimiento de los filtros.

La primera parte de esta tesis se refiere a la respuesta espuria de los resonadores BAW. Esta respuesta es originada por ondas acústicas que viajan en la dimensión lateral del resonador. Estas ondas se acoplan electromecánicamente, degradando la respuesta del filtro. Los filtros BAW han sido capaces de superar esta limitación suprimiéndolos mediante el uso de diferentes geometrías en los electrodos (apodización), o rodeando el electrodo con un marco de grosor reducido o aumentado (Border Ring). La naturaleza de estas ondas se estudia a lo largo de la tesis y se proponen varios modelos equivalentes para predecirlas con precisión y diseñar las correspondientes estructuras de supresión.

Una de las contribuciones de esta tesis con respecto a las resonancias espurias laterales consiste en utilizar un modelo de Mason modificado para determinar el

origen de las resonancias espurias adicionales generadas por el Border Ring. Estas resonancias pueden atribuirse a un modo acústico, diferente del fundamental, que se propaga a través del conjunto del resonador. Al agregar fuentes no lineales a ese modelo, también se estudian las emisiones del segundo armónico (H2, por sus siglas en inglés) y el impacto de las resonancias espurias en ellas.

Finalmente, se propone un nuevo modelo equivalente basado en el método de la Matriz de Línea de Transmisión (TLM, por sus siglas en inglés) para la cavidad acústica de un resonador BAW. Este nuevo enfoque puede modelar resonadores con diferentes geometrías de electrodos de manera mucho más rápida que los métodos tradicionalmente utilizados como el Método de Elementos Finitos (FEM, por sus siglas en inglés). Además, al determinar diferentes regiones de propagación, puede utilizarse para modelar tanto la apodización como el Border Ring al mismo tiempo.

La segunda familia de contribuciones se refiere al comportamiento termoelástico del resonador BAW. Un sólido se calienta cuando se comprime y viceversa. En una oscilación armónica, cuando el calor puede fluir a través de las regiones del sólido, este flujo de regiones más calientes a más frías genera una relajación de la onda acústica que se conoce como amortiguamiento termoelástico. En esta tesis de describe la utilización de un modelo Mason termo-electro-mecánico para cuantificar esta fuente de pérdidas en resonadores BAW. El modelo se compara con datos experimentales tomados a temperaturas criogénicas y con un análisis de pérdidas de las resonancias espurias fuera de banda originadas en el reflector de Bragg.

Chapter 1

Introduction

1.1 Context

The emergence of smartphones not only changed the way people uses its phone for, but it also changed the traffic amount that networks need to carry, increasing the demand of higher data rates. The overall result was the appearance of 4th Generation (4G) networks, and nowadays, the current development of 5th Generation (5G), implying the need for more frequency bands, and the application of new techniques such as Carrier Aggregation (CA), Multiple-Input Multiple-Output (MIMO) antennas, and so on. All these market driven necessities suppose a great challenge for the Radio-Frequency (RF) industry, which have been facing the necessity of miniaturization and band coexistence on its devices since the beginning of mobile communications.

Microwave filters for mobile applications have been one of the most affected components by the stringent specifications imposed by the 4G and 5G standards. But it is not only the necessity of a better performance, due to the increase of bands, the number of resonators needed is increasing up to a hundred per handset, being the size of the filters a critical factor on their design [1].

Two decades ago, the size of an overall ceramic based duplexer was about 20 mm long per 5 mm wide [2], it is clear to see that ceramic filters became too big to fit into an actual RF front end. The solution was in the electroacoustic technology, based in the conversion of the electromagnetic wave into an acoustic one by the piezoelectric effect, the use of this filters allow us to reduce their size by about 5 orders of magnitude.

1.2 Electroacoustic resonators

The first candidates from the electroacoustic family to substitute the ceramic filters, were the Surface Acoustic Wave (SAW) filters developed in the 60s. They are based on a surface propagated acoustic wave excited by interdigital transducers. SAW filters offer acceptable Quality Factor (Q) values at a reduced size, but when going up the 3 GHz operational frequency, their performance decreases drastically. Another alternative for the SAW filters is the Bulk Acoustic Wave (BAW) technology, developed in the late 90s and based on a thickness propagated wave in a piezolayer between two parallel electrodes. BAW filters offered better Q values, and higher power handling on higher operational frequency, albeit they have a higher manufacturing cost [3]. On Fig.1.1 a BAW resonator and a SAW resonator can be seen.

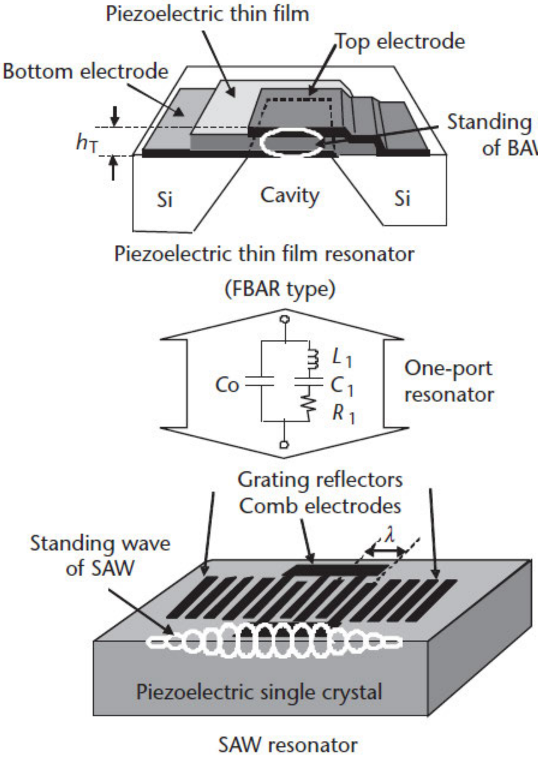

Figure 1.1: BAW and SAW resonators. In the middle an equivalent circuital model for electroacoustic resonators. [4].

For these reasons, coexistence of these two electroacoustic technologies is common on the mobile phone scenario. Although, the needs to go up in frequency and to achieve high performing filters due 5G networks, puts BAW technology in an interesting place, with the need to overcome the performance degradation that arises from the more pronounced edge effects (such as spurious modes, lateral leakage...), and an at least linear increase in acoustic losses [5].

BAW filters are composed of several BAW resonators disposed in different topologies. The resonators can be electrically coupled (ladder, lattice...), or acoustically coupled (Stacked Crystal Filter, Coupled Resonator Filter...). Selecting one or other topology allow us to overcome some flaws on the resonator design, but to ensure the best functioning of the overall filter, the BAW resonator itself is of major concern.

The first work on thin film BAW resonators made of AlN was done by Lakin in the 80s [6], and set the basis for the resonators used today. It was followed by the development of Film Bulk Acoustic Resonator (FBAR) and Solidly Mounted Resonator (SMR). The main difference between the FBAR and the SMR is the wave confinement method. FBAR resonators use an air cavity between the bottom electrode and the substrate(Figure 1.2a), while SMR use a Bragg reflector that acts as an acoustic mirror (Figure 1.2b).

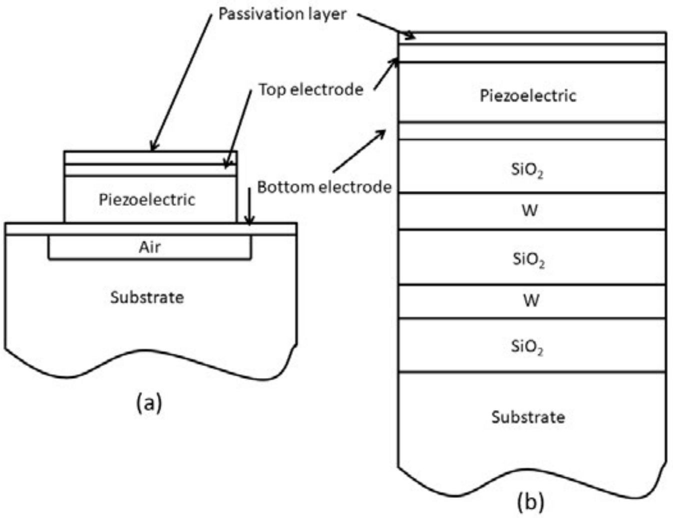

Figure 1.2: (a) FBAR resonator. (b) SMR resonator.

The electrical response of a resonator is quite similar for a FBAR and a SMR. Due to the different wave confinement method, FBAR presents better electromechanical coupling and Q factor, although SMRs present a better heat dissipation having more contact surface to the substrate [7].

1.3 BAW devices' state of the art

By the 2010s, BAW filters dominated the market for nearly all high end mobile devices [8]. BAW resonators of that time were exhibiting Q factors up to 4000.

Nowadays BAW resonators exist up to 8 GHz [9]. These BAW resonators performing at high frequencies for 5G and WiFi6E networks are facing new challenges related to their performance.

Since the thickness of the piezoelectric layer scales with $1/f$, in order to achieve the 50 Ω port impedances in the filters, the resonator´s area will scale in size with $1/f^2$ [5]. Reducing the resonator's area makes the resonator more prone to the spurious modes generated by the modes propagating along the lateral dimensions of the resonators. Another effect related to the area shrinking of the resonator is the increase of the electrode's edge to area ratio. BAW resonators with larger perimeters exhibit higher lateral leakage, these contributes to a decrease on the resonator's acoustic Qs [5].

To suppress these lateral spurious modes, a decreased or increased frame is deposited along the resonator's perimeter. This frame, the Border Ring (BR) is determined by the dispersive behavior of the laterally propagating modes. Due to the perimeter to area ratio increase, the spurious modes of this frame structure are becoming stronger [9].

The nonlinear behavior of BAW resonators has also been a matter of interest in recent years. The modeling of these effects is crucial to achieve linear filter responses. The generated harmonics and intermodulation products can generate interference signals that can desensitize the handset's receiver [10]. This effect becomes more important for devices using CA.

The shrinkage of the resonator's area also increases these undesired nonlinear effects. Smaller areas lead to worse power dissipation, and the nonlinear emissions of these more prominent lateral resonances become a problem if they are not correctly suppressed at the filter level. To suppress the Second Harmonic emissions (H2), two identical resonator's can be connected in antiparallel [11]. Although an slight mismatch in the two employed resonators can result in the H2 cancellation level degradation. The lateral spurious resonances can play a role on mismatches due to process variations.

Another performance characteristic of BAW resonators that is being degraded at higher operational frequencies is the Q factor due to acoustic damping. These losses are increasing at least linearly with frequency [5]. One of the loss mechanisms that is attracting the interests of BAW resonator designers is the thermoelastic damping (TED). This source of material damping is caused by the heat generated due to the propagating acoustic wave, and its propagation along the solid extracts energy from the vibration [12]. When the thickness of the resonator's layers is decreased, the thermal path is being also reduced. This reduction increases the losses due to the thermoelastic damping mechanism.

Modeling all these effects is becoming crucial to accurately design BAW resonators for the newly developed frequency bands.

1.4 Statement of contributions

This thesis is focused in modeling the physical behaviors that degenerate the performance of BAW resonators. It is centered on the acoustic physics of the resonator, the lateral modes propagating along the stack, and the loss mechanisms that occur and degrade the Q Factor.

The first group of contributions are the ones related to these lateral modes. Several models are proposed to explain the behavior of the so called Lamb waves. Based on a Mason circuital model with an added dispersive transmission line to model the lateral dimensions, several performance degradation effects are studied. The first one is related to the Border Ring (BR) resonances that appear on the electric impedance of an SMR. Here the modified Mason model is used to explain that effect. The other one studied with that model are the second harmonic emissions (H2) of an SMR. In order to do so, the modified Mason model is expanded with the nonlinear constitutive relations to model the effect of the laterally propagating modes on the H2 response of the resonator.

To improve the modeling capabilities, a model based on the Transmission Line Matrix (TLM) method was derived for modeling a BAW resonator in two dimensions. That model is later expanded for modeling a 3D resonator. These new models give an improvement on the BR modeling capabilities, and enable simulations of any in-plane geometry of the electrodes.

The second group of contributions are related to the thermoelastic damping. Thermoelastic damping is one of the loss mechanisms that take place on a BAW resonator. This damping mechanism is expected to grow with frequency, so it is one of the main concerns for resonators operating at the new above 5 GHz bands. In this work, the Mason model is modified with the electro-thermo-mechanical constitutive relations, that add the thermal domain to the resonator physics. This model is able to predict the heat propagation along the resonator layers and consequently modeling the thermoelastic effect.

The model is validated with electric measurements of resonators at cryogenic temperatures, showing a good explanation of the loss effects measured at that temperatures. Also a study of the different Bragg reflector layers resonances that appear on SMR resonators was done. The Q Factor for these resonances is not correctly predicted by traditional loss models such as viscoelasticity, and the thermoelastic damping model is able to give an explanation at a broad range of frequencies.

Chapter 2

BAW Devices

This chapter explains the basics of electroacoustic resonators, specifically the Bulk Acoustic Wave resonators. On the first section the basic physics undergoing into a BAW resonator are introduced to the reader. Here some concepts such as piezoelectricity and the resonator's input electrical impedance Z_{in} are presented.

The following sections introduce some of the electroacoustic resonator figures of merit, the electromechanical coupling and the Q factor. The first characterizing the electromechanical transduction of the device, and the later characterizing the losses on the resonator. A brief introduction to common loss mechanisms in BAW resonators is also given.

Finally, the two main circuital models for BAW resonators, the Butterworth-van Dyke and the Mason model, are derived and presented to the reader.

2.1 Fundamentals of electro-acoustic BAW devices

BAW resonators transform the electromagnetic wave into an acoustic wave confined in it. That conversion is possible by the piezoelectric effect, which transforms electrical energy into mechanical, and vice versa. In an acoustic wave propagating in a crystalline material like the ones used on BAW resonators, the propagation velocity is about five orders of magnitude lower than in electromagnetic waves, allowing to make that devices smaller.

As described in [3], let us consider a piezoelectric material plate of thickness $2d$, and infinitely thin electrodes located on the top and the bottom of the plate (Figure 2.1). Due to the piezoelectric effect, the electric field created between the electrodes generates an acoustic wave that propagates in the thickness of the plate. Supposing that the plate is situated in a vacuum medium, intuition tells us that the wave will be reflected at the interfaces since mechanical waves do not propagate on vacuum.

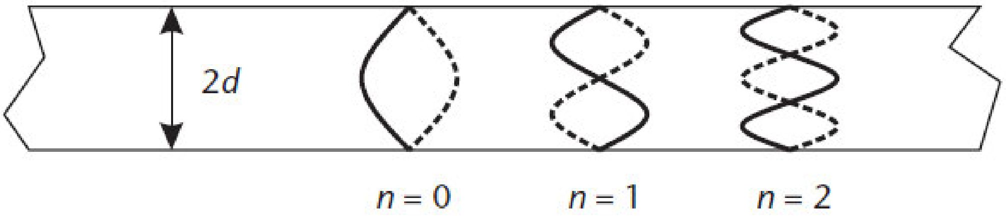

Figure 2.1: Mechanical resonances on a plate of thickness $2d$. The stress fields associated with the resonances are plotted. [3].

This structure will mechanically resonate when the incident and the reflected waves add up in phase somewhere within the structure. To achieve that, the plate thickness has to be a multiple of half-wavelengths at the resonance frequency. Considering the wave traveling with an acoustic velocity v, the mechanical resonance condition of the plate is

$$\omega_n = (n+1) \cdot \frac{\pi}{2} \cdot \frac{v}{d}, \quad n = 1, 2, 3... \tag{2.1}$$

where n represents each of the resonance modes corresponding to each multiple of half-wavelengths. From (2.1) we can notice that using a piezoelectric material like AlN to obtain a 2 GHz resonator a plate thickness of roughly 3 µm will be needed. That size is interesting for mobile phone manufacturers that are always struggling with a very limited space for the RF module.

The truth is that a piezoelectric driven resonator it is not going to behave like that. The previous case was a purely mechanical system that does not take into account the electric excitation of that waves. To understand the piezoelectric resonator nature, basic theories that govern piezoelectric resonators need to be described.

Piezoelectric materials due to its internal lattice symmetries, generate electric fields when deformed and vice versa. When a stress (T) is applied to the crystal an strain (S) is generated, this deformation will cause a change in polarization (P) due to ion displacements

$$P = (\chi_{ion} + \chi_e)E + eS, \tag{2.2}$$

where e is the piezoelectric constant, χ_{ion} and χ_e are the ion and the electronic susceptibility, E is the electric field, and S the strain. This polarization will generate changes on the electric displacement field (D) [13].

To derive the constitutive relations of the mechanical and electric domains, we will use of the variation of internal energy (U) in a piezoelectric solid taking only into account the z-direction [13]:

$$dU = \Theta d\sigma + T_3 dS_3 + E_3 dD_3 \tag{2.3}$$

here, Θ is the absolute temperature and σ the entropy. The subscripts indicate that all the fields are in the z-direction. Since we need σ, S_3 and E_3 as independent variables, the electric Gibbs potential ($G = U - E_3D_3 - \sigma\Theta$). Assuming entropy to remain constant ($d\sigma = 0$), the stress and the electric displacement of the piezoelectric solid can be calculated as

$$T_3 = \left(\frac{\partial G}{\partial S_3}\right)_E \quad \text{and} \quad D_3 = -\left(\frac{\partial G}{\partial E_3}\right)_S .$$

After some manipulation we arrive to the final constitutive relations:

$$\begin{aligned} T_3 &= c_{33}^E S_3 - e_{33}E_3 \\ D_3 &= e_{33}S_3 + \varepsilon_{33}^S E_3. \end{aligned} \tag{2.4}$$

Here the stiffness constant $c_{33}^E = (\partial T_3/\partial S_3)_E$, is introduced. Relating the rate of change of the stress due to strains. The electric permittivity $\varepsilon_{33}^S = (\partial D_3/\partial E_3)_S$, is the rate of change of the electric displacement fields due to variations of the electric fields. The superscripts indicate that the constants need to be evaluated under specific conditions (e. g. c^E indicates stiffness under a constant electric field), while the subscripts indicate the field direction.

The two domains are related by the piezoelectric effect. The first equation on (2.4) reflects the emergence of stress on a piezoelectric material caused by an external electric field, and they are related by the piezoelectric constant e_{33}. That is called the direct piezoelectric effect. The second one, reflects the inverse piezoelectric effect, relating how internal deformations contribute to the electric displacement, and is also related by e_{33}. Making use of the symmetry of second derivatives, it can be demonstrated that the piezoelectric constant is the same for the direct and the inverse piezoelectric effect:

$$\left(\frac{\partial^2 G}{\partial E_3 \partial S_3}\right) = \left(\frac{\partial T_3}{\partial E_3}\right)_S = -\left(\frac{\partial D_3}{\partial S_3}\right)_E = -e_{33}. \tag{2.5}$$

For simplicity, subscripts will be dropped off this chapter, so it is assumed that every component will act in the z-direction.

Another important equation is the Newton's second law relating a force with mass and acceleration

$$\frac{\partial T}{\partial z} = \rho_m \frac{\partial^2 u}{\partial t^2}, \tag{2.6}$$

here ρ_m is the material mass density. For a non-piezoelectric medium if we insert (2.4) on (2.6), we end up with the wave equation:

$$\frac{\partial^2 u}{\partial t^2}, = \frac{c}{\rho_m}\frac{\partial^2 u}{\partial z^2}. \tag{2.7}$$

The phase velocity of the wave is defined as

$$v_p = \sqrt{\frac{c^E}{\rho_m}}, \tag{2.8}$$

it should be emphasized that the phase velocity has nothing to do with the particle velocity.

If the wave described in (2.7) propagates in the same direction than the applied electric field, the constitutive relations (2.4) are no longer valid since are implying constant electric field in the propagation direction. Applying a variable substitution on (2.4), we end up with

$$T = c^E \left(1 + \frac{e^2}{c^E \varepsilon^S}\right) S - \frac{e}{\varepsilon^S} D = c^D S - \frac{e}{\varepsilon^S} D, \tag{2.9}$$

where the superscript D indicates that the parameters are defined under a constant electric displacement. Using (2.9) to derive the wave equation (2.7), some changes can be seen on the phase velocity

$$v_p^D = \sqrt{\frac{c^D}{\rho_m}} = v_p \cdot \sqrt{1 + K^2}. \tag{2.10}$$

In (2.10), one of the piezoelectricity effects on the system can be seen: the acoustic velocity is higher than on the one of the simply mechanical case, deduced from the parameter c^E, that is because the piezoelectric effect stiffens the material being $c^D > c^E$. In (2.10) a new parameter was defined, it is the material electromechanical coupling factor K^2, given by

$$K^2 = \frac{e^2}{c^E \varepsilon^S}, \tag{2.11}$$

that depends of the material and it is a measure of conversion efficiency between electrical and acoustical domains in a piezoelectric.

2.2 Electric Impedance

In order to derive the electric impedance (Z_{in}) for the piezoelectric plate showed in Figure 2.1, we will make use of the following Ansatz for a time-harmonic acoustic wave propagating in the thickness z direction:

$$u(z) = [a \cdot \sin(kz) + b \cdot \cos(kz)] \cdot e^{j\omega t} \tag{2.12}$$

where ω is the angular frequency, $k = \omega / v_p^D$ is the wave number, and constants a and b are determined by the boundary conditions.

Inserting (2.12) in (2.9) the stress becomes

$$T(z) = c^D k \cdot [a \cdot \sin(kz) + b \cdot \cos(kz)] - \frac{e}{\varepsilon^S} D, \tag{2.13}$$

the term $e^{j\omega t}$ will be omitted from this point to keep the text more readable. All equations imply time harmonic fields albeit the contrary is indicated.

If the boundary condition of vanishing stress at the upper and lower surfaces of the plate is applied, $T(\pm d) = 0$ [3], we obtain

$$T(z) = \frac{eD}{\varepsilon^S} \left[\frac{\cos(kz)}{\cos(kd)} - 1 \right]. \tag{2.14}$$

The electrical response of the device is determined by its impedance Z_{in}

$$Z_{in} = \frac{V}{I} \tag{2.15}$$

being V the electric potential and I the current intensity. The former is defined between the two electrodes as

$$V = \int_{-d}^{d} E(z)\, dz \tag{2.16}$$

The same variable substitution performed on (2.9) is applied on (2.4) to obtain

$$E = -\frac{e}{c^D \varepsilon^S} T + \left(\frac{1}{\varepsilon^T} - \frac{e^2}{c^D \varepsilon^S} \right) D, \tag{2.17}$$

the electric potential at the electrodes is obtained integrating (2.17):

$$V = \frac{2dD}{\varepsilon^S} \left[1 - \frac{e^2}{c^D \varepsilon^S} \cdot \frac{\tan(kd)}{kd} \right] \tag{2.18}$$

On a dielectric material such as the piezolayer, a pure displacement current is generated between the electrodes, $J = \partial D / \partial t$. So, the current at the terminals is

$$I = j\omega A \cdot D \tag{2.19}$$

being A the electrode area of the device. By the use of (2.18) and (2.19), the input impedance of the resonator is obtained:

$$Z_{in}(\omega) = \frac{1}{j\omega C_0} \left[1 - K_t^2 \cdot \frac{\tan(kd)}{kd} \right]. \tag{2.20}$$

Here, another electromechanical coupling factor is introduced, defined as

$$K_t^2 = \frac{e^2}{c^D \varepsilon^S} = \frac{K^2}{K^2+1}, \tag{2.21}$$

this is the electromechanical coupling factor for thickness-longitudinal modes and for weak piezoelectrics, like AlN and ZnO, can be approximated $K_t^2 \approx K^2$. The term C_0 is the static capacitance, given by

$$C_0 = \frac{\varepsilon^S A}{2d}. \tag{2.22}$$

The device will resonate when the reactance or susceptance of the resonator equals zero, assuming Z_{in} is purely reactive, the series resonances will arise when $Z_{in} = 0$, and the parallel resonances (or antiresonances) when $Z_{in} \to \infty$ (or when the admittance $Y = 1/Z$ equals zero). So, from (2.20) the antiresonance frequencies can be obtained as

$$\omega_{a,n} = (2n+1) \cdot \frac{\pi}{2} \cdot \frac{v_p^D}{d}, \qquad n = 1, 2, 3... \tag{2.23}$$

The resonant frequency for the main resonating mode is therefore obtained from the following relation

$$\frac{\tan\left(\frac{\pi}{2} \cdot \frac{\omega_r}{\omega_{a,0}}\right)}{\frac{\pi}{2} \cdot \frac{\omega_r}{\omega_{a,0}}} = \frac{1}{K_t^2}. \tag{2.24}$$

If (2.23) is compared to the initially proposed in (2.1), it can be seen that in the one developed by the piezoelectric constitutive relations, asymmetric modes are not excited.

In Figure 2.2 one can see how at the resonance frequency the magnitude of the impedance tends to zero and the phase passes through zero, and how at the antiresonance frequency the phase passes through zero another time while the magnitude tends to infinity. Also, as described in (1.22) the separation between the resonance and antiresonance frequencies is determined by K_t^2.

2.3 Effective electromechanical coupling

On the previous section the material electromechanical coupling factor (K^2), and the electromechanical coupling factor for the thickness extensional mode (K_t^2) were introduced. This latter coefficient corresponds to the coupling on a piezolayer with infinitesimal electrodes. Since, we are discussing BAW resonators, it is more interesting to measure the conversion efficiency of the whole resonator structure. In [14],

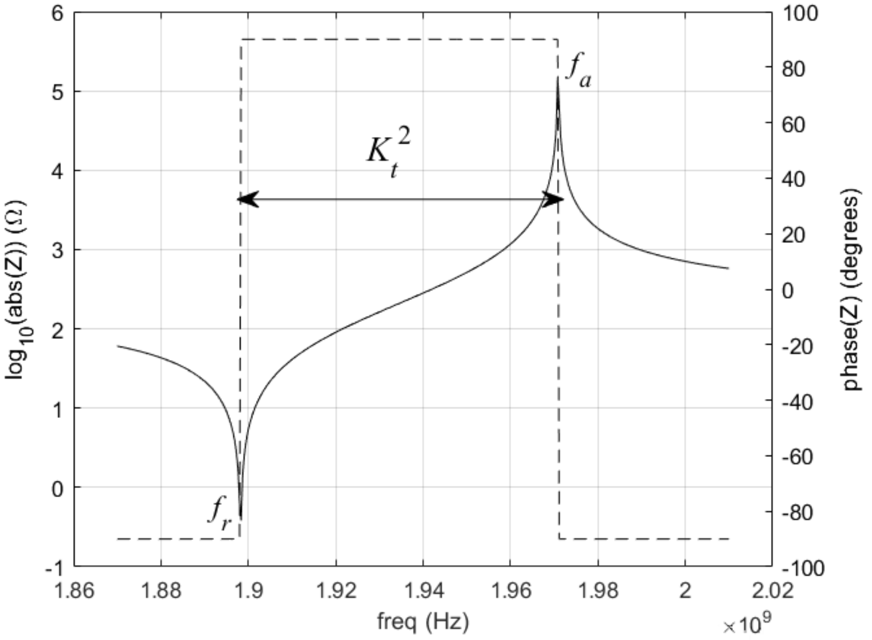

Figure 2.2: Magnitude (continuous line) and phase (dotted line) of the impedance of a resonator. The electromechanical coupling

a formula for calculating the effective coupling coefficient (k_{eff}^2) of the stack was provided:

$$k_{eff}^2 = \frac{U_m^2}{U_e U_d} \tag{2.25}$$

$$\begin{aligned} U_e &= \frac{1}{2}\int_{\Omega} T s^E T \, dV \\ U_m &= \frac{1}{4}\int_{\Omega} (TdE + EdT) \, dV \\ U_d &= \frac{1}{2}\int_{\Omega} E \varepsilon^T E \, dV. \end{aligned} \tag{2.26}$$

These energies are identified as elastic (U_m), electric (U_d), and mutual energy (U_m). In a resonator with real electrodes, we can expect the k_{eff}^2 to differ from the one obtained in an ideal BAW piezolayer, since the field patterns across the piezolayer and the electrodes will differ from (2.13) [3]. In this case the metal electrodes play also a role in the acoustic domain, since the acoustic wave is able to propagate into the metal layers Figure 2.3. For this simple case the expression of the effective coupling coefficient for the fundamental mode will end as [3]:

$$k_{eff}^2 = \frac{e^2}{\varepsilon^S c^D} \cdot \frac{8}{\pi^2} \frac{\cos^2\left(\frac{\pi}{2} \cdot \frac{t}{d+t}\right)}{\left(1 - \frac{t}{d+t}\right)}. \tag{2.27}$$

For this simple case, we can find the maximum coupling about at the electrode thickness ratio of $t/(d+t) \approx 0.26$. A more realistic case will be the one corresponding to electrodes with different acoustic impedance than the piezolayer (Figure 2.4). For the latter case, it is no possible to derive a closed form expression by means of (2.25), so numerical methods are needed.

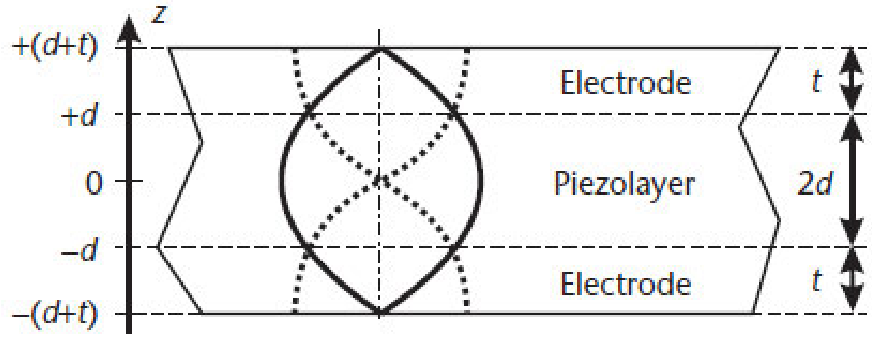

Figure 2.3: Geometry of a resonator with electrodes of thickness t of the same material of the piezolayer. The stress field is shown with a solid line and the displacement with a dashed line [3].

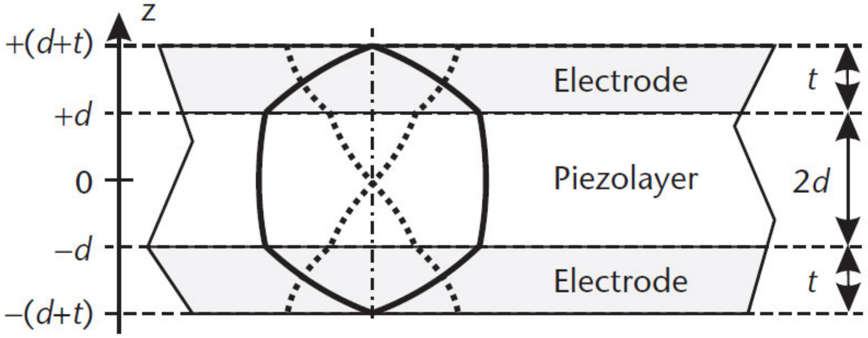

Figure 2.4: Geometry of a resonator with electrodes of thickness t with the acoustic impedance of the electrodes higher than the one of the piezolayer. The stress field is shown with a solid line and the displacement with a dashed line [3].

2.4 Losses on BAW resonators

On this section a brief overview of the sources of losses on BAW resonators will be given and a basic model of losses on BAW resonators will be derived.

2.4.1 Sources of losses

The basic loss mechanisms on BAW resonators can be grouped in three categories [3]:

- Electrical losses.
- Acoustic attenuation.
- Leaking waves.
- Thermoelastic damping.

Electrical losses are the ones concerning the electric resistivity of the metal electrodes, following Ohm's law the intrinsic resistivity of the electrode materials will play a role near the resonant frequency of the resonator (f_r), where the electric currents are largest. Other effect that plays a role on the resistive losses of the electrodes are the ones due to nonuniform stress distributions generated by the lateral acoustic propagation. These nonuniform stress distributions lead to eddy currents on the electrodes generating additional losses due to the Joule effect [15].

Acoustic attenuation takes place in the wave propagating in the piezolayer. This effect can be understood as a relaxation constant for the time derivative of the strain S [13]. We will assume that the entropy will remain constant since there are no thermal effects involved like for (2.4), so the constitutive equations will end as:

$$\begin{aligned} T_3 &= c_{33}^E S_3 + \eta_{33}\dot{S}_3 - e_{33}E_3 \\ D_3 &= e_{33}S_3 + \varepsilon_{33}^S E_3. \end{aligned} \tag{2.28}$$

Here, η_{33} is the viscosity. Neglecting the thermal effects with the introduction of losses seems quite naive at first glance. It is well-known that the introduction of irreversible thermodynamic processes, i. e. losses, lead to an increase of the system's entropy [16]. Nevertheless since we are dealing with small harmonic motions we will assume all thermal effects to be negligible. This is not the case for BAW resonators working at high power levels [17]. In [18], thermal effect on a BAW resonator are modeled with the use of the full constitutive relations.

The viscoelastic process is analogous to the Kelvin-Voigt viscous damping model (Figure 2.5) [12]:

$$T = ES + \eta\dot{S} \tag{2.29}$$

in this model, E stands for the Young modulus of the material. Since we are dealing with harmonic motions, viscosity can be inserted into a complex stiffness constant

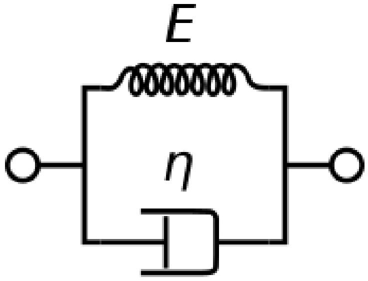

Figure 2.5: Kelvin-Voigt model for viscous damping.

making use of the time harmonic derivative:

$$T = (c + j\omega\eta) \cdot S. \tag{2.30}$$

For the acoustic wave propagating in the material, one can extract a complex propagation constant

$$k = j\alpha + \beta, \tag{2.31}$$

here β is the phase constant and α can be approximated as [3]:

$$\alpha = \frac{\eta\omega^2}{2v_p^3\rho_m}. \tag{2.32}$$

The third group of loss mechanisms are leaking waves. These waves are the ones regarding the leakage of acoustic energy outside the resonator structure. On SMRs some acoustic energy is leaked through the Bragg mirror contributing to the overall acoustic losses. Another source of leaking is across the lateral boundaries of the resonator.

The thermoelastic damping is a source of losses in longitudinal acoustic waves due to internal heat propagation on the crystal. This source of loss will be explained in more detail in Chapter 4.

2.4.2 Q factor of a resonator

In order to measure the energy dissipation of a resonator, the Q factor is introduced. The Q factor is the relation of the energy stored on the resonator and the energy dissipated per cycle. From this definition is noticeable the relation between the Q factor and the attenuation. The Q factor is defined as:

$$Q = 2\pi \frac{\text{energy stored}}{\text{energy dissipated per cycle}} = 2\pi f \frac{\text{energy stored}}{\text{power loss}}. \tag{2.33}$$

For any one-port resonator, the following expression can be derived [19], [20], [21]:

$$Q = 2\pi f \frac{\left|\dfrac{dS_{11}}{d\omega}\right|}{1 - \left|S_{11}\right|^2}, \tag{2.34}$$

here, the scattering parameter S_{11} correspond to the reflection coefficient of the resonator. This method can be easily used to extract the Q factor of the resonator's electrical measurements.

2.5 BAW models

In order to model the one-dimensional behavior of BAW resonators, the Butterworth-Van Dyke model (BvD) and the Mason model are the most commonly used.

2.5.1 Butterworth van Dyke (BvD) model

In [22], an equivalent circuit for the input impedance of a resonator is derived. From (2.20) it is clear that the resonator can be described by a capacitance C_0 in parallel with an acoustic arm, comprised by an inductance (L_1) and a capacitance (C_1) in series (Figure 2.6) [23]. The analytical expression of the impedance takes the form:

$$Z(\omega) = \frac{j(\omega L_1 - 1/\omega C_1)}{1 - \omega^2 C_0 L_1 + C_0/C_1}, \tag{2.35}$$

where we can define the series and parallel resonances as:

$$\omega_r = \frac{1}{\sqrt{L_1 C_1}} \tag{2.36}$$

$$\omega_a = \sqrt{\frac{C_1 + C_0}{L_1 C_1 C_0}} = \omega_r \cdot \sqrt{1 + \frac{C_1}{C_0}}. \tag{2.37}$$

This circuit does not include losses. In [24], the modified Butterworth-van Dyke (mBvD) is presented. This circuit adds three resistors to take into account for losses. The values of the resistors can be approximated to the Q factors at series and parallel resonances.

$$Q_s \approx \frac{\omega_r L_1}{R_s + R_1} \tag{2.38}$$

$$Q_p \approx \frac{\omega_a L_1}{R_0 + R_1} \tag{2.39}$$

Because of the simplicity of this model, it is commonly used for designing any type of acoustic filter [3].

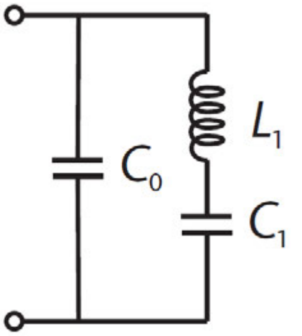

Figure 2.6: BvD model with a motional arm for the fundamental mode. [3]

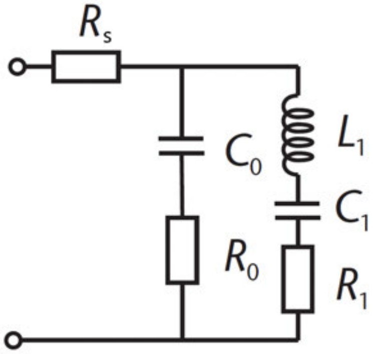

Figure 2.7: mBvD model with a motional arm for the fundamental mode. [3]

2.5.2 Mason model

The model previously derived works well when the effect of the electrodes is negligible (e. g. traditional crystal resonators). In thin film resonators, the metalized layers are no longer negligible since they add an additional mass to the system, also, SMRs are comprised of several layers. Being able to model these structures is crucial to accurately predict the BAW resonator behavior.

In order to model multi-layered structures on the thickness direction z, the Mason model is introduced [25], [22]. For a non-piezoelectric layer of thickness $2d$, manipulating (2.12), and introducing the particle velocity $v = j\omega u$, the acoustic characteristic impedance $Z = \rho_m v_p A$, and the force as $F = -TA$, the force at the upper and lower surfaces of the solid will become:

$$F_1 = \frac{Z}{j\sin(2kd)} \cdot [v(z_1) - v(z_2)] + jZ \cdot \tan(kd) \cdot v(z_1) \tag{2.40}$$

$$F_1 = \frac{Z}{j\sin(2kd)} \cdot [v(z_1) - v(z_2)] + jZ \cdot \tan(kd) \cdot v(z_2) \tag{2.41}$$

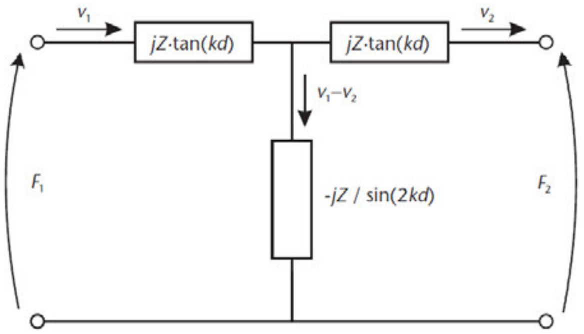

Figure 2.8: T-network modeling an acoustic transmission line [3].

From this, equivalences between the acoustic and electrical variables can be established: the particle velocity v at the boundaries with the current intensity I, and the forces F at the boundaries with the electric potential V. Looking at (2.40) and (2.41) an equivalent circuit can be identified composed by a T-network modeling an acoustic transmission line with two ports (Figure 2.8).

For a piezolayer, using the constitutive relation (2.13), (2.19), and setting $h = e/\varepsilon^S$ the mechanical forces at the surfaces become:

$$F_1 = \frac{Z}{j\sin(2kd)} \cdot [v(z_1) - v(z_2)] + jZ \cdot \tan(kd) \cdot v_(z_1) + \frac{h}{j\omega} \cdot I \tag{2.42}$$

$$F_1 = \frac{Z}{j\sin(2kd)} \cdot [v(z_1) - v(z_2)] + jZ \cdot \tan(kd) \cdot v(z_2) + \frac{h}{j\omega} \cdot I \tag{2.43}$$

The electric potential at the electrodes is obtained integrating (2.17):

$$V = \int_{z_1}^{z_2} E\,dz = \frac{dD}{\varepsilon^S} - h\left[u(z_2) - u(z_1)\right], \tag{2.44}$$

by the use of (2.19), (2.22), the current intensity between the electrodes become:

$$I = C_0 j\omega V - C_0 h\left[v(z_2) - v(z_1)\right]. \tag{2.45}$$

After some manipulation the Mason model is obtained (Figure 2.9). Using the Mason model, different layers can be interconnected, this way it is possible to model structures such as the SMRs and any transmission effect in the longitudinal dimension. As discussed on Section 2.4, attenuation can be introduced by means of a complex propagation constant $k = j\alpha + \beta$.

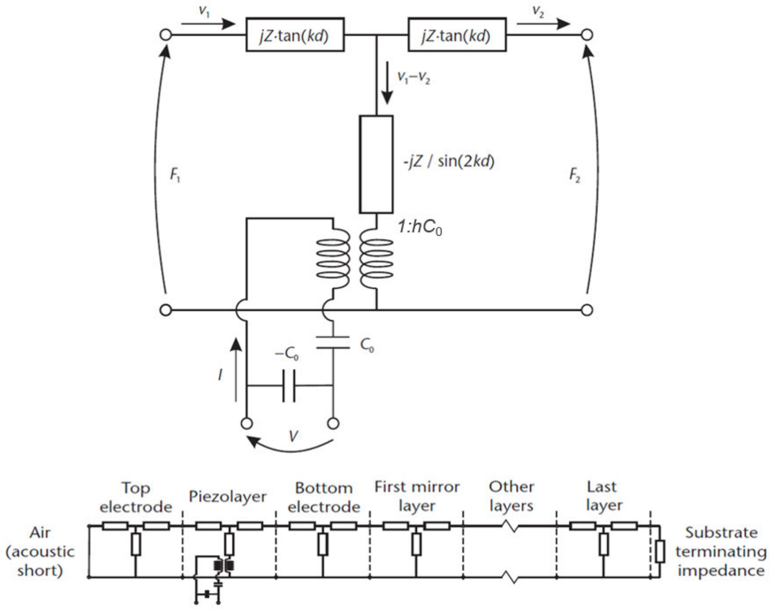

Figure 2.9: Mason model. Below it can be seen its implementation for a multi-layer resonator. On the left it represents a stress free boundary (acoustic short) and on the right a thin substrate layer modeled by a load [3].

2.6 Summary

Following the basic physical principles of piezoelectric solids, the electric input impedance of the resonator is presented in the first two sections. From this starting point the reader is presented to the effective electromechanical coupling of the resonator, and the role it has for the frequency spacing of the resonance and the antiresonance. Also, a brief explanation of how it becomes affected by the resonator's stack is given.

Loss mechanisms in BAW resonators are the other concern regarding their performance discussed on this chapter. Some of the main loss sources are discussed and a basic phenomenological model is derived. From this, the resonator's Q factor is presented, being the main performance indicator of the losses in a BAW resonator.

A basic circuital model for electroacoustic resonators, the BvD model is derived in the following section, being the common choice by filter designers due to its simplicity. Finally the Mason model is explained, giving a more physics based model, where the contribution of each resonator's layer can be taken into account.

Chapter 3

Modeling Lamb Waves on BAW Resonators

In a real resonator, and due to the nature of elastic vibrations in plates, a Lamb wave is excited [13]. This wave will propagate along the resonator's lateral dimension and is the responsible of the main resonance. For a laterally infinite BAW resonator, the physics described in Chapter 2 are perfectly valid. But due to this laterally propagating wave some spurious resonances arise in the electrical input impedance of the resonator.

In the following section, the physics of this Lamb wave will be presented to the reader, followed by a brief explanation of how these spurious resonance are excited. The basic suppression mechanisms of these resonances will also be explained through this section.

The next sections will deal with the physical modeling of the BAW resonator taking these resonances into account. In order to model the lateral effects of a BAW resonator, Finite Element Method (FEM) simulations are mostly used. Two-dimensional simulations are performed to obtain the stack's Lamb modes and their dispersion curves [26]. However, when aiming to simulate the behavior of an in-plane arbitrary shaped resonator, three-dimensional FEM simulations are mandatory [27]. Despite the reliability of FEM, their memory and computational power requirement are extremely heavy, especially for solidly mounted resonators (SMR) with many layers in their stack [28].

In Chapter 2, some models for the one-dimensional BAW resonator where exposed. The BvD model is capable of representing all that spurious resonances caused by Lamb modes with the use of additional motional branches. It is important although the development of models capable of simulating the lateral dimension of a resonator.

On the last decade, Mason based models [29], [30], and analytical solutions for the 2D simulations [31], [32], have been proposed. These models have the advantage of being much faster than FEM, but they are only able to model simple in-plane geometries.

Through this thesis several circuital models making use of dispersive transmission lines were developed. The first family of models are implemented by modifications of the Mason model. A dispersive acoustic transmission line is coupled to the Mason model adding the additional lateral dimensions. By these means, the suppression of the Border Ring as well as nonlinear effects can also be modeled.

The second family implements the Transmission Line Matrix (TLM) method to give more flexibility when modeling any in-plane electrode geometry. It enables the modeling of both 2D and 3D resonators, and suppression methods such as apodization and Border Ring as well.

3.1 Lamb waves on BAW resonators

The nature of plate waves was studied between the end of the XIX century and the beginning of the XX century, by Lord Rayleigh [33] and Lamb [34]. They ended up with the so called Lamb waves, that are the ones that arise on a BAW resonator. Sadly, the Rayleigh-Lamb equation does not have an analytical solution, being impossible to obtain an exact solution of the wave propagating modes. During the XX century, methods were developed in order to give approximate solutions to the Rayleigh-Lamb equation. A more modern approach to the work of Lamb can be seen on [35] and [13].

On an isotropic plate, Longitudinal acoustic waves (L) and Transverse Vertical acoustic waves (TV) are coupled at the interfaces. When an incident longitudinal wave arrives to a free surface, it generates reflected longitudinal and transverse vertical waves. The same applies for incident transverse vertical waves (Figure 3.1) [13].

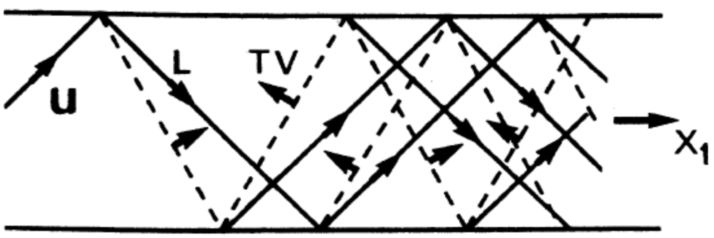

Figure 3.1: L and TV waves on a plate. When each of these incident waves arrives to a free surface, generates two reflected L and TV waves [13].

To analyze the wave propagation on an isotropic plate the Helmholtz decompo-

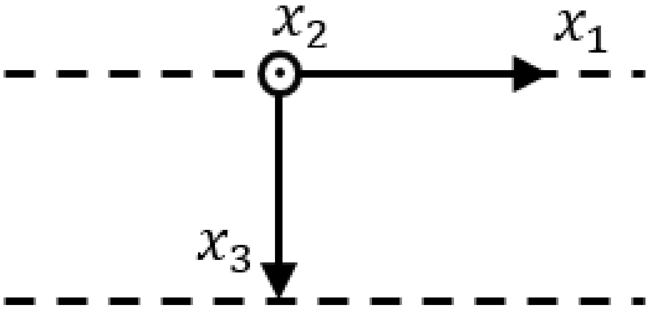

Figure 3.2: Isotropic plate.

sition is used for the displacement vector, giving an scalar potential ϕ, and a vector potential $\boldsymbol{\Psi}$

$$\boldsymbol{u} = \nabla\phi + \nabla \times \boldsymbol{\Psi}, \tag{3.1}$$

the former potentials will satisfy the wave equations.

$$\nabla^2\phi - \frac{1}{V_L^2}\ddot{\phi} \tag{3.2}$$

$$\nabla^2\boldsymbol{\Psi} - \frac{1}{V_L^2}\ddot{\boldsymbol{\Psi}}. \tag{3.3}$$

Here, $V_L^2 = c_{33}/\rho_m$ and $V_T^2 = c_{55}/\rho_m$, are the phase velocities for the longitudinal and transverse waves respectively. The strains that are related to volume changes are associated with the scalar potential ϕ; shear strains, that cause no volume changes are associated to the vector potential Ψ.

For a Lamb wave polarized in the x_1x_3 saggital plane and propagating in the x_1 direction (Figure 3.2), the displacement fields end as:

$$\boldsymbol{u} = \begin{bmatrix} -jk\phi - \frac{\partial\psi_2}{\partial x_3} \\ 0 \\ \frac{\partial\phi}{\partial x_3} - jk\psi_2 \end{bmatrix}. \tag{3.4}$$

There the diffraction in the x_2 direction was ignored, since it leads to a transverse horizontal mode (TH) that we are not interested in. Supposing harmonic motions, the functions ϕ and ψ_2 will satisfy the following equations:

$$\frac{\partial^2\phi}{\partial x_3^2} + p^2\phi = 0 \tag{3.5}$$

$$\frac{\partial^2\psi_2}{\partial x_3^2} + q^2\psi_2 = 0 \tag{3.6}$$

where, $p^2 = \frac{\omega^2}{V_L^2} - k^2$ and $q^2 = \frac{\omega^2}{V_T^2} - k^2$, respectively.

Since the boundary conditions of the plate impose that $T_3 = T_5 = 0$ at $x_3 = \pm d$, the stresses at the plate will become:

$$T_3 = c_{55}\left[(k^2 - q^2)\phi + 2jk\frac{\partial \psi_2}{\partial x_3}\right] \tag{3.7}$$

$$T_5 = c_{55}\left[(k^2 - q^2)\psi_2 - 2jk\frac{\partial \phi}{\partial x_3}\right]. \tag{3.8}$$

This set of equations requires the solutions to have different parity, so they become:

$$\phi = B \cdot \cos(px_3 + \alpha) \cdot e^{j(\omega t - kx_1)} \tag{3.9}$$

$$\psi_2 = A \cdot \sin(qx_3 + \alpha) \cdot e^{j(\omega t - kx_1)} \tag{3.10}$$

where $\alpha = 0$ (T_2 even, T_5 odd) or $\alpha = \pi/2$ (T_2 odd, T_5 even). Substituting this functions into the displacement (3.4) they end up as:

$$\boldsymbol{u} = \begin{bmatrix} -jkB \cdot \cos(px_3 + \alpha) + qA \cdot \cos(qx_3 + \alpha) \\ 0 \\ -pB \cdot \sin(px_3 + \alpha) + jkA \cdot \sin(qx_3 + \alpha) \end{bmatrix} \cdot e^{j(\omega t - kx_1)}. \tag{3.11}$$

We can clearly see that two types of Lamb wave exist: The symmetric modes ($\alpha = 0$), with the longitudinal component even, and the transverse odd; and the asymmetric modes ($\alpha = \pi/2$), with an odd longitudinal component and an even transverse one (Figure 3.3).

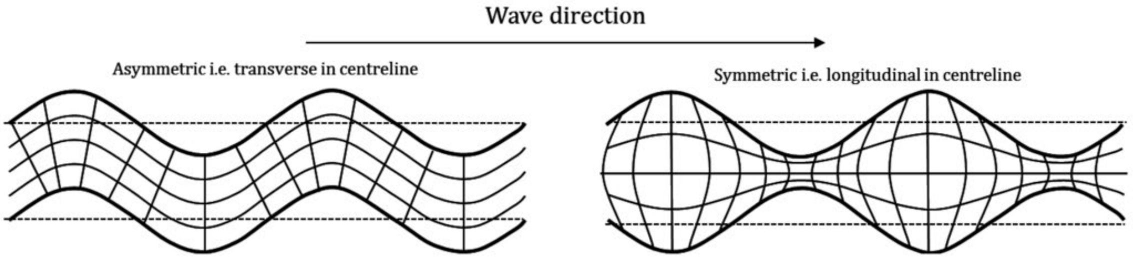

Figure 3.3: Symmetric and asymmetric modes of a Lamb wave [36].

Applying the boundary conditions to the stresses, we obtain the following linear system of equations:

$$\begin{bmatrix} (k^2 - q^2) \cdot \cos(pd + \alpha) & 2jkq \cdot \cos(qd + \alpha) \\ 2jkp \cdot \sin(pd + \alpha) & (k^2 - q^2) \cdot \cos(qd + \alpha) \end{bmatrix} \cdot \begin{bmatrix} B \\ A \end{bmatrix} = \begin{bmatrix} 0 \\ 0 \end{bmatrix}. \tag{3.12}$$

Non trivial solutions are found by setting the determinants of the coefficients to 0. This gives us the Rayleigh-Lamb equation:

$$\frac{\omega^4}{V_T^4} = 4k^2q^2\left[1 - \frac{p}{q}\frac{\tan(pd+\alpha)}{\tanh(qd+\alpha)}\right], \tag{3.13}$$

this dispersion relation between ω and k, results to the propagation characteristic of each Lamb mode. Equation (3.13) has no analytical solution so numerical methods are needed to obtain the plate dispersion curves. The dispersion curves for a plate are shown in Figure 3.4.

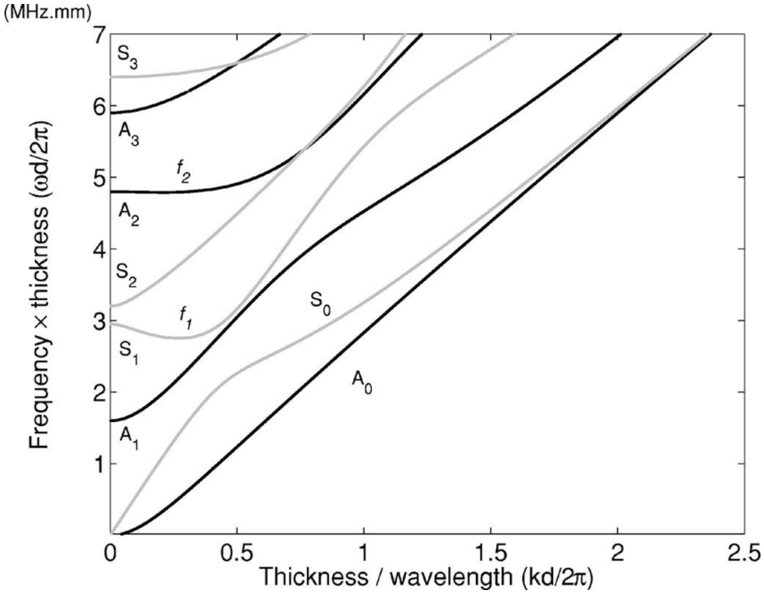

Figure 3.4: Dispersion curves on a plate. Symmetric modes are shown in grey, while asymmetric ones in black [37]

3.1.1 The main operating mode

On Chapter 2, the BAW resonator was treated in a one-dimensional approach, albeit being a plate. This approach, although it gives good approximation, is quite naive. In reality one can expect all the Lamb modes propagating along the resonator's lateral dimensions.

A common nomenclature for Lamb modes is one that involves its thickness standing wave patterns. It refers as Thickness Extensional (TE) mode to the one exhibiting displacements in the thickness direction, and Thickness Shear (TS) for the one exhibiting in the orthogonal direction (Figure 3.5). Usually a number accompanies its name defining the number of half-wavelengths.

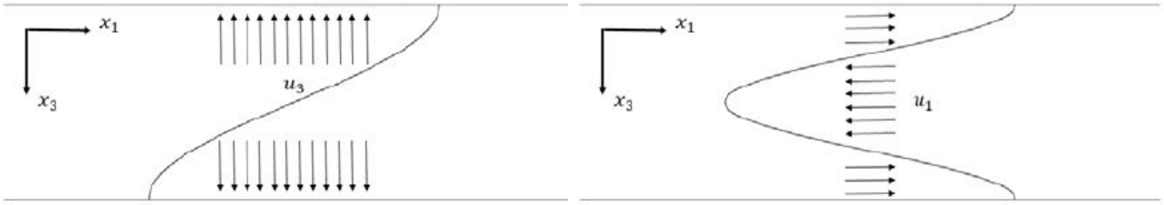

(a) Thickness extensional 1 (TE_1)

(b) Thickness shear 2 (TS_2)

Figure 3.5: Nomenclature of the Lamb modes depending in its thickness standing wave pattern. The arrows show the displacement (u_i) directions on the plate's thickness, indicated by its subscript. The number of half-wavelengths is represented by the continuous line.

One of special interest for BAW resonators is the TE_1 mode (Figure 3.5a). At its cutoff frequency, it has the same displacement distribution than piston mode of the BAW resonator. Also, looking at its cutoff frequency one notices that is the same that the resonant frequency of the piston mode.

The cutoff frequencies of these modes can easily be calculated in a 1D approach as done in Chapter 2 for the longitudinal one. The disposition of this cutoff frequencies will depend on material constants, particularly the Poisson ration (ν) of the stack [38].

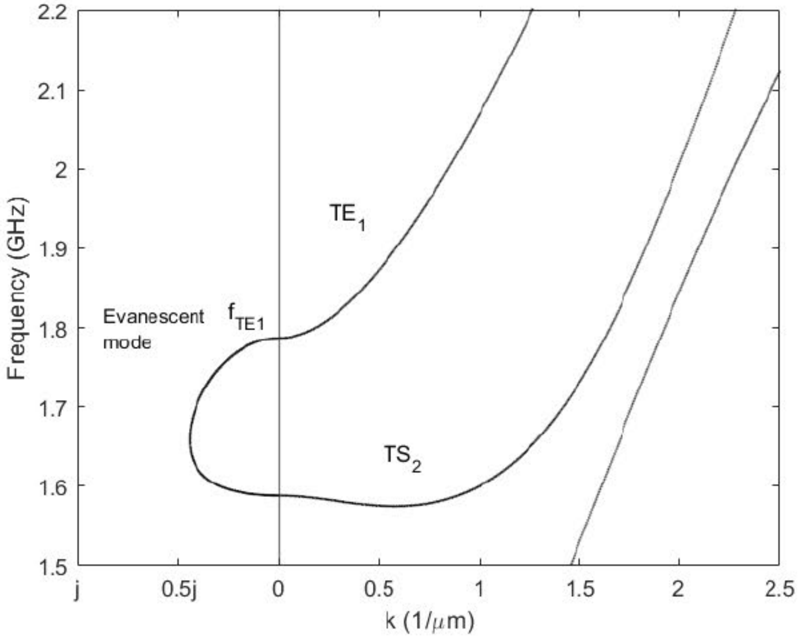

Figure 3.6: Dispersion curves of a ZNO piezoelectric plate exhibiting type I dispersion

Stacks exhibiting $\nu > 0.33$ have the cutoff frequency of the longitudinal mode higher than the shear, this is called type I dispersion. In the other hand, $\nu < 0.33$ have the shear cutoff frequency higher than the longitudinal one, this is called type II dispersion.

In Figure 3.6, the TE_1 and the TS_2 modes propagating in a type I BAW resonator are shown. Notice how between these two modes the propagation constant k becomes pure imaginary. This is an evanescent mode, whose field magnitudes will decay exponentially.

In [39] and [40], it is described a simple one-dimensional model of a BAW resonator based on its dispersion relation. They stated that: “If the portion of the wafer surrounding the resonator has a cutoff frequency higher than the exciting frequency, the resulting vibratory energy is essentially confined to the resonator with an energy distribution decreasing exponentially with distance away from the resonator. This exponential decay is not associated with energy loss but acts to trap the oscillating energy within a confined region.” In Figure 3.7a, such structure is drawn with the different dispersion regions. The active region with β_a real, and the inactive zone with β_o imaginary. These lateral wave numbers can be obtained from the dispersion curves of each zone (Figure 3.7b).

To simplify the analysis, we can assume that the displacement amplitude and the stress can be separated in spatial coordinates:

$$u_z(x,z) = u_z(z) \cdot u_z(x) \tag{3.14}$$

$$T_z(x,z) = T_z(z) \cdot u_z(x) \tag{3.15}$$

In this case, $u_z(x)$ acts as modulating term, arising for the non-uniformity of u_z

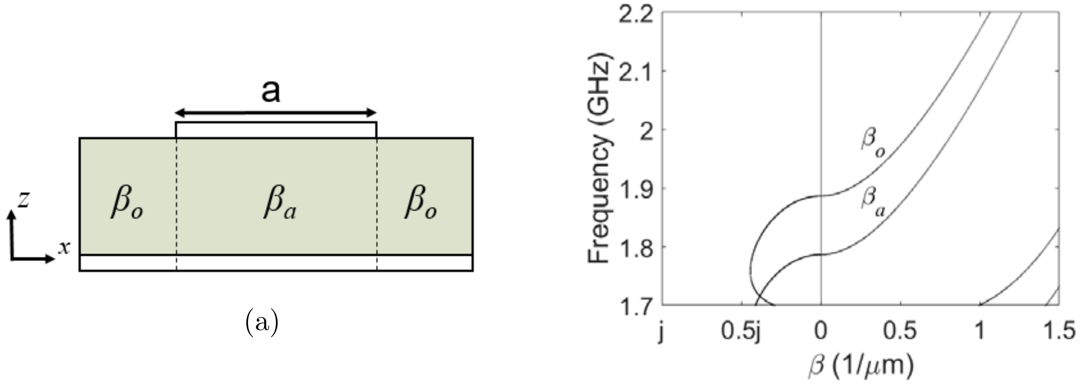

(a)

(b)

Figure 3.7: (a) 2D BAW resonator. (b) Dispersion curves of the active and inactive regions.

in the x-direction. The same decomposition can be applied to the effective coupling coefficient:

$$k_{eff}^2 = k_z^2 \cdot k_x^2 \tag{3.16}$$

where the contribution of the thickness direction is grouped under k_z^2. Applying the Berlincourt formula (2.25):

$$k_x^2 = \frac{\int E_z(x) u_z(x)\, dx^2}{\int E_z^2(x)\, dx \cdot \int u_z^2(x)\, dx} \tag{3.17}$$

here, $E_z(x)$ is the x-dependence of the z-directional electric field. Being the resonator a parallel plate capacitor the integral will become 1.

From (3.17), it can be seen that asymmetric lateral displacements would not electrically couple. So, the Ansatz for the displacement on the lateral dimension is the following:

$$u_z(x) = \begin{cases} A \cdot \cos(\beta_a x) & \text{Active} \\ B \cdot e^{-\beta_o x} & \text{Inactive} \end{cases}, \tag{3.18}$$

here A and B are coefficients for normalizing the amplitudes. Imposing the boundary conditions of continuity in displacement u_z and its first derivative du_z/dx, the following boundary condition is obtained:

$$\beta_a \tan(\beta_a a/2) = \beta_o, \tag{3.19}$$

from where it can be seen that the lateral dimension a also affects the resonant frequency of the BAW resonator.

If we suppose a hard wall at the boundaries of the active region i. e. $\beta_o = \infty$, we obtain the resonance condition of $\beta_a a = (2n+1)\pi$, for $n = 0, 1, 2, ...$ These are the spurious modes of the resonator that get coupled at the electrical response of the resonator (Figure 3.8). The spurious modes are undesired, since they usually degrade the response of the filter [3].

3.1.2 Suppression methods

Spurious modes have been a major drawback for designing BAW filters. Fortunately, on the last 20 years several works have been done to suppress the lateral spurious modes [41], [42], [43]. On this section the two main methods of suppression are discussed.

3.1.2.1 Apodization

Looking at a BAW resonator from the top view, one can observe the electrode (i. e. the active region where the acoustic energy is confined) as some sort of geometrical shape. Let us suppose the electrode as a shape such as a square, it can be imagined as

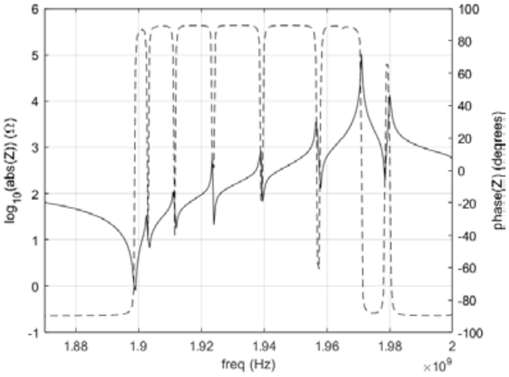

Figure 3.8: 2D BAW resonator exhibiting high spurious modes. The plot corresponds to a 2D FEM simulation of a ZnO membrane with a thickness of 1.74 μm, and a lateral dimension of 80 μm. Magnitude (continuous line) and phase (dotted line) of the impedance of a resonator.

a continuous array of (3.19), for each of the directions. Since the faces of the electrode are parallel for each direction, one can expect that each generated resonance is the sum of each of the array contributions.

Apodization relies in using polygonal shapes for the electrodes, which will not have parallel faces. Then, number of resonances will resemble more a continuum, generating much less coupled resonances. The main drawback of apodization is that we are really spreading the number of spurious resonances all over the frequencies. This fact, increases the loss all over the frequencies of the resonator, diminishing its Q factor [41].

3.1.2.2 Border Ring

The Border Ring (BR) is a suppression technique that applied on type I BAW resonators, and relies on an increased electrode frame at the boundaries of the active region (Figure 3.9a). This region will have a lower cutoff frequency than the active one (Figure 3.9b). The idea of the Border Ring is achieving a boundary condition of $du_z/dx = 0$, that way the lateral ways would not be reflected an the energy confinement would not be violated [42], [43]. The Ansatz for the displacement this time will become:

$$u_z(x) = \begin{cases} A \cdot \cos(\beta_a x) & \text{Active} \\ B \cdot \cos(\beta_{BR} x) & \text{Border Ring} \\ C \cdot e^{-\beta_o x} & \text{Inactive} \end{cases}, \tag{3.20}$$

here A, B, and C act also as coefficients for normalizing the amplitude. Forcing constant amplitude in the active region ($\beta_a = 0$) the new resonance condition is

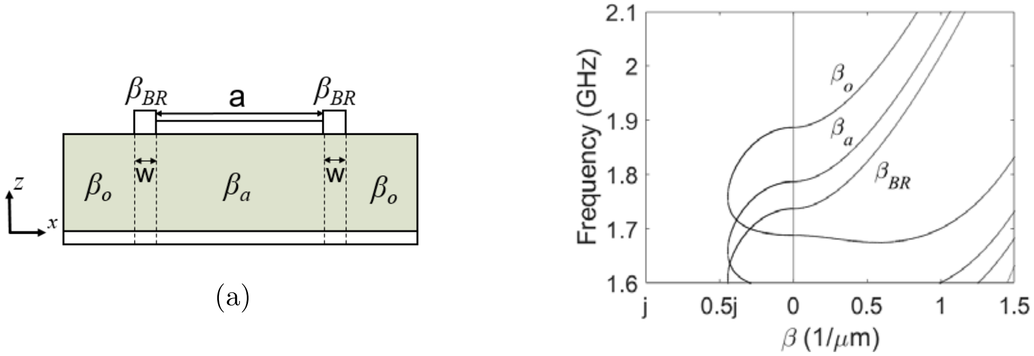

(a)

(b)

Figure 3.9: (a) 2D BAW resonator with Border Ring. (b) Dispersion curves of the active, the inactive, and the Border Ring regions.

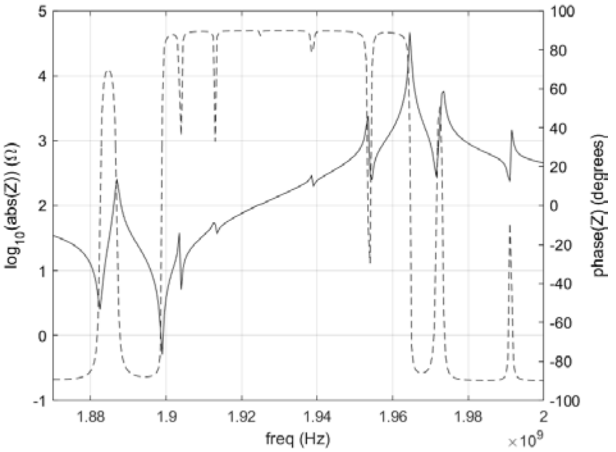

Figure 3.10: 2D BAW resonator with Border Ring. The plot corresponds to a 2D FEM simulation of a ZnO membrane with a thickness of 1.74 μm, a lateral dimension of 80 μm, and a BR width of 7.5 μm. Magnitude (continuous line) and phase (dotted line) of the impedance of a resonator.

achieved for the Border Ring:

$$\beta_{BR}\tan(\beta_{BR}w) = \beta_o. \tag{3.21}$$

If the Border Ring of the device is designed to match the resonant frequency of the device, the spurious modes of the resonator will be suppressed (Figure 3.10). Taking a closer look to Figure 3.10, one clearly sees a new mode that has appeared below f_s. this is the fundamental mode of the Border Ring that also gets coupled to the electrical domain.

3.2 BvD multi-branch

From the expression for the input impedance (2.20), the following expression can be derived [3]:

$$Z_{in}(\omega) = \frac{1}{j\omega C_0} \cdot \left[1 - K_t^2 - \sum_n \frac{\omega^2 k_n^2}{\omega_{a,n}^2 - \omega^2} \right], \tag{3.22}$$

here, k_n^2 is the coupling of the nth mode

$$k_n^2 = \frac{8K_t^2}{[(2n+1)\pi]^2}. \tag{3.23}$$

This expression can be transformed to the same BvD model than the one in Figure 2.6. The summatory on (3.22) can be modeled as parallel motional branches on the BvD circuit (Figure 3.11).

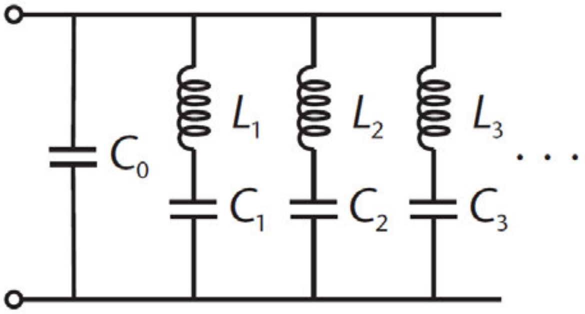

Figure 3.11: BvD equivalent circuit with a motional branch for each spurious resonance [3].

In order to use this model, the number of spurious resonances, their resonant frequency, and their coupling needs to be known in advance. For this reason, the use of the following models give an advantage, based on physical parameters of the resonator, they are able to accurately predict these spurious resonances. without any knowledge in advance of the number of resonances that can appear.

3.3 Mason based models

The first Mason based model for the lateral spurious resonances was presented in [29]. It introduces a transmission line to model the lateral propagation, where the values of this transmission line are fitted to a resonator. On [30], the idea behind this previous model is expanded, and the physical characteristics of the BAW resonator are taken into account.

The model presented in [30], uses an analogy between acoustic plate waves and electromagnetic waveguides. The electromagnetic waveguides are analyzed through the transverse resonance method, which allows to treat independently both in-plane directions. The propagating acoustic modes are defined in the transverse direction. This sets its cut-off frequency according to the lateral and thickness dimensions.

3.3.1 Lateral transmission line

For low wavenumbers ($k \sim 0$), and being the TE_1 the first odd symmetric mode ($A \sim 0$), the displacements defined on (3.11) end as:

$$u_x \approx 0; \quad u_z = -pB\sin(pz)e^{\pm jkx}. \tag{3.24}$$

The tangential stress T_{xz} will have the same distribution on the thickness direction than the displacement u_z:

$$T_{xz} = c_{55}(\pm jkpB)\sin(pz)e^{\pm jkx}, \tag{3.25}$$

where c_{55} is one of the constants of the material stiffness tensor.

Those field magnitudes u_z and T_{xz} are the ones that determines the propagating modes that laterally resonate generating the spurious resonances.

An electrical analogy of the acoustic wave is done to develop a transmission line model [30]. The equivalences between acoustic and electric transmission lines relate the mechanical force (F_z) with the electric voltage (V), and the particle velocity (v_z) with the electric current intensity (I). The phase constant (β), and the acoustic characteristic impedance (Z_0), need to be defined for the TE_1 mode.

In order to model the dispersive behavior of the TE_1 mode the phase constant (β) needs to satisfy the Rayleigh-Lamb relation (3.13), so $\beta = k$. An analytic expression can be approximated to the precomputed dispersion curve for Type I resonators [30]:

$$\beta = \frac{2\pi}{c_{lamb}}(f^r - f_{001}^r)^{1/r}, \tag{3.26}$$

where the exponent r is near to 2, the constant c_{lamb} is the estimated wave velocity of the mode, and f_{001} the cut-off frequency of the TE_1 mode, the so-called piston mode. The subscripts 001 indicate the number of half-wavelengths in the directions x, y, and z, respectively. Here, the 0 subscript indicates that the fields are uniform on the x and y directions, while the subscript 1 indicates half-wavelength on the thickness direction. The constants, c_{lamb}, r and f_{001}, are fitted to the measured or pre-calculated dispersion curve given a resonator's stack.

For a rectangular resonator, one can find the resonating frequency of each mode as:

$$f_{mn1}^r = \left(c_{lamb}\frac{m}{2a}\right)^r + \left(c_{lamb}\frac{n}{2b}\right)^r + f_{001}^r, \tag{3.27}$$

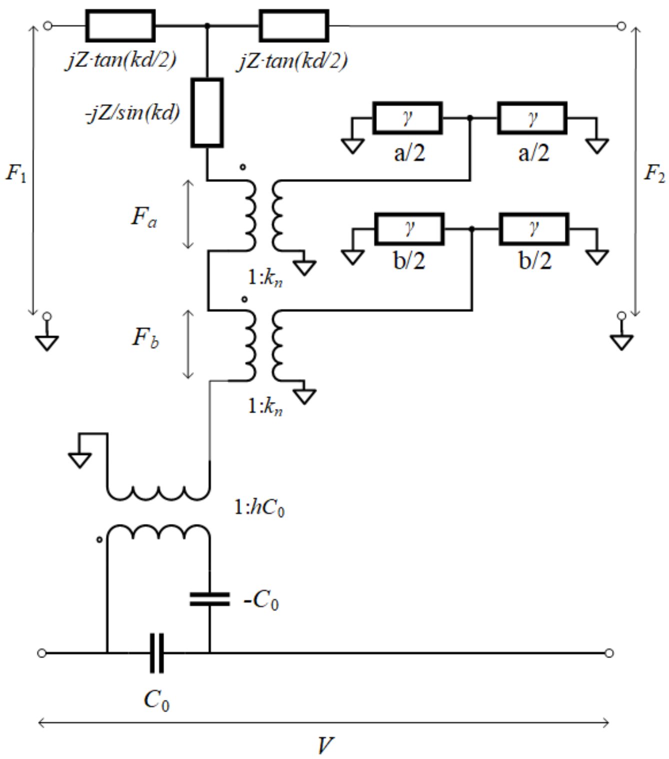

Figure 3.12: Circuit model of a lateral transmission line for each physical direction connected to a conventional Mason model.

where a and b correspond to the lateral dimension of the resonator. Here, the subscripts m and n ($m, n = 1, 2, 3\dots$) indicate the number of half-wavelengths of the mode in each lateral dimension.

For a wave propagating in an acoustic transmission line, the characteristic impedance will relate the force (F_z) and the particle velocity (v_z):

$$F_z = Z_0 \cdot v_z, \tag{3.28}$$

being:

$$F_z = \int_V \frac{\partial T_{xz}}{\partial x} dV = T_{xz} A_{tb}, \tag{3.29}$$

where A_{tb} is the resonator's cross-sectional area. Applying (3.24) and (3.25) to (3.28) and (3.29), the acoustic characteristic impedance for the TE$_1$ results in:

$$Z_0 = \frac{1}{\omega} \beta c_{55} A_{tb}. \tag{3.30}$$

Losses are introduced in the model by means of a complex propagation constant ($\gamma = \alpha + j\beta$), where α and β are the attenuation constant (Np/m), and the phase constant (rad/m) respectively. Assuming that $\alpha \ll \beta$, the Z_0 and the phase constant remains the same that in the lossless case.

The separation of variables is used to solve the coupling of the lateral mode, as described in [3] the coupling on each direction is considered independently. The piston mode is modeled by means of the traditional Mason model, and then one lateral transmission line for each direction is added. The coupling is done in a similar way as done in [29]. The strength of the coupling depends of on the v_z of the piston mode, equivalent to the coupling on the thickness direction.

The coupling of the transmission line to the Mason model can be seen in Figure 3.12. The lateral lines are coupled at the center of the resonator's lateral distance. This is the point where v_z is maximum. The turn ratio of the transformer is scaled for each of the modes propagating in the same direction, the scaling is given by (3.23).

The proposed model is able to simulate and predict the spurious modes for three-dimensional SMR-BAW resonators. Although, its main drawback its that is limited to simple electrode geometries, it is only able to model square and rectangular electrodes [30]. In Figure 3.13 the fitting of the model to a rectangular ZnO resonator is given.

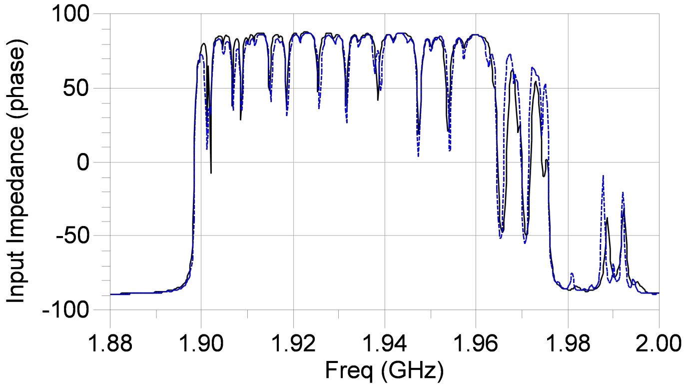

Figure 3.13: Input impedance of a ZnO rectangular resonator. Results of 3D FEM simulation are plotted in dotted blue line. The results of the circuit model are plotted in continuous black line [30].

3.3.2 BR modes on SMR

As explained thoroughly in Chapter 2, the main objective of the BR is to suppress the spurious resonances due to the lateral modes in a BAW resonator. Due to the increased thickness of the BR area, it resonates at a lower frequency than the resonator's active area. The electrical response of the resonator can be expected as having two shunted resonators of different thickness, adding another resonance below the main one. However, FEM simulations and measurements show something else. On Figure 3.14, multiple resonances for the BR mode appear [44].

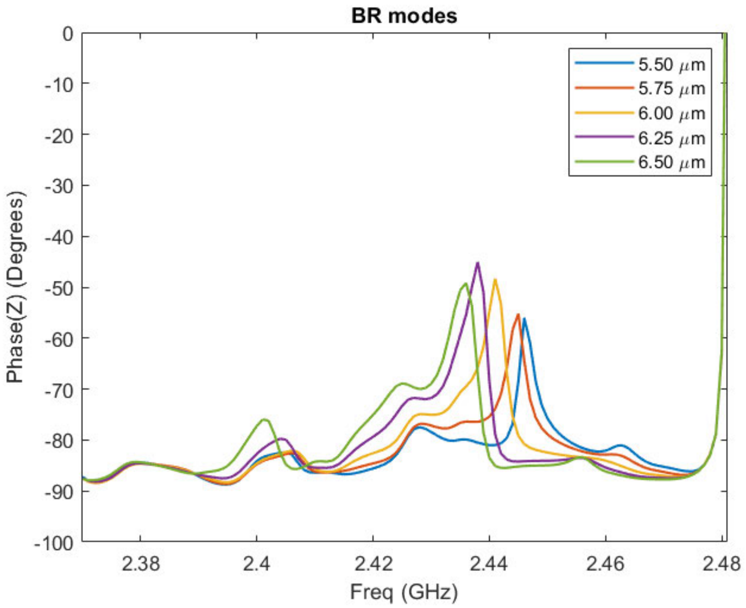

Figure 3.14: Different BR modes depending of the BR width (from 5.5 µm to 6.5 µm).

Depending of the width of the BR, more or less resonances appear in a quite unpredictable way. That phenomenon suggests that the multiple resonances are due to a lateral mode propagating, not only under the BR area, but also under the active area. This mode is manifested in the resonator's electrical response when the coupling in the thickness direction is high and that happens under the BR area, since the cut-off frequency of the TE_1 mode is lower for the BR section than the one for the active section. These low cut-off modes, which are responsible of the BR spurious modes, are below the TS_2 mode.

As an example, FEM simulations of an SMR-BAW resonator show that acoustic resonances below the cut-off frequency of the fundamental mode of the active area exist through the whole structure. This mode can be seen in Figure 3.15, where the displacement pattern at one of the BR resonant frequencies is shown.

3.3.2.1 Modeling the BR modes

In order of being able to model the BR modes, a modification of the Mason lateral model is proposed. The fundamental concept behind it remains in the naive initial idea that the response of the BR on a BAW resonator will resemble to two shunted resonators of different thicknesses. One can think of placing two Mason models in parallel, but there will be only a single and narrow resonance for the BR instead of the multiple resonances that appear on FEM simulations and measurements [44]. This is because the conventional Mason circuit only models for the propagation in

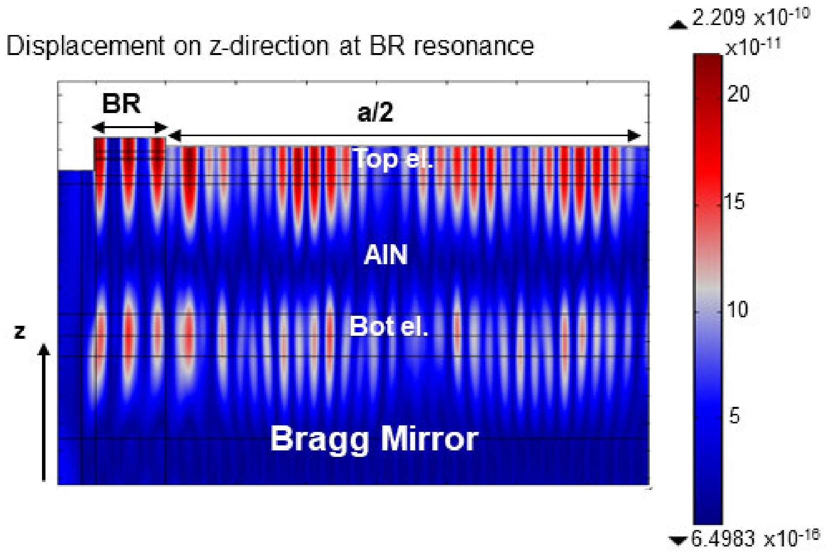

Figure 3.15: FEM simulation of a SMR. The displacement field on the thickness direction is shown.

the thickness direction.

The proposed model consists on using additional dispersive lateral transmission lines coupled to each conventional Mason circuit to consider the lateral propagation (Figure 3.16). When doing so, special care has to be taken when modeling the lateral propagation. Reference [43] proposes to use different transfer matrices for each resonator section to model the lateral displacement. Each transfer matrix has the phase constant of the dispersion curve of each section. This idea can also be applied to dispersive transmission lines being able to connect the different sections to obtain the displacement profiles. The advantage of using transmission lines over transfer matrices is that they can be used as it was done in [30] without more modifications. The last consideration to be done is that the Mason circuit that accounts for the BR section has to consider the dispersive behavior of the TE_1 mode. Note that the width of the BR section w_{BR} is typically a few microns, so its main TE_1 resonance if the BR was isolated would be slightly higher than its conventional cut-off frequency (piston-mode). This effect is usually neglected when modeling the active area using a conventional Mason model since the length of the resonator is around a hundred of microns, but it cannot be neglected for the very narrow BR section. Fortunately, this effect can be automatically corrected if the dispersive curve of the BR section is known.

The model of Figure 3.16 results as two Mason models, one for the resonator active area, which accounts also for the cancellation effects of the in-band lateral modes, and other for the BR area, which accounts for the modeling of the spurious

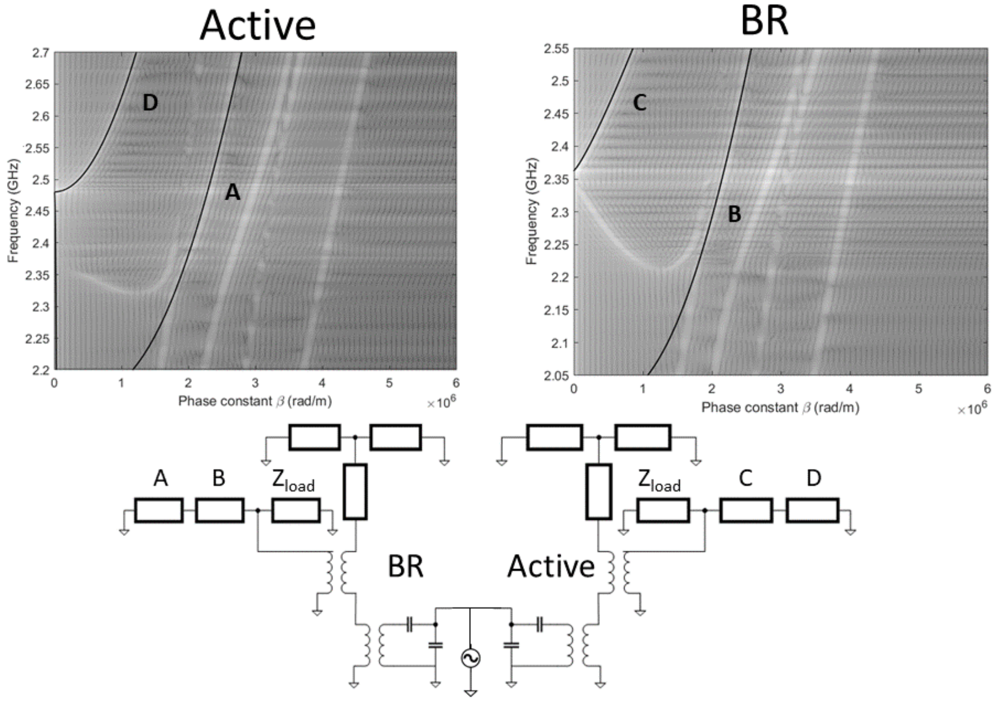

Figure 3.16: Circuital model for the BR modes. The dispersion curves correspondents to each lateral transmission line section are shown on top.

resonances below the series resonance. Both Mason models have dispersive lateral transmission lines modeling the different lateral sections of the resonator.

3.3.2.2 Mode dispersion relations

For the lateral transmission line belonging to the Mason of the active area, the dispersion curves of the TE1 mode are used both for the active area (curve D in Figure 3.16) and for the BR area (curve C in Figure 3.16). Regarding to the lateral transmission lines belonging to the BR Mason, the low cut-off modes dispersion curves (A and B in Figure 3.16) are selected instead. The outside area is modeled with a lumped resistance (Z_{load} in Figure 3.16) to model the small leakage of the acoustic waves.

The dispersion relations associated to each lateral line shown in Figure 3.16 are obtained from FEM simulations of the independent resonators having the stack configuration of the active area or the stack of the BR section. The lateral displacement profile is obtained for each frequency and later a Fast Fourier Transform (FFT) is performed to obtain them. Finally, these curves are fitted using the formulation

(3.26). This time the lateral transmission lines are not coupled at their maximum. For achieving only the coupling of the even modes, a short circuit is imposed on the center of the resonator lateral dimension. Now, the lateral transmission line is coupled at the interface of the Border Ring and the non-active zone. This coupling at a single point can lead to some errors in the model.

3.3.2.3 FEM simulations of SMRs with BR

SMRs with different BR widths were simulated to validate the proposed model. From the same stack, we obtained the dispersion curves shown in Figure 3.16. The circuital model was set like in Figure 3.16 and adjusted to match two different BR widths of two FEM simulated resonators. Figure 3.17 shows the phase of the input impedance of two simulated SMR with different BR widths, and the adjustment of the circuital model proposed.

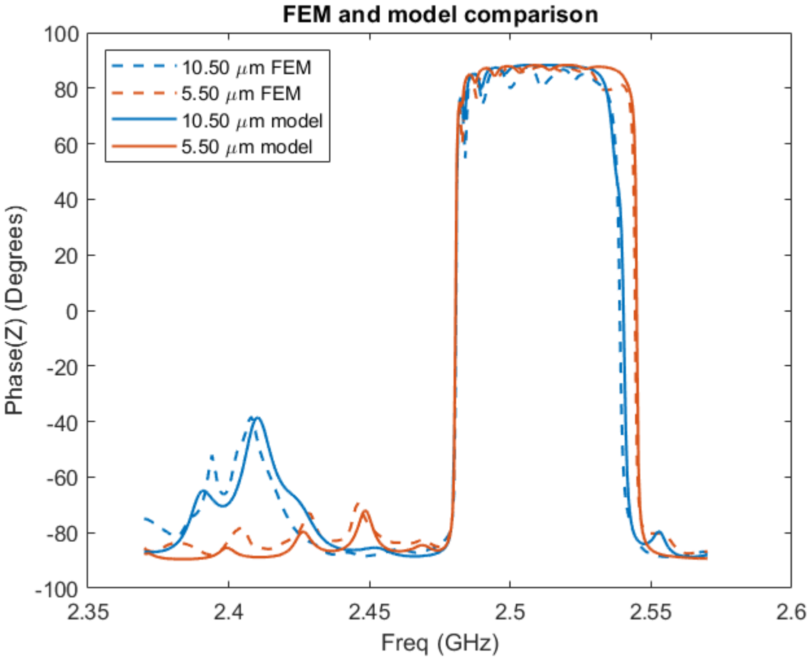

Figure 3.17: Phase of the input impedance of FEM simulated SMR (dotted traces), and adjustment of our model (solid traces). Blue traces correspond to a BR width of 5.5 µm, while red to 10.5 µm.

As it can be seen, the current model is not able to perfectly predict the in-band cancellation effect. We believe that is due to the very simplified model that couples the lateral transmission lines in a single point, losing therefore the distributed nature of the coupling. This inaccuracy can be corrected in part if the w_{BR} considered for the in-band cancellation differs a little from the real one. For this example, we have considered w_{BR} of 10.9 µm and 5.21 µm for the in-band cancellation, being the real values w_{BR} 10.5 µm and 5.5 µm respectively.

Despite the simplified coupling mechanism of the lateral transmission lines, the current model can be useful to model, for a given optimum border ring, the BR modes and the in-band lateral modes for different dimensions of the active area and, therefore, different aspect ratios as it is shown in the next subsection.

3.3.2.4 Measurements of SMR resonators with BR

The measured devices were four SMR resonating at 2.48 GHz, with a BR width of 3.5 µm, two different areas ($13 \cdot 10^{-9}$ m^2 and $6.46 \cdot 10^{-9}$ m^2), and for each area two different aspect ratios (one square resonator and one rectangular with an aspect ratio of two).

The dispersion curves for the active area were obtained in an experimental way adjusting the dispersion curves to a measured SMR without BR. The model was then adjusted to a certain BR width, which can be different for the BR and active section, to match one resonator. The width selected to match the in-band cancellation was 3.5 µm, while the one for the BR resonances was 5.9 µm.

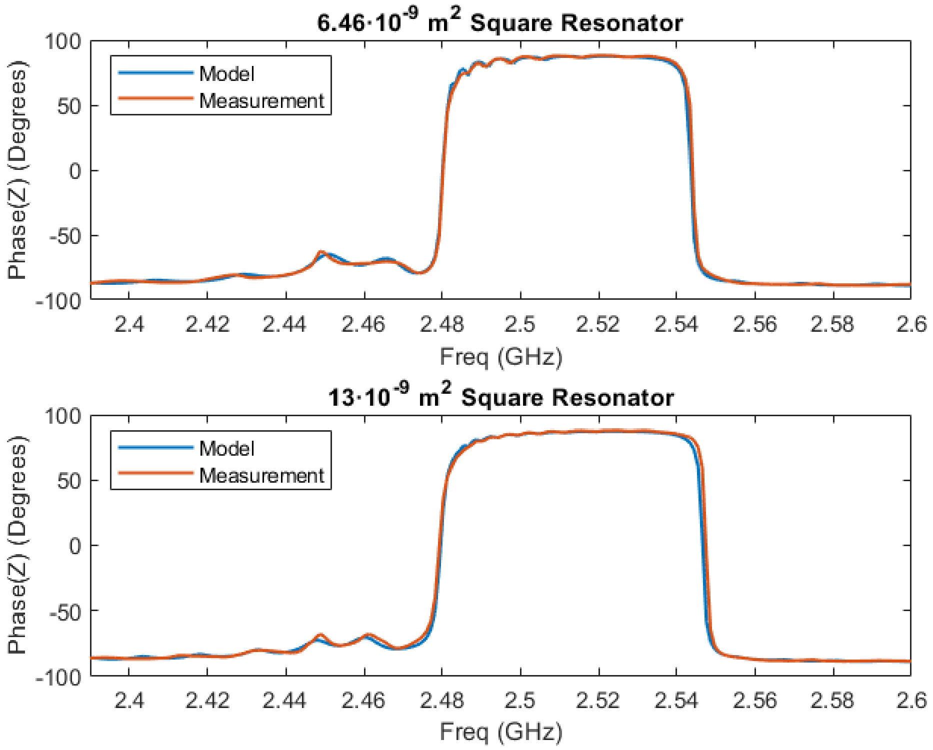

Figure 3.18: Phase of the input impedance of the two measured square resonators.

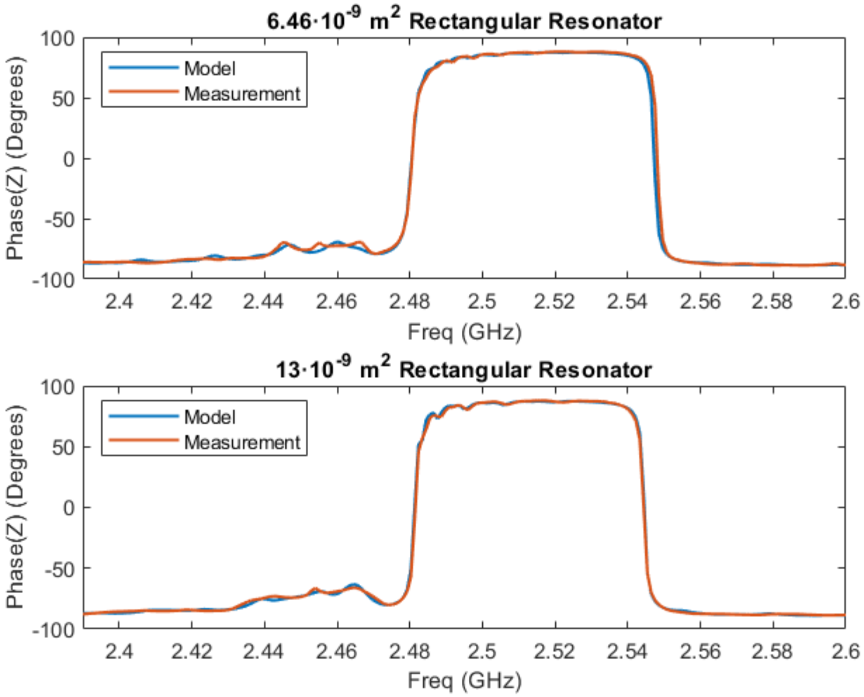

Figure 3.19: Phase of the input impedance of the two measured rectangular resonators.

Using the same parameters but the area and aspect ratio, the other three resonators were simulated showing a fairly good agreement between the circuital model and the measurement (Figure 3.18 and Figure 3.19). It can be seen that once the BR width that provides good agreement with the measurements is found, any change on the area or the aspect ratio of the resonator matches the spurious modes suppression and the BR resonances.

The main drawback of this circuital model is that it fails when simulating the cancellation and the BR mode as a function of the BR width. This is due to the coupling of the lateral line at a single point. For resonators without BR there are always a maximum of the stress at the coupling point, but for resonators with BR that maximum does not rest at the coupling point in the circuit model.

Despite its limitation, this model gives strong evidence of the BR resonances origin, laying it in the low cut-off modes propagating through the whole resonator, which are electrically coupled mainly at the BR region. It is also remarkable that the model allows to predict for a given BR width, the cancellation effect and BR resonances as a function of the resonator shape. That is a valuable asset for optimizing the shape dimensions trying to minimize the BR resonances, while keeping good cancellation of the in-band modes.

3.4 2nd Harmonic Emissions on BAW Resonators Exhibiting Lateral Spurious Resonances

Nonlinear behavior of Bulk Acoustic Wave (BAW) resonators, is currently one of the most relevant aspects to improve in mobile phone's RF acoustic duplexers. This is crucial to avoid desensitization on the receiver. On the last years, several Mason based models were proposed to model the nonlinear behavior of BAW resonators [45], [18], also none of these models considered the lateral dispersive behavior of the resonator. Reference [46] included the effects of the lateral modes on the second harmonic (H2) response using a Butterworth-van Dyke (BvD) based model. The inconvenient of this approach is that it needs many BvD additional branches, as many as lateral resonances, which must be included into the equivalent circuit.

The equivalent circuit proposed here models all the lateral resonances including just two dispersive transmission lines, one for each in-plane dimension, and just one nonlinear parameter can explain the H2 measurements.

Departing from the Mason lateral model shown in Chapter 3, the stress perturbation generated by the lateral resonances is added to the nonlinear constitutive relations. The model is solved using the Harmonic Balance (HB) method. The results of the simulated H2 response are compared to one-tone measurements showing good agreement between simulations and measurements.

3.4.1 Nonlinear constitutive relations

At high power levels, the intrinsic nonlinear behavior of BAW resonators generates second harmonic (H2) responses [17]. These intrinsic nonlinear behavior is due to nonlinear constitutive relations.

3.4.1.1 Piezoelectric layers

The nonlinear constitutive relations of the piezoelectric layer have been obtained traditionally from a McLaurin expansion of the Gibbs free-energy function ($G = U - ED - \sigma\Theta$). For the second harmonic response the nonlinear constitutive relations become

$$\begin{aligned} T &= c^E S - eE + \Delta T \\ D &= eS + \varepsilon^S E + \Delta D, \end{aligned} \tag{3.31}$$

here, the tensor indices are dropped (assuming we are dealing with fields only in the thickness direction z), and as done in Section 2.1, entropy is assumed to remain constant ($d\sigma = 0$). ΔT and ΔD are the nonlinear contributions to the constitutive relations of the material.

Taking only into account the most relevant nonlinear terms for the H2 generation

[47], and adding a lateral perturbation on the φ_5 term, the constitutive relations end up as

$$\begin{aligned}\Delta T &= \varphi_5 SE + \varphi_{5lat} \cdot S_{lat} E \\ \Delta D &= \varepsilon_2^S \frac{E^2}{2} - \varphi_5 \frac{S^2}{2} - \varphi_{5lat} \frac{S_{lat}^2}{2},\end{aligned} \tag{3.32}$$

in which ε_2^S, φ_5 are the second order nonlinear constants, and φ_{5lat} the nonlinear constant for the lateral modes. This is a phenomenological approach which aims to consider the lateral displacement. The second order terms are the main responsible of the second order response, although there is evidence that even third order terms have impact on the H2 response. The lateral perturbation for the strain is obtained from

$$S_{lat} = \frac{F_a}{A_{tb} \cdot c_{55}^E} + \frac{F_b}{A_{ta} \cdot c_{55}^E}, \tag{3.33}$$

S_{lat} is a lateral perturbation of the solution. F_a and F_b are the mechanical forces of the lateral perturbation at each orthogonal direction. A_{ta} and A_{tb} are the cross-sectional areas for each side of the resonator.

3.4.1.2 Non-piezoelectric layers

The constitutive relations for the non-piezoelectric layers are truncated up to the second order and end up as

$$\begin{aligned}T &= cS + T_C \\ T_C &= \frac{1}{2} c_2 S^2,\end{aligned} \tag{3.34}$$

where c, and c_2, are the derivatives of the stiffness constant. Notice how the value of these constants will differ from one material to another.

3.4.2 Nonlinear Mason model

The electrical model used for the piezolayer is based on the lateral line lossless non-distributed Mason model presented in [30]. Nonlinearities due to the Lamb modes will only be considered in the piezolayer. The nonlinear contributions are added to the modified Mason model in the same way that in [48] and [18]. The nonlinear sources are then defined as

$$\begin{aligned}T_C &= \Delta T + h \cdot \Delta D \\ V_C &= \beta^s \cdot \Delta D \cdot 2d,\end{aligned} \tag{3.35}$$

being $2d$ the thickness of the piezolayer.

Nonpiezoelectric layers are modeled in two different ways. Layers that have no nonlinear contributions to the H2 response, are modeled with a linear T-network model of an acoustic transmission line. Layers such as SiO_2 are modeled using a discretized nonlinear model composed of the equivalent lumped circuit for acoustic transmission lines [47]. The reason for that choice is that in those layers, the standing wave pattern of the stress plays a significant role on the H2 generation.

From the nonlinear Mason model with its nonlinear sources (3.35), and adding the lateral transmission lines, an equivalent Mason model for the piezoelectric layers is obtained (Figure 3.20). The nonpiezoelectric layers are added to model the electrodes and the acoustic reflector. These layers are added connecting the acoustic transmission lines to the Mason's acoustic terminals F_1 and F_2 as explained on Chapter 2.

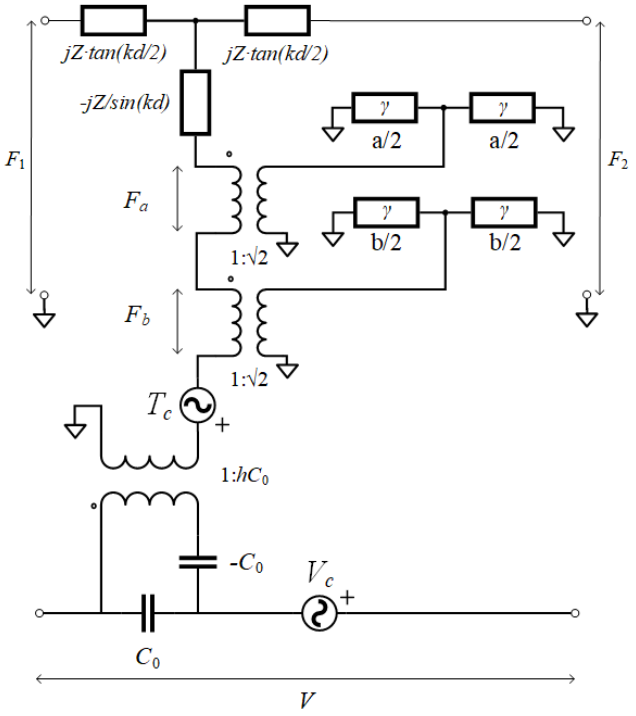

Figure 3.20: Equivalent nonlinear lateral Mason model for the piezoelectric layer [55]

3.4.3 Devices and linear measurements

Two different resonators, named R1 and R2, were measured and adjusted using the model described on the previous section to prove the suitability of our approach to characterize and predict the H2 response of SMR-BAW devices.

The stack distribution of the two resonators can be seen on Figure 3.21. Although the stack materials are the same in both resonators, they differ on their layer's thicknesses. Due to that, they exhibit different dispersive behaviors and different lateral modes. The fundamental resonance in both resonators, with an AlN thickness of ~900 nm, is around 2.31 GHz. The main difference between these two resonators appear on their H2 response. The different layer thicknesses of the acoustic reflector

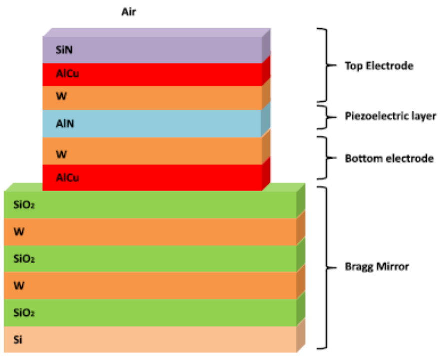

Figure 3.21: Stack configuration of the measured SMR-BAW devices [49]

generate spurious resonances over the fundamental one that interfere with its H2. Both resonators have rectangular shape and the same area, but exact dimensions cannot be disclosed here for confidential reasons.

The first step when modeling nonlinearities of a BAW resonator is adjusting its linear response. The measured input impedance is compared with the one adjusted from the model Figure 3.22.

The dispersive curve of the lateral transmission could be extracted from interferometric measurements of the resonator. However, it is much faster to find the parameters c_{lamb} and r by adjusting the phase of its input impedance.

3.5 Nonlinear measurements

Nonlinear measurements of the H2 response were obtained using the measurement setup described in [49]. Here, a one tone frequency sweep is performed. The power emissions at the second harmonic of this tone are measured in order to obtain the H2 response of the resonator. The simulations were performed using Harmonic Balance simulator on Advanced Design System.

Figure 3.23 shows the H2 response for R1 and R2. Note that the peak appearing at the right of the maximum is placed at different frequencies. This is due to the thickness of the SiO_2 layers on the acoustic reflector. The main responsible of the H2 response is the φ_5 parameter of (3.32), the value obtained for this model is $-20.5 \cdot e_{AlN}$. That value is about 10% higher than the published on [47] and [49] mainly because of the effect of the lateral lines nonlinear response lowering the power level. φ_{5lat} was set to the same value than φ_5. The lower φ_{5lat}, the higher the averaged H2 power but the lateral modes would not couple enough to the H2 response.

On the other side, ε_2^S is found to be $20 \cdot \varepsilon^S e / c_{AlN}^E$, the same value was found on [47]

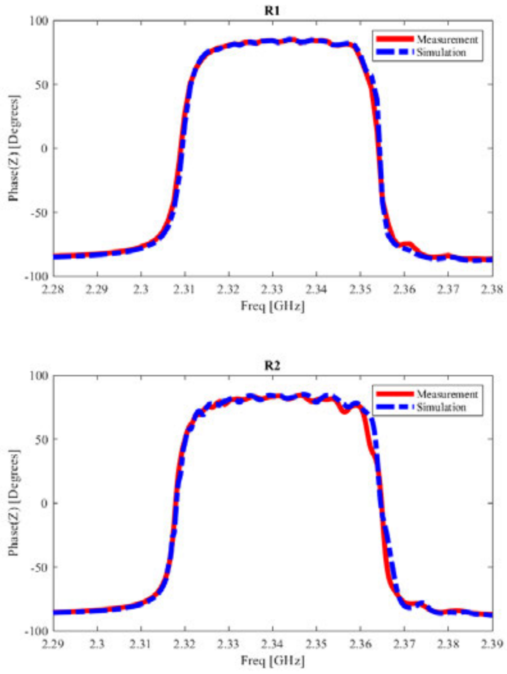

Figure 3.22: Phase of the input impedance of R1 and R2. Measurements correspond to the red line, while simulation to the dashed blue line.

and [49]. The term c_{2SiO_2}, that has strong relevance on the SiO_2 peak, is near a 10% lower than on previous references, having a value of $-5.8 \cdot c_{SiO_2}$. These values work well for the two measured resonators, although having different dispersion curves and different lateral resonances.

The proposed circuital model succeeds in predicting the lateral modes appearance on the H2 response. Using the same nonlinear parameters gives consistent results for different resonators. Its main strength is to rely in material nonlinear properties, making it independent from the stack configuration. Nevertheless, the dispersive behavior of the propagating Lamb wave must be known.

The 10% increase of the φ_5 AlN can be due to the increase of acoustic losses on the piezolayer due to the coupling of the lateral transmission lines. That would cause the need to increase the φ_5 AlN value to match the H2 measurements. Also, since practically all loss mechanisms on this model are considered in the piezolayer, nonlinear constants of other layers need to be slightly lower to fit the measurements, as in the case of the c_2 parameter of the SiO_2.

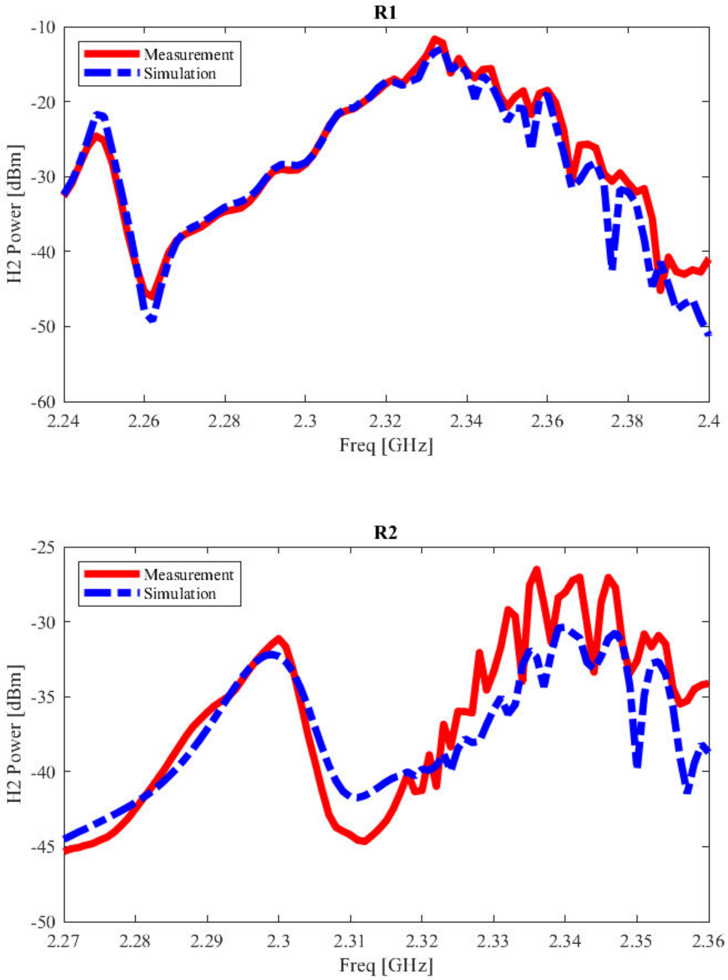

Figure 3.23: H2 measurement and simulation of R1 and R2. Measurements correspond to the red line, while simulation to the dashed blue line.

3.6 The Transmission Line Matrix (TLM) method

On the previous section the main issue of the Mason model with lateral lines its described: the coupling at a single point of the lateral standing wave pattern does not give accurate results when introducing the BR. Also, its important to notice its limitation to rectangular shaped electrodes.

In [50], a new approach based on the Transmission Line Matrix (TLM) method was presented. It allows for fast simulation of BAW devices with an arbitrary electrode shape.

3.6.1 Quasi-2D model

The first approach is to reduce a simple two-dimensional BAW resonator to a one-dimensional problem. It is achieved via the Quasi-2D model, where only the lateral wave propagation is taken into account. Being the main responsible of in-band spurious modes, only the TE_1 mode is taken into account [32].

For a two-dimensional resonator comprised in the xz-plane, as outlined in Figure 3.24, the Lamb wave propagates in the x-direction. The lateral dimension a is discretized in N_x elements of length dx.

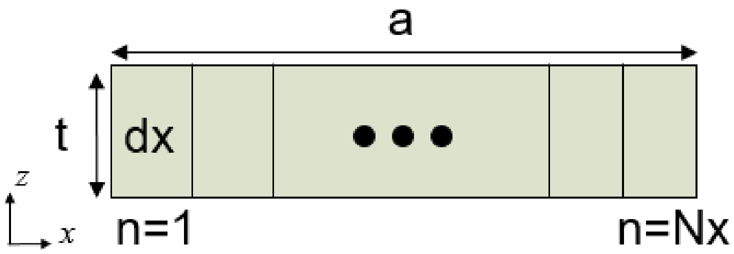

Figure 3.24: Two-dimensional resonator in the xz-plane. The x-dimension is discretized in N_x elements.

3.6.1.1 Unit cell

Each of the unit cells is modeled with a dispersive transmission line as the ones used in the Mason lateral model. Since we are using nodal Y-matrices, in order to implement the free stress lateral boundary conditions (see section 3.6.1.2, below) [50], it is more convenient to invert the typical equivalences between electric and acoustic magnitudes. That means defining V as velocities and I as forces. Then the Z_0 of the transmission line is defined as the inverse of (3.30):

$$Z_0' = a_{kz} \frac{\omega}{\beta c_{55} A_{tb}}, \tag{3.36}$$

here a_{kz} acts as a scaling factor to adjust the resonator coupling. This is required because the displacement field (3.24) is a simplification obtained from the Lamb-wave equations for non-piezoelectric isotropic plates [13].

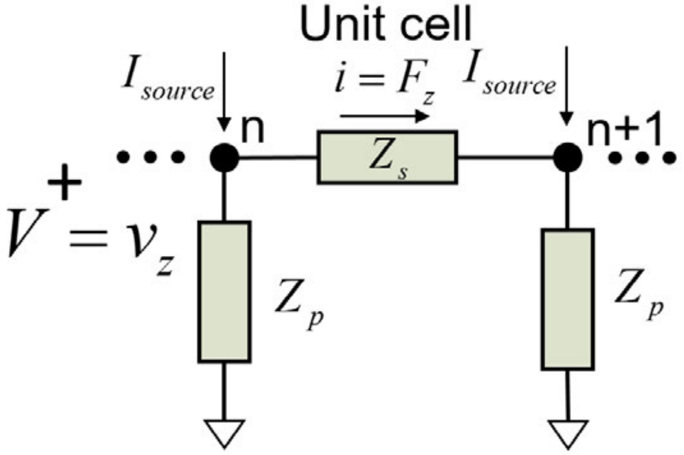

Figure 3.25: Equivalent Π-network of a dispersive transmission line in the x-direction

Then, the equivalent circuit of a unit cell of the TL is depicted in Figure 3.25, where the values of the Π-network are now:

$$Z_s = Z_0' \cdot \sinh(\gamma \cdot dx) \tag{3.37}$$

$$Z_p = Z_0' \frac{1}{\tanh(\gamma \cdot dx/2)} \tag{3.38}$$

$$dx = a/N_x. \tag{3.39}$$

The propagation along the lateral dimension of the resonator is modeled cascading several unit cells.

3.6.1.2 Lateral boundary conditions

In an ideal resonator, the acoustic wave is reflected at its lateral edges, thus generating each of the lateral spurious resonances.

- **Free stress:** The velocity v_z at the boundaries will be zero, implying the full reflection of the acoustic waves at the lateral interfaces. To impose this boundary condition, the lateral transmission lines are ended with a short-circuit. This way, the voltage at the end of the lines become zero.

- **Lateral leakage:** Acoustic energy may leak out of the resonator active area. This effect is called lateral leakage and degenerates the Q factor around the antiresonance frequency [3]. If required, this effect can be modeled adding a conductance to the ends of the transmission line instead of an ideal short-circuit.

3.6.1.3 Model implementation

Applying an electric potential (U) on the resonator electrodes, a constant F_z is generated along the resonator lateral dimension [35], [51]. Due to the impedance inversion, it is modeled as distributed current sources (I_{source}) at each cell node:

$$I_{source} = e \cdot dx \cdot b/t \cdot U, \tag{3.40}$$

where e is the piezoelectric constant for the piston mode, b the lateral dimension on the y axis, and t the thickness of the piezolayer between the electrodes.

The distributed transmission line will be assembled in a nodal Y-matrix made of (3.37) and (3.38). This matrix will have the dimension $N \times N$, and will be excited with the current sources (3.40):

$$\begin{bmatrix} Y_s + Y_p & -Y_s & 0 & 0 & \ddots \\ -Y_s & Y_s + 2 \cdot Y_p & -Y_s & \ddots & 0 \\ 0 & -Y_s & \ddots & -Y_s & 0 \\ 0 & \ddots & -Y_s & Y_s + 2 \cdot Y_p & -Y_s \\ \ddots & 0 & 0 & -Y_s & Y_s + Y_p \end{bmatrix} \cdot \begin{bmatrix} V_1 \\ \\ \vdots \\ \\ V_n \end{bmatrix} = \begin{bmatrix} I_{source} \\ \\ \vdots \\ \\ I_{source} \end{bmatrix} \tag{3.41}$$

Once the system is solved, the velocities v_z are obtained for each node along the lateral dimension a. As a result, an electrical current intensity I is generated between the electrodes due to each electromechanical contribution, as:

$$I = (e \cdot dx \cdot b/t) \cdot \sum_{1}^{N_x} v_z(n), \tag{3.42}$$

and the acoustic contribution of the resonator's admittance is found using

$$Y_{lat} = I/U. \tag{3.43}$$

To obtain the total resonator impedance, the static capacitance (C_0), and the series resistance (R_s) to model the Ohmic losses on the electrode [15] are included, resulting in:

$$Z_{in} = R_s + \frac{1}{Y_{lat} + j\omega C_0}. \tag{3.44}$$

3.6.1.4 Comparison with FEM simulations

A simple ZnO membrane of 1.74 µm thickness and lateral dimension a equal to 80 µm is simulated in 2D using COMSOL. Losses are kept artificially low to achieve more pronounced spurious modes. The dispersive curves of the membrane are obtained with COMSOL following the procedure described in [26], and the curve corresponding to the TE_1 mode is fitted using the function described in (3.26).

Using the obtained dispersive phase constant, with $f_{001} = 1.787$ GHz, $c_{lamb} = 6745$, and $r = 1.955$, the lateral dimension of the resonator is modeled with $N_x = 80$. This number of discretizations is enough to ensure convergence of the model for these resonators. The boundary conditions are set on the two extremes of the lateral line, shorting the nodes of the Y-matrix that correspond to the boundaries. We refer to this kind of simulations as Quasi-2D simulations, since we are modeling only propagation in one direction and the characteristics of the propagation mode along the thickness direction are considered using the dispersive phase constant and the associated characteristic impedance of the TE_1 mode.

Figure 3.26 shows the fitting of the Quasi-2D model to the FEM simulation. The scaling of the characteristic impedance was fine-tuned with $a_{kz} = 0.9$. This can be justifiable because the characteristic impedance was derived for an isotropic layer. The electric permittivity (ε_r) and the piezoelectric constant are the same than those provided by COMSOL for ZnO. The attenuation constant of the dispersive line was set to $\alpha = 2000$ Np/m.

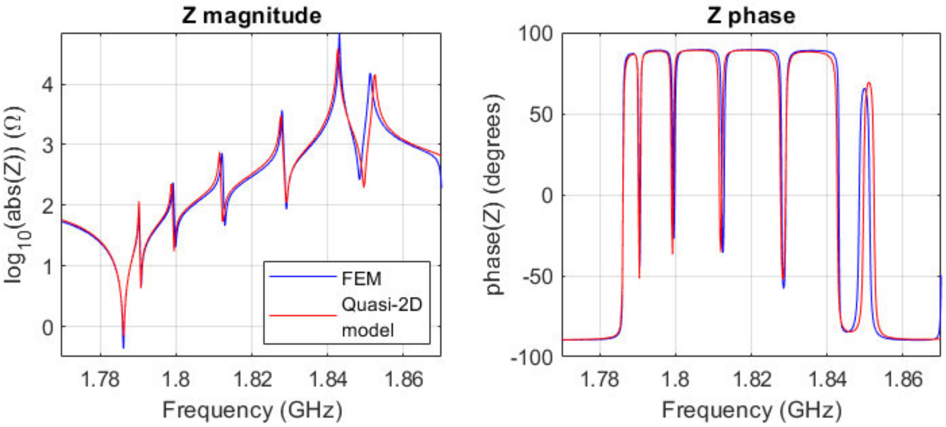

Figure 3.26: Magnitude and phase of the Impedance of the 2D FEM ZnO resonator (blue), and the Quasi-2D model (red).

The model was also tested simulating an AlN SMR resonator. FEM 2D simulations were performed with realistic losses in all layers in this case. The resonator has a top electrode comprised of Al, W layers and a SiN passivation layer, a bottom electrode of W and Al layers, and a Bragg reflector comprised of alternating SiO_2 and

W layers on a Si substrate. Its series resonance is around 2.48 GHz, and the k^2_{eff} is about 6.8%.

The dispersion curve was fitted with f_{001} = 2.48 GHz, c_{lamb} = 5740, and r = 2.05 and the attenuation constant was tuned to α = 7800 Np/m. FEM simulations unveiled displacements outside the active area at frequencies near the antiresonance frequency. These losses (lateral leakage) were modeled with a conductance of 0.3 mS connected at the boundary nodes. The fitting of the Quasi-2D model can be seen in Figure 3.27. In this case, the characteristic impedance was scaled using $a_{kz} = 0.5$.

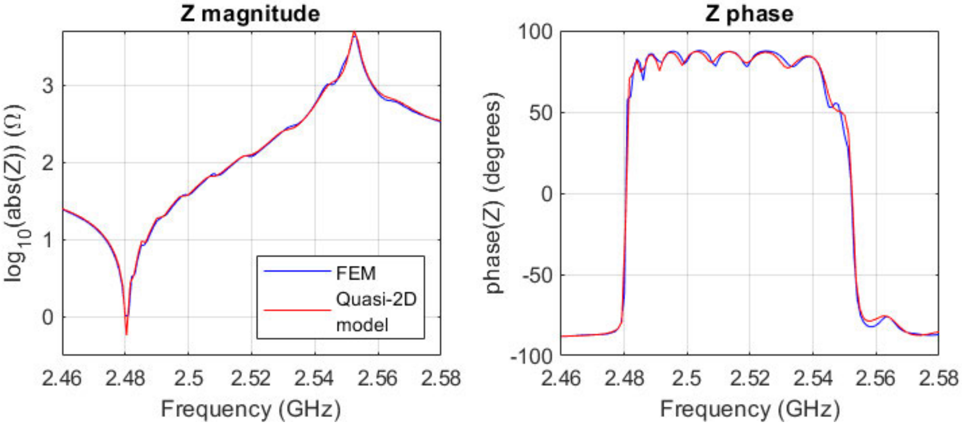

Figure 3.27: Magnitude and phase of the Impedance of the 2D FEM AlN SMR resonator (blue), and the Quasi-2D model (red).

3.6.2 Quasi-3D model

Once the quasi-2D approach has been verified, we will extend the basic idea for modeling resonators with arbitrary in-plane geometry. The Quasi-2D model can be extended to the other in-plane dimension using the Transmission Line Matrix (TLM) method [52]- [54]. We refer to this model as Quasi-3D model. The TLM method appears as a discrete implementation of Huygens' Principle, where the waves propagate along a mesh of transmission lines connected by nodes (Figure 3.29) [52]. When a node of the TLM mesh is excited, the energy spreads isotropically from the excited node. All the scattered fields along the mesh combine to form the overall waveform.

3.6.2.1 Unit cell

To add the other dimension, an additional transmission line is added. The new transmission line will have the same dispersive behavior, and the length of the lateral dimension b will be discretized in N_y elements of length $dy = b/N_y$. The cross-sectional area will be different for each propagating direction. It ends up being $A_{tb} =$

$dy \cdot t$ for the x-direction, and $A_{ta} = dx \cdot t$ for the y-direction. Note that this would allow emulating resonators with non-uniform shapes. In Figure 3.28, four nodes of the TLM mesh are shown. The impedances for each dimension are calculated considering dx, dy, and the different cross-sectional areas.

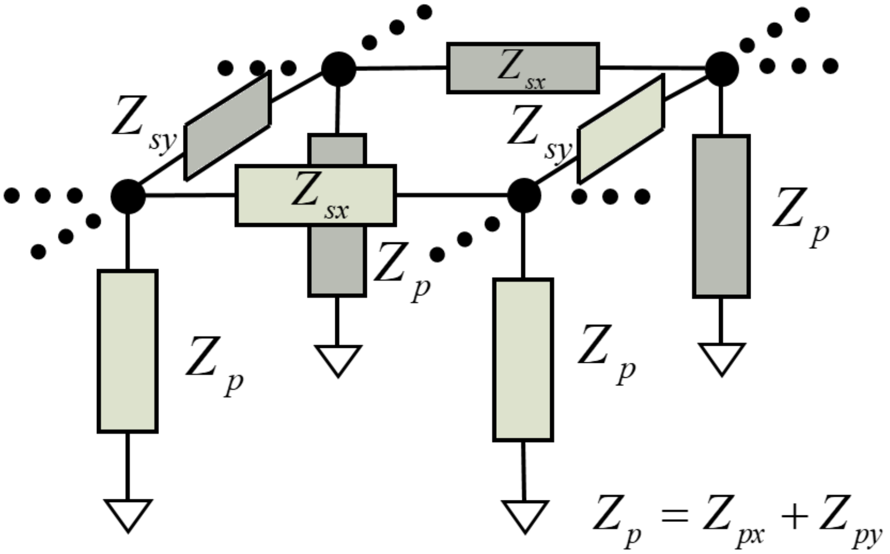

Figure 3.28: Equivalent Π-network of a dispersive transmission line on the x and y direction. Four nodes interconnected by different direction transmission lines are shown.

3.6.2.2 Losses and boundary conditions

Losses and boundary conditions are set as in the Quasi-2D model. A complex propagation constant is used in each propagation direction, and all the boundary nodes are shorted if not lateral leakage is considered or otherwise set with the correspondent conductance.

3.6.2.3 Implementation of the model

The resulting nodal Y-matrix has a size of $(N_x \times N_y)^2$, where N_x and N_y are respectively the discretizations along the x and y direction respectively. The node numbering is illustrated in Figure 3.29 for the sake of clarity.

The linear system of equations, extended version of (3.41), will be solved. However, note that excitation will be slightly different than the one described in (3.40), since now we must consider the discretization of the y-direction (dy), which results in:

$$I_{source} = e \cdot dx \cdot dy/t \cdot U. \tag{3.45}$$

Once the linear system is solved, the electric current generated between the electrodes is calculated as:

$$I = (e \cdot dx \cdot dy/t) \cdot \sum_{1}^{N_{tot}} v_z(n). \tag{3.46}$$

Finally, the electric input impedance of the resonator is calculated using (3.44), as it was done for the Quasi-2D model.

3.6.2.4 Quasi-3D Model vs. 3D FEM simulations

A 3D ZnO membrane with the same thickness than in the 2D case was simulated using COMSOL. Three different resonators with different in-plane geometries were simulated: a square resonator with area 80x80 µm^2, a rectangular resonator with area 80x100 µm^2 and a trapezoidal resonator with a height of 80 µm, and two bases of 40 µm and 80 µm, respectively. Losses are artificially kept much lower than in a real resonator to show highly coupled modes.

The phase constant and characteristic impedance of the TE$_1$ mode remains the same than the previously used in the Quasi-2D model (f_{001} = 1.787 GHz, c_{lamb} = 6745, r = 1.955, a_{kz} = 0.9, and α = 2000 Np/m) as they are assumed characteristics

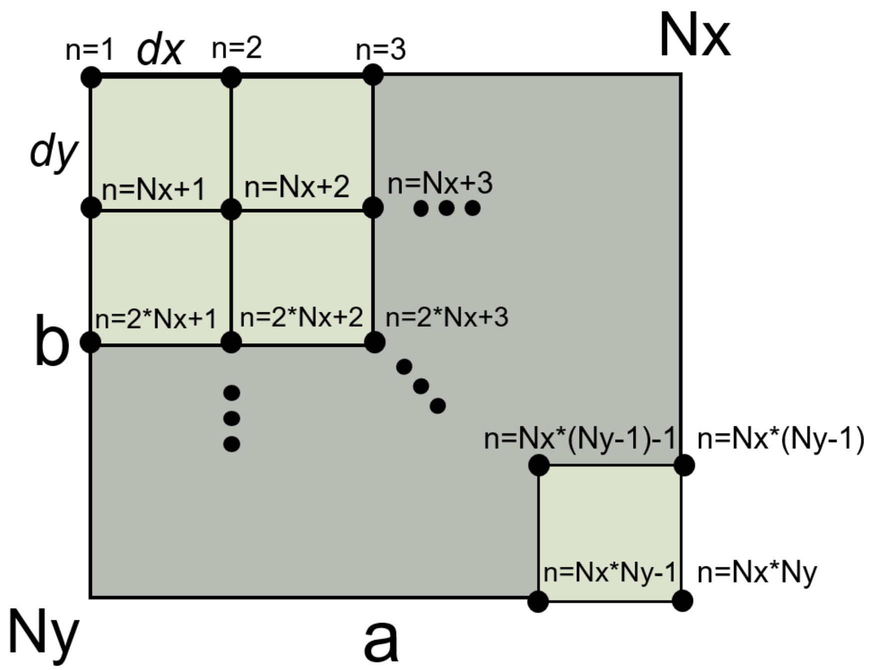

Figure 3.29: Schematic of a TLM mesh for a square resonator. The lateral dimensions a and b, and the number of discretizations in each direction (N_x and N_y) are indicated.

of the stack. The free stress lateral boundary conditions are applied at each edge node.

Figure 3.30 and Figure 3.31 show the electrical input impedances for the square and rectangular resonators respectively.

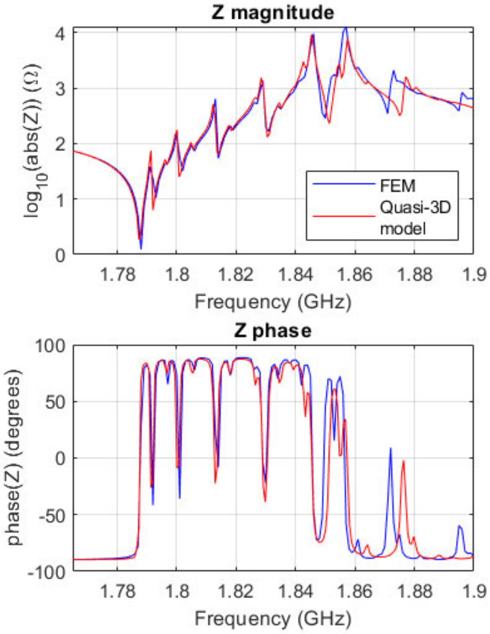

Figure 3.30: Magnitude and phase of the Impedance of the 3D FEM ZnO square resonator (blue), and the Quasi-3D model (red).

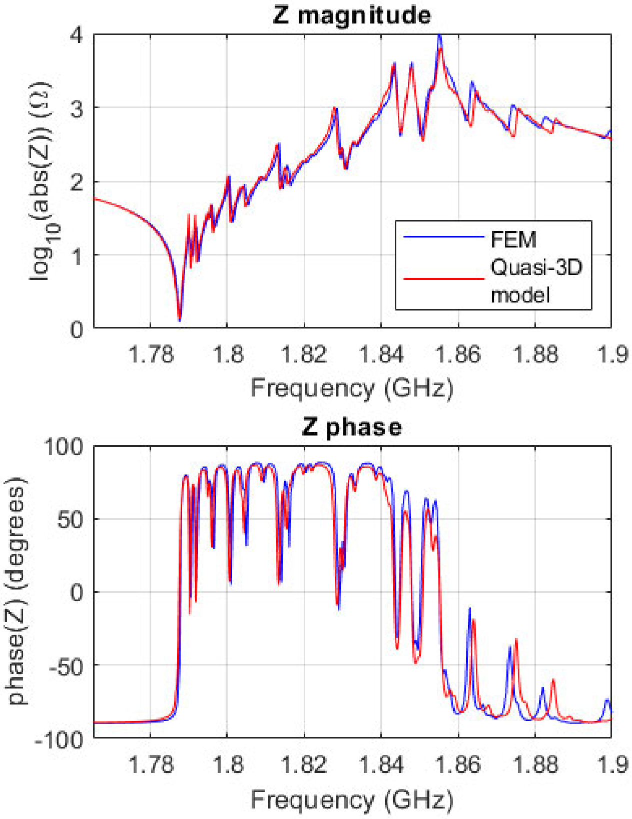

Figure 3.31: Magnitude and phase of the Impedance of the 3D FEM ZnO rectangular resonator (blue), and the Quasi-3D model (red).

Comparing Figure 3.26 with Figure 3.30, one can notice that although both are for the same square resonator, the latter has additional spurious modes. On the 2D model, constant displacement in the y-direction of the resonator was assumed, and only modes $m01$ were simulated, in both the FEM simulation and the Quasi-2D model. Adding the extra dimension y, allows simulating modes n different to zero. Those are the additional spurious modes appearing on Figure 3.30. In a square resonator, since $a = b$, the $mn1$ and the $nm1$ are degenerated modes, thus meaning that they occur at the same frequency. As an example, Figure 3.32 shows the resulting standing wave pattern of v_z of the mode 311 and 131 sharing the same frequency on a square resonator.

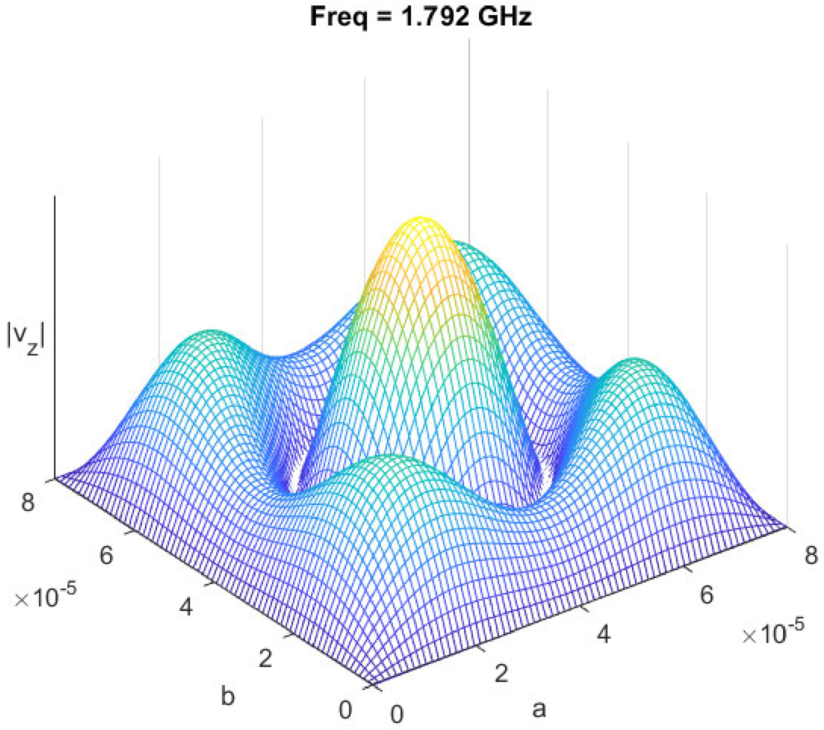

Figure 3.32: Standing wave pattern of $|v_z|$ at the frequency of mode 311 and 131 in the square resonator.

Notice that the rectangular resonator (Figure 3.31) shows more spurious modes, since $a \neq b$ and therefore the $mn1$ and the $nm1$ modes do not fall at the same frequency. In this case, and just for illustrative purposes, Fig. 3.33 shows v_z of the mode 311 showing three half wavelengths on the x-direction and one in the y-direction.

The electrical impedance of the trapezoidal resonator is shown in Figure 3.34. The Quasi-3D model shows good agreement with the FEM modeling. The number of discretizations has to be increased from the 80x80 used on the square and rectangular resonator, to 180x180 to achieve convergence of the simulation.

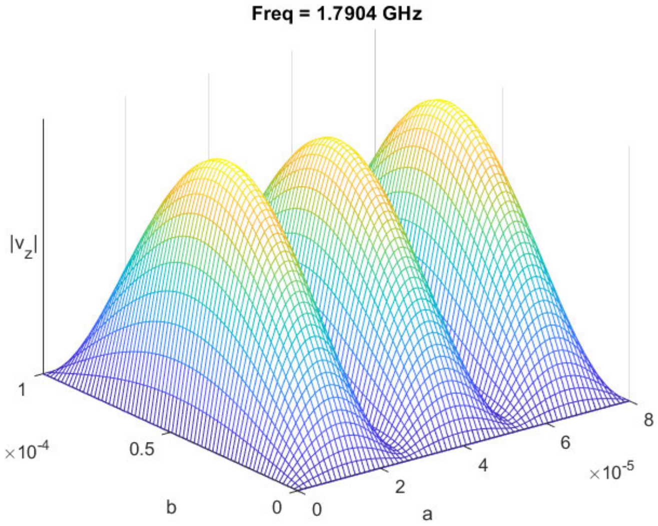

Figure 3.33: Standing wave pattern of $|v_z|$ at the frequency of mode 311 in the rectangular resonator.

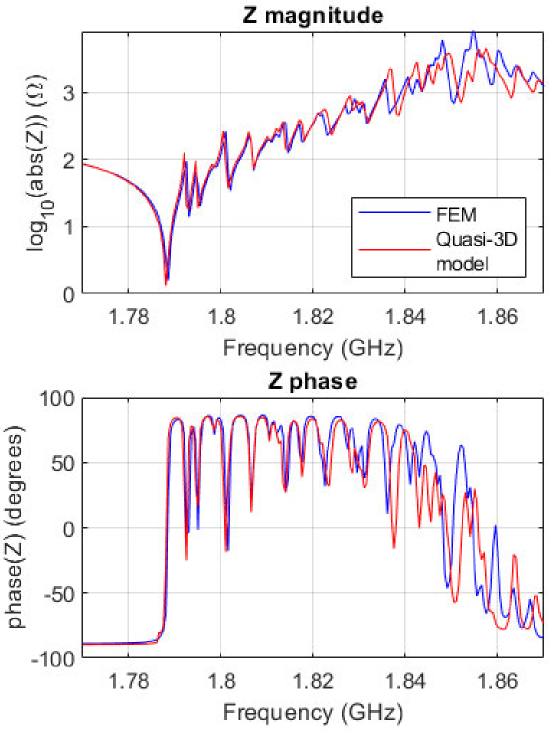

Figure 3.34: Magnitude and phase of the Impedance of the 3D FEM ZnO trapezoidal resonator (blue), and the Quasi-3D model (red).

The first four resonant modes of the trapezoidal resonator can be observed on Figure 3.35. The fundamental mode and the ones exhibiting three half-wavelengths on the larger dimensions can be clearly identified. The other mode cannot be defined as usually done in rectangular resonators since it is a combination of the scattering produced at the non-parallel interfaces.

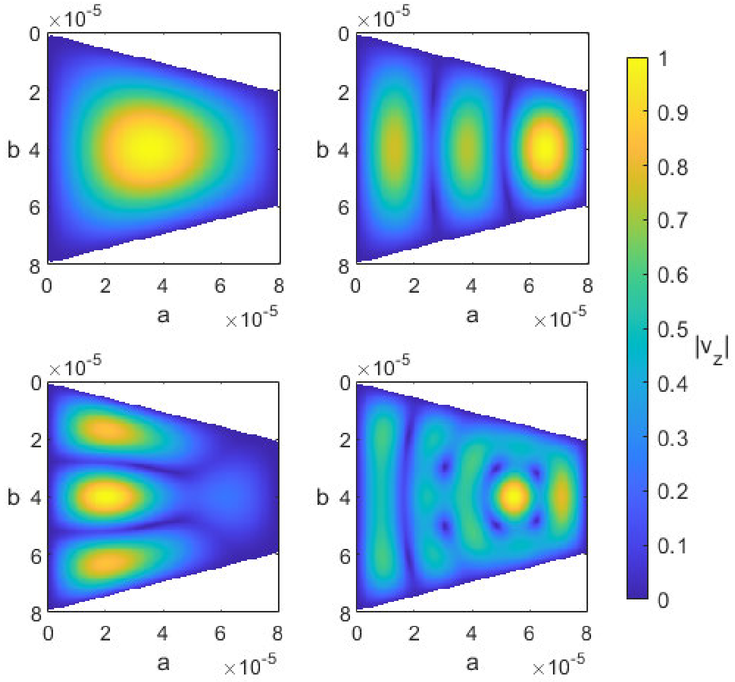

Figure 3.35: Standing wave pattern of normalized $|v_z|$ for the first four resonant modes of the trapezoidal resonator.

3.6.2.5 Computational time

Since the thickness dimension of the resonator does not have to be considered into the simulation, the number of Degrees of Freedom (DoF) is significantly reduced.

The computational time for both the FEM simulations and for our proposed model are presented in Table 3.1. They were calculated using the same number of frequency points, and achieving a mesh convergence in both cases.

For the Quasi-2(3)D model an additional FEM simulation needs to be performed to obtain the stack characteristics. But with a 2D simulation of around 100 frequency points is enough to obtain the dispersive curve and the electromechanical coupling.

The computational time is reduced several orders of magnitude between FEM and the TLM method. The 2D SMR case, shows a higher reduction due to the increase of DoF in the FEM simulations due to the discretization along the thickness dimension with many layers involved. Although the number of unknowns for modeling any arbitrary electrode shape, like the trapezoidal one, is increased, the time needed to perform the Quasi-3D simulation, continues being much lower than the one required for FEM simulations.

Note that, as can be seen in Table 3.1, the number of unknowns is independent of the resonator layers, making this method very suitable when working with SMR, since the same number of nodes are needed than for the FBARs.

We want to outline that the performance of the Quasi-3D method has room to be upgraded, since the 90% of the computational time in Matlab was taken by the assembling of the Y-matrices. In addition, any kind of symmetry was considered when using the TLM model, meanwhile in FEM simulations, symmetries where used when possible to reduce the amount of computational resources needed. The symmetry strategy is also noted in the Table 3.1.

Simulation	FEM (time [DoF])	Quasi-2(3)D Model (time [DoF])
ZnO membrane 2D $\frac{1}{2}$ *symmetry*	3 min 22 s [9300]	0.134 s [80]
SMR 2D $\frac{1}{2}$ *symmetry*	11 min 4 s [163391]	0.134 s [80]
ZnO membrane 3D $\frac{1}{4}$ *symmetry*	1 hour 52 min [215628]	42 s [6400]
ZnO trapezoidal 3D $\frac{1}{2}$ *symmetry*	2 hour 55 min [630752]	4 min 52s [32400]

Table 3.1: Comparison of computational times between FEM and the proposed model.

3.6.2.6 Evaluation of Quasi-3D simulations and measurements results

Four different SMR measurements were provided by the manufacturer of the devices for validating the model. The resonators have the same stack composition than the FEM simulated SMR. The resonators are made of two different areas (6400 µm^2 and 12900 µm^2), and two different aspect ratios (1 and 2).

The dispersion curve was fitted with $f_{001} = 2.48$ GHz, $c_{lamb} = 5180$, and $r = 2.2$. Although, the cut-off frequency of each resonator were slightly tuned (in the order of 100 ppm) to consider the tolerances of each resonator's layers. The other material constants were adjusted to $e = 1.51$, and $\varepsilon_r = 9.8$.

The propagation constant was set to $\alpha = 7800$ Np/m, the lateral leakage was modeled by means of a conductance in the lateral boundaries. Since in a 3D geometry, the lateral boundaries are discretized by N_x and N_y, the conductance connected at each node will be also divided by N_x or N_y. The conductance value used to fit the four resonators was $0.3/N_i$ mS.

The fitting of the Quasi-3D model to the four different measurements is shown in Figure 3.36-3.39. The model presents good agreement with the measurement near the fundamental frequency, but deviates slightly near the antiresonance. This can be due to slight tolerances on each resonator stack making the same curve unable to match the four different resonators.

The computational time necessary for the Quasi-3D SMR simulation stays the same than the required for FBARs (See Table 3.1).

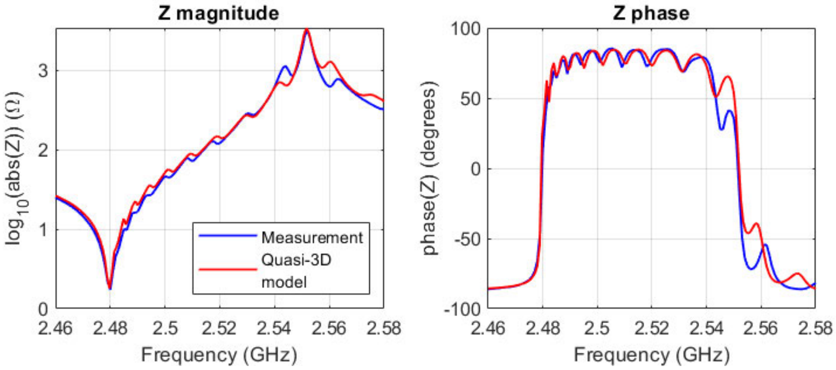

Figure 3.36: Magnitude and phase of the Impedance of the measured square SMR (A=6400 µm^2) (blue), and the Quasi-3D model (red).

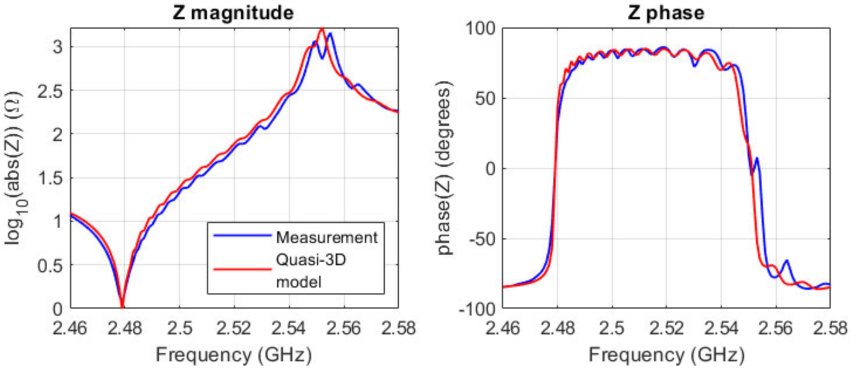

Figure 3.37: Magnitude and phase of the Impedance of the measured square SMR (A=12900 µm^2) (blue), and the Quasi-3D model (red).

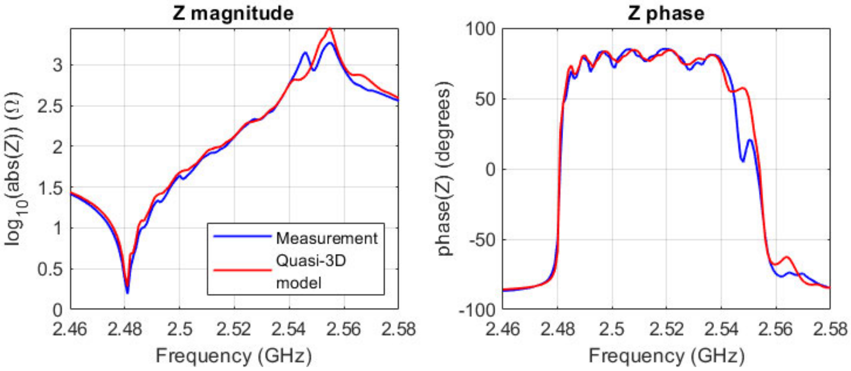

Figure 3.38: Magnitude and phase of the Impedance of the measured rectangular SMR (A=6400 µm^2) (blue), and the Quasi-3D model (red).

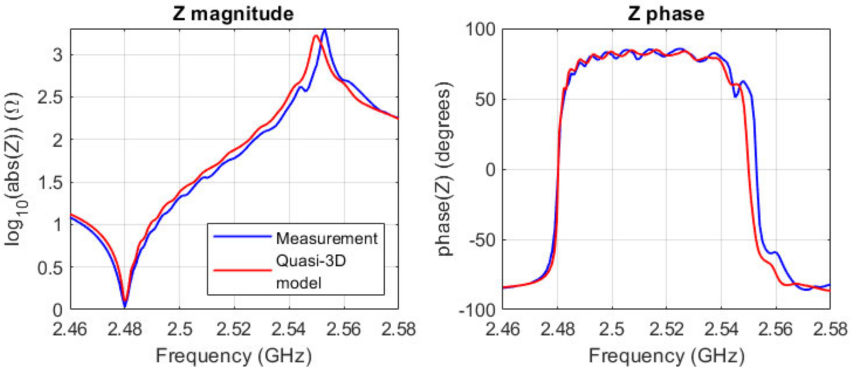

Figure 3.39: Magnitude and phase of the Impedance of the measured rectangular SMR (A=12900 µm^2) (blue), and the Quasi-3D model (red).

3.6.3 BAW resonators with Border Ring

On Section 3.1.2.2, the principle of the BR was explained for BAW resonators. In this section, the Quasi-3D model is extended to be able to model the BR effect on FBARs [55].

3.6.3.1 Quasi-2D Model Implementation

The implementation of the model is discussed thoroughly on the previous section. The model is divided into two different regions, the active region and the BR region. The non-active region will be modeled as a boundary condition. The phase constant and the Z_0 are different for each of the regions. At Figure 3.40, the disposition of each node for a 2D resonator with N_x nodes for the active region, and N_{BR} nodes for the BR region. Notice how the BR region is situated at the start and the end of the

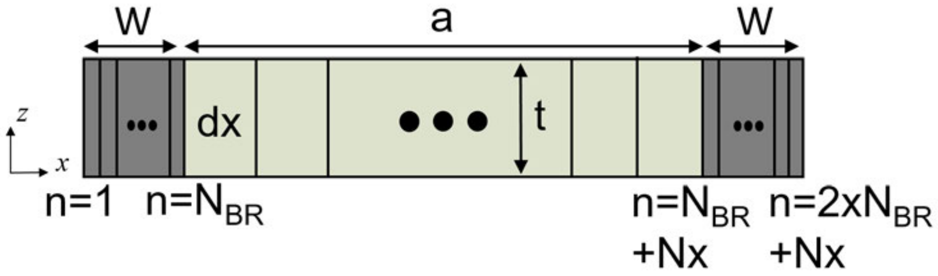

Figure 3.40: Two-dimensional resonator in the xz-plane. The x-dimension is discretized in N_x elements.

active region. A Y-matrix connecting all the nodes of the resonator is generated with the impedances (3.37)-(3.39) of each unit cell.

The admittance matrix generated is excited with the following distributed current sources at each node 3.40. Notice that dx may be different for each region, so the excitations for the active and BR regions may differ. This current source represents the force generated by the electric potential (U) applied on the electrodes.

Solving the system and obtaining the particle velocities v_z along the resonator's lateral dimension, the electric current between the electrodes is calculated with (3.42). As it happens with the excitation the contributions of each of the regions to (3.42), may be calculated separately depending of the discretizations per region.

The input impedance (Z_{in}) of the resonator is finally obtained with the use of (3.43) and (3.44).

3.6.3.2 Lateral boundary conditions

In the homogeneous electrode case, a short-circuit was enough to model the boundary condition of $v_z = 0$, equivalent of having $\beta_o = \infty$. In the case of BAW resonator's with BR it is needed that the β_o is correctly modeled. Therefore, at the boundary nodes the characteristic impedance (Z_0) of the non-active region needs to be defined, this impedance will model the behavior of the non-active region.

3.6.3.3 Obtainment of the dispersion curves

The dispersion curves of the stack are obtained from FEM simulations of the different stacks. The dispersive curves for the active region are obtained from eigenmode simulations following [26]. Once the TE_1 mode is identified, equation (3.26) is fitted to the curve to obtain β_a. The same process is applied for the BR region and β_{BR}.

For the non-active region, a different procedure is used. From FEM simulations of a 2D BAW resonator with its non-active region, the displacement profiles are obtained on top of both regions. To suppress reflections at the end of the non-active region that will lead to an incorrect displacement profile a Perfectly Matched Layer (PML) is applied at both ends of the resonator [56].

Following the procedure described in [57], the displacements of the non-active region are fitted to the exponential function:

$$A(x) = A_0 + A_1 e^{-|k_x|x}, \tag{3.47}$$

here A_0, A_1 and k_x are the fitting coefficients. Each wavenumber k_x is extracted at different frequency points, generating the dispersion curve of the evanescent mode (Fig. 8). Then, an ellipsoid is fitted to the obtained data points:

$$\beta_o(f) = -j \cdot \Re\left[\frac{k_{max}}{\Delta f}\sqrt{\Delta f^2 - (f - f_0)^2}\right], \tag{3.48}$$

the constants f_0, Δf, and k_{max} can be seen on Fig. 8 and are determined by the fitting.

In Figure 3.41, the dispersive curve of the non-active region of a BAW resonator is shown. the values of $|k_x|$ obtained by the fitting of (3.47) are shown with asterisks. The approximation using (3.48) is shown by the solid black line in the evanescent region, the TE_1 mode is fitted with (3.26). The main parameters of (3.48) are represented on the figure.

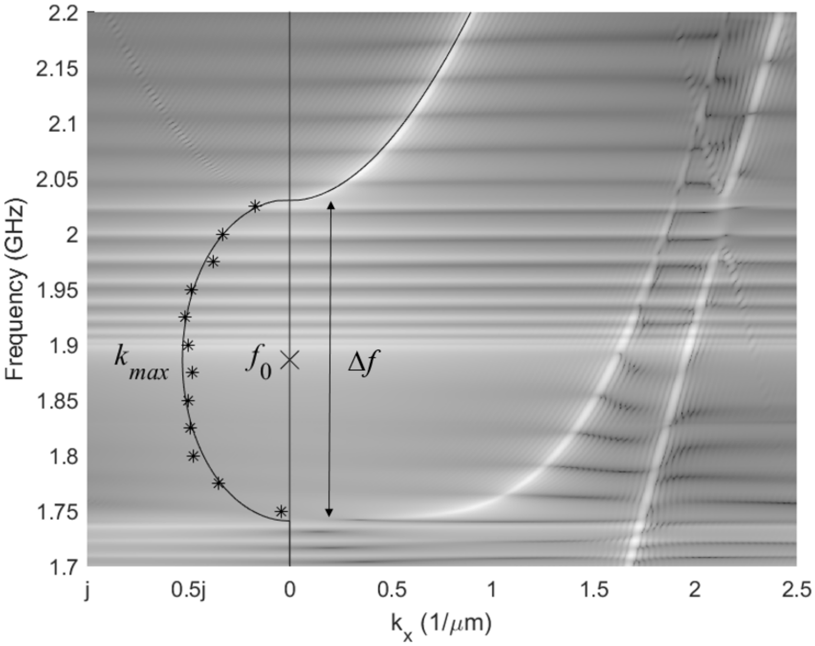

Figure 3.41: Dispersive curves of the non-active region.

3.6.3.4 Quasi-2D model vs. 2D FEM simulations

The model is validated using 2D FEM simulations of a ZnO Film Bulk Acoustic Resonator (FBAR) with Aluminum electrodes. The piezolayer has a thickness of 1.52 µm. The electrodes have a thickness of 100 nm, and the top electrode has a length of 80 µm, limiting the active region to that size.

A BR was also added, it consists of a region of Aluminum with an increased thickness of 165 nm. Resonators with three different BR widths of 7.5 µm, 10 µm, and 12.5 µm are simulated.

The simulations of the FBARs were done with COMSOL, keeping the loss factor low to achieve more pronounced spurious modes. The dispersion curves of the resonator are obtained as in the previous section.

For the FBAR without BR, the dispersion curve of the active region was adjusted with f_{001} = 1.898 GHz, c_{lamb} = 6200, and r = 1.85. The lateral dimension of the resonator was discretized with $N_x = 80$. This number is enough to ensure the convergence of the applied mesh.

Two impedances are set at the lateral boundaries these impedances have the value of the non-active region Z_0. The dispersive curve of the non-active region is fitted with $f_0 = 1.886$ GHz, $\Delta f = 145$ MHz, and $k_{max} = 0.53$ 1/µm.

Figure 3.42 shows the fitting of the Quasi-2D model to the 2D FEM simulation. The characteristic impedance of the active section is scaled to $a_{kz} = 0.93$, meanwhile the one of the non-active region to $a_{kzna} = 1.7$. The electric permittivity (ε_r) and the piezoelectric constant are the same than the provided by COMSOL for ZnO. The attenuation constant was set to $\alpha = 3000$ Np/m.

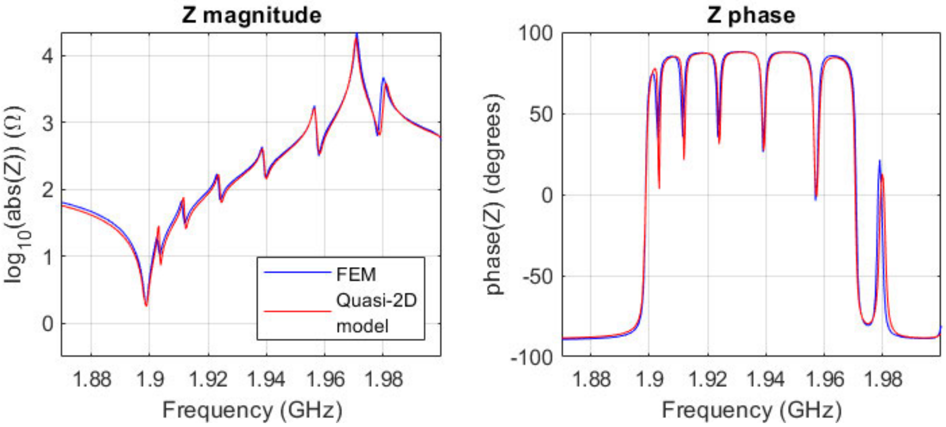

Figure 3.42: Magnitude and phase of the Impedance of the 2D FEM ZnO resonator (blue), and the Quasi-2D model (red).

For the resonators with BR, in addition to the previous simulations, the BR region was added with $N_{BR} = 20$ for the three different lengths. The dispersion curve of the BR was fitted to $f_{001} = 1.857$ GHz, $c_{lamb} = 6100$, and $r = 1.835$. The scaling factor applied to the characteristic impedance was $a_{kzBR} = 0.95$.

In Figure 3.43 to Figure 3.45, the results of the Quasi-2D model applied to different BR widths can be seen. The model shows good agreement of the spurious mode suppression, and the generation of the spurious BR fundamental mode.

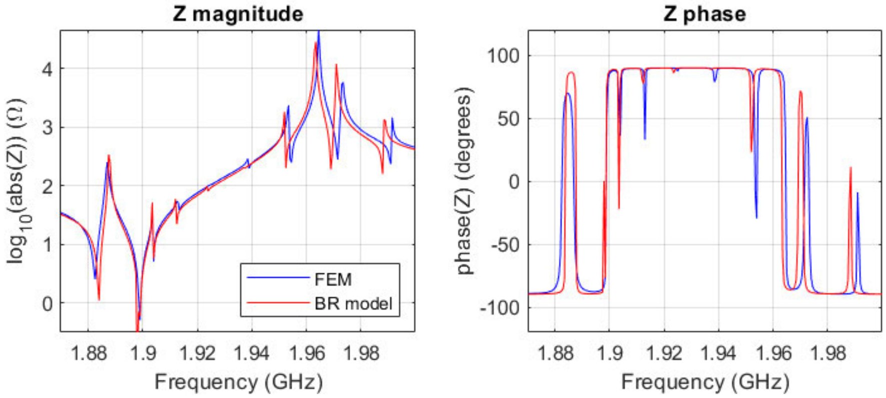

Figure 3.43: Magnitude and phase of the Impedance of the 2D FEM ZnO with a BR of 7.5 µm (red).

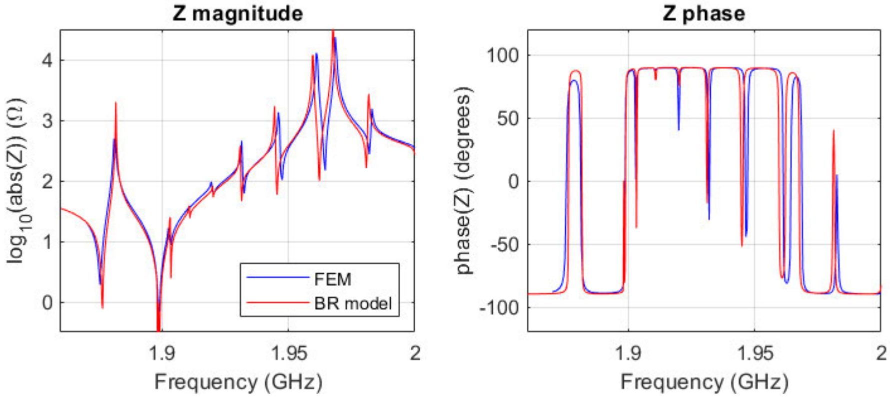

Figure 3.44: Magnitude and phase of the Impedance of the 2D FEM ZnO with a BR of 10 µm (red).

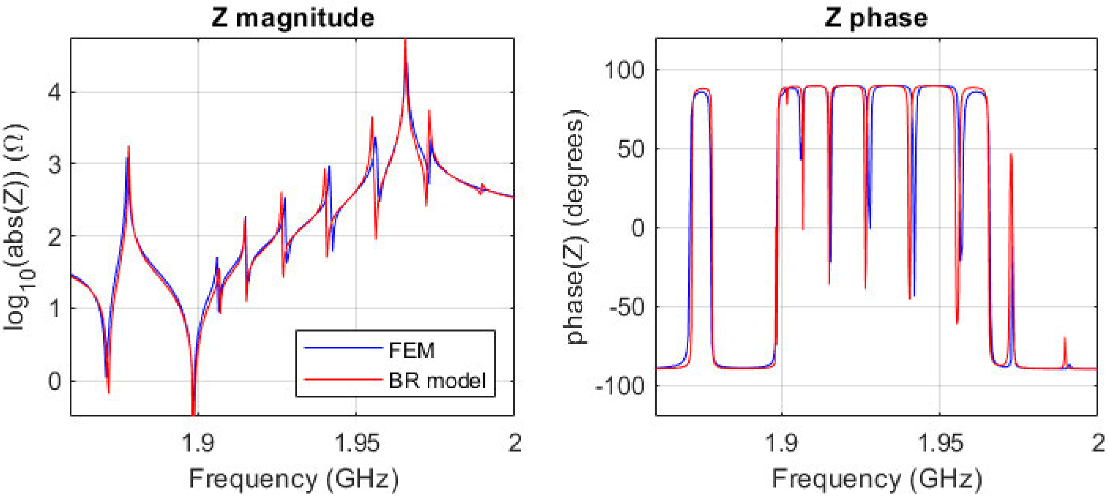

Figure 3.45: Magnitude and phase of the Impedance of the 2D FEM ZnO with a BR of 12.5 µm (red).

3.6.3.5 Implementation of the Quasi-3D model for BR

The previous Quasi-2D model can be extended to an additional dimension by means of the Transmission Line Matrix (TLM) method [50]. The details of the implementation can be seen in Section 3.6.2.

Notice that this time the dependence of dx and dy with the discretization of each electrode region, making it convenient to define it for each region. The electric input impedance of the resonator is obtained using (3.45), (3.46), (3.43), and (3.44).

3.6.3.6 Quasi-3D Model vs. 3D FEM simulations

A square 3D FBAR comprising the same stack than in section III was simulated using COMSOL. The dimensions of the top electrode were 80x80 µm^2. In Figure 3.46, the 3D FEM is compared with the Quasi-3D model, showing good agreements. The parameters used to fit the model are the same than the ones used for the Quasi-2D model.

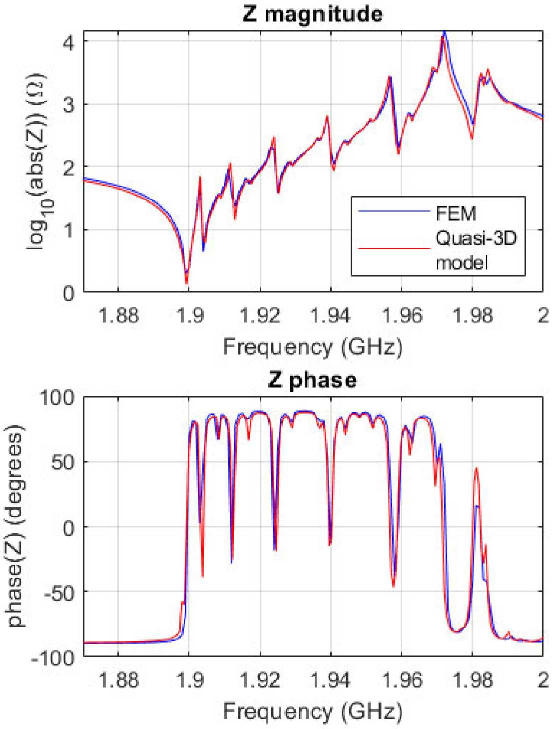

Figure 3.46: Magnitude and phase of the Impedance of the 3D FEM ZnO square resonator (red).

Four more resonators were used to validate the BR. Two square resonators of 80x80 µm^2, and two rectangular resonators of 80x100 µm^2. Both with BR widths of

7.5 µm and 10 µm. The comparison between the FEM simulations and the Quasi-3D model show good agreement using the same exact parameters than the determined in the 2D case Figure 3.47-3.50. The active region was discretized with $N_x = 80$, and $N_y = 80$, while the BR region was discretized with $N_{BR} = 20$.

The Quasi-3D model outperforms the 3D FEM simulations in computational time. Quasi-3D simulations take about 3 minutes to compute 201 frequency points, in the other hand 3D FEM simulations of 1/4 of the resonator take about 6 hours for the same frequency points.

In [50] it was demonstrated that the TLM method could be applied to arbitrary electrode shapes of BAW resonators. This method enables for very fast simulations of different electrode shapes with BR.

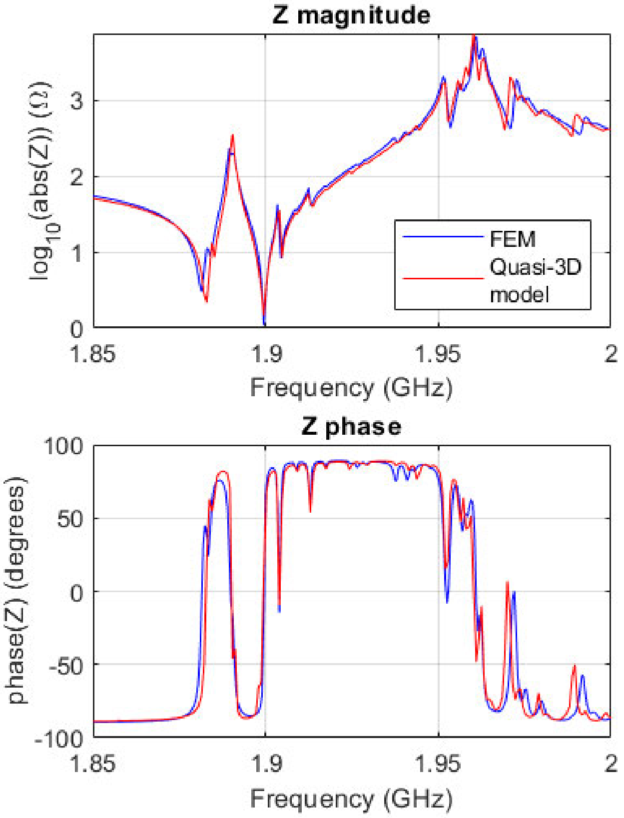

Figure 3.47: Magnitude and phase of the Impedance of the 3D FEM ZnO square resonator with 7.5 μm BR (red).

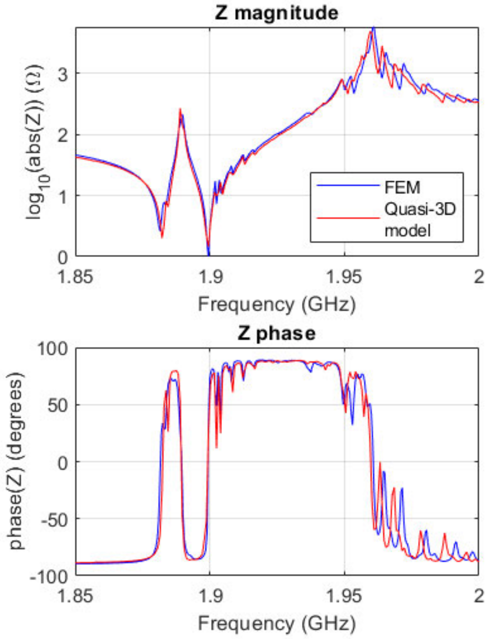

Figure 3.48: Magnitude and phase of the Impedance of the 3D FEM ZnO rectangular resonator with 7.5 μm BR (red).

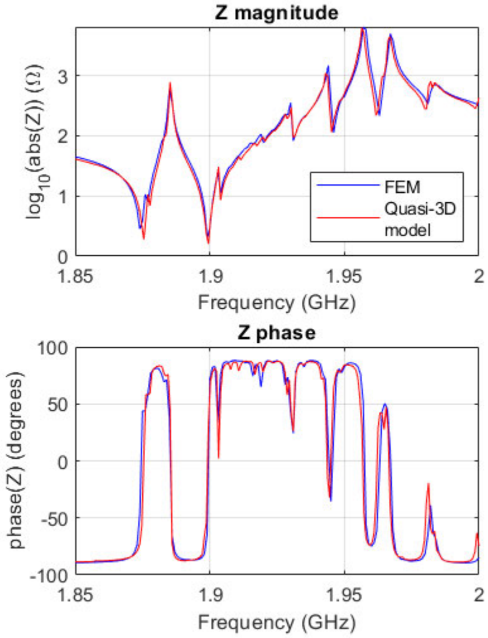

Figure 3.49: Magnitude and phase of the Impedance of the 3D FEM ZnO square resonator with 10 μm BR (red).

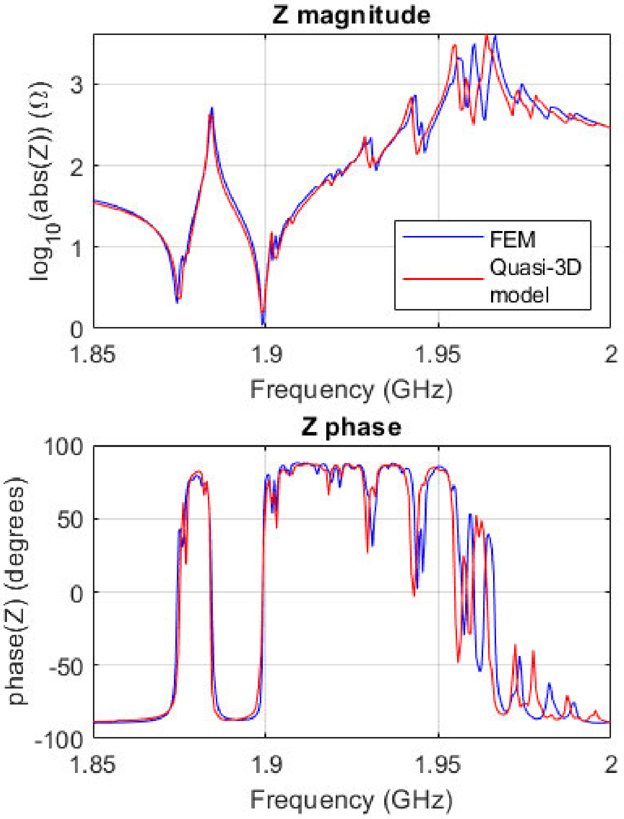

Figure 3.50: Magnitude and phase of the Impedance of the 3D FEM ZnO rectangular resonator with 10 μm BR (red).

3.7 Conclusions

The first part of this chapter deals with the physics of Lamb wave. The theory developed in that section gives the reader a good starting point for the mechanisms that generate the spurious resonances and their suppression.

The first model introduced was a modification of the Mason model with a transmission line for modeling the lateral dimension of the resonator. This model serves as a basis for the work developed across this chapter.

First the model was used to give an explanation of the spurious resonances below the fundamental frequency. They are generated by the Border Ring on an SMR resonator exhibiting Type I dispersion. From this study it is concluded that they are caused by the lateral propagation of an acoustic mode with a lower cutoff frequency than the TE_1.

The Mason with the lateral transmission line can also be modified to model the nonlinear behavior of the resonator. In Section 3.4, the piezoelectric constitutive relations are expanded to higher order terms to model the H2 emissions due to the lateral spurious resonances.

Finally a new approach based on the TLM method for acoustic resonances is presented. It is able to model any electrode in-plane geometry. This way three-dimensional modeling of BAW resonators can be performed even for apodized geometries and Borer Ring.

Chapter 4

Thermoelastic Damping Model

In this chapter thermal effects on BAW resonators are introduced. The thermo-electro-mechanical constitutive relations are derived for a piezoelectric solid and the mechanism for thermoelastic damping is given to the reader. In the following section a Mason based model for thermoelastic damping (TED) is presented. This model is meant to work for different types of BAW resonators independently of their resonance frequency and composition.

In order to validate the model different experiments were performed. The first one tries to explain the behavior of the Q factor at cryogenic temperatures. Two different BAW resonators are measured down to 100 K. The measurements are fitted to a Mason model with viscoelastic losses and to a Mason model incorporating the thermoelastic damping.

The next set of experiments are performed at ambient temperature. In this case, the Q factor of the different outband spurious resonances generated in the Bragg reflector layers is analyzed. Here, the Mason with thermoelastic damping is compared to the classical Mason with viscoelastic damping. The aim of this experiment is to give more accurate predictions at higher frequency resonances than the ones provided by the Mason model with viscoelastic losses.

4.1 Thermo-electro-mechanical behavior of BAW resonators

In Chapter 2, the interaction of the elastic and the mechanical domain was explained by the piezoelectric effect via its constitutive relations. There, they were simplified assuming that there were no changes on the entropy, decoupling the thermal domain from the equation.

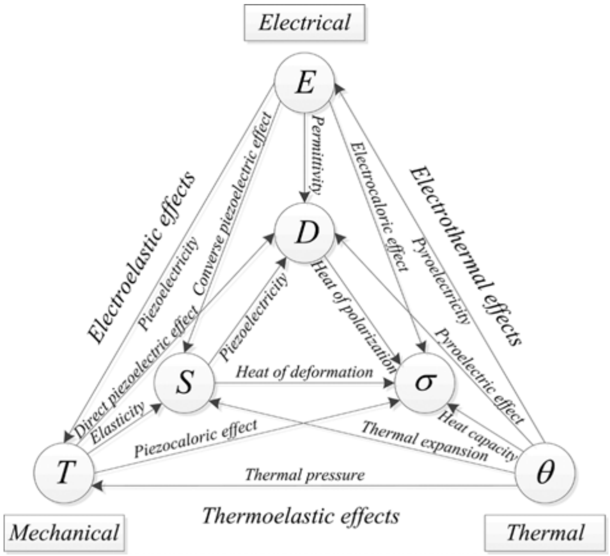

Figure 4.1: Heckmann diagram showing the interaction between the intensive variables (T, E, and Θ), and the extensive ones (S, D, and σ) [18].

On a real BAW resonator, those interactions (Figure 4.1) cannot be omitted. So as done before, a new set of constitutive relations can be derived from equilibrium thermodynamics [18]. Since we are dealing with in-line excited bulk waves the electric magnitude that remains constant is the electric displacement (D). Also, for further convenience temperature will be used as the third independent variable. For these reasons, and assuming no residual stresses and strains, the Free energy ($A = U - \sigma\Theta$) [25] will be used to obtain the constitutive relations following:

$$dA = TdS + EdD - \sigma d\Theta \tag{4.1}$$

$$T = \frac{\partial A}{\partial S}; \quad E = \frac{\partial A}{\partial D}; \quad d\sigma = \frac{\partial A}{\partial \Theta} \tag{4.2}$$

$$T = \frac{\partial T}{\partial S}dS + \frac{\partial T}{\partial D}dD + \frac{\partial T}{\partial \Theta}d\Theta \tag{4.3}$$

$$E = \frac{\partial E}{\partial S}dS + \frac{\partial E}{\partial D}dD + \frac{\partial E}{\partial \Theta}d\Theta \tag{4.4}$$

$$d\sigma = \frac{\partial \sigma}{\partial S}dS + \frac{\partial \sigma}{\partial D}dD + \frac{\partial \sigma}{\partial \Theta}d\Theta \tag{4.5}$$

Tensor indices were dropped from the previous expressions, anyway they imply summation over all indices. Assuming that the Free energy is a perfect differential, the following Maxwell relations can be established:

$$\frac{\partial E}{\partial S} = \frac{\partial T}{\partial D}; \quad \frac{\partial T}{\partial \Theta} = -\frac{\partial \sigma}{\partial S}; \quad \frac{\partial E}{\partial \Theta} = -\frac{\partial \sigma}{\partial D} \tag{4.6}$$

from them, the partial derivatives can be defined as: $\dfrac{\partial T}{\partial S} = c^{D\Theta}$, $-\dfrac{\partial T}{\partial D} = h^{\Theta}$, $\dfrac{\partial E}{\partial D} = \beta^{S\Theta}$, $\dfrac{\partial T}{\partial \Theta} = -\lambda^{SD}$, $\dfrac{\partial E}{\partial \Theta} = \tau^{SD}$, and $\dfrac{\partial \sigma}{\partial \Theta} = \dfrac{\rho_m C_v^{\Theta}}{\Theta}$. Here $h^{\Theta} = e/\varepsilon^{S}$, $\beta^{S\Theta}$ is the inverse of the permittivity of the medium, λ^{SD} is the temperature coefficient of the stress, τ^{SD} is the pyroelectric tensor, and C_v^{Θ} is the heat capacity at constant volume (do not confuse the subscript v with a tensor index).

Extending the equations above to tensor notation, the constitutive relations can be set as:

$$T_i = c_{ij}^{D\Theta} S_j - h_{ik}^{\Theta} D_k - \lambda_i^{SD} d\Theta \tag{4.7}$$

$$E_l = -h_{lj}^{\Theta} S_j + \beta_{lk}^{S\Theta} D_k - \tau_i^{SD} d\Theta \tag{4.8}$$

$$d\sigma = \lambda_j^{SD} S_j - \tau_k^{SD} D_k + \frac{\rho_m C_v^{\Theta}}{\Theta} d\Theta \tag{4.9}$$

Notice how the negative sign must be imposed in the definition of λ to keep it positive. From physical observations it can be seen than, when the temperature increases, a negative stress (compression) must be applied to keep the strain constant if the thermal expansion is assumed to be positive.

4.1.1 Relation between temperature coefficient of stress an linear thermal expansion

From the constitutive relations derived from the Gibbs function (with T, E, and Θ as independent variables), we can establish a relation between the temperature coefficient of stress derived from the previous constitutive relations, and the coefficient of linear thermal expansion (See Appendix A):

$$\lambda_i^{SD} = c_{ij}^{E\Theta} \alpha_j^{E} - p_m^{SE} h_{mi}^{\Theta} \tag{4.10}$$

If pyroelectricity p^{SE} is neglected, it turns out to an equal expression that the one for a non-piezoelectric solid derived also in [25]:

$$\lambda_i^{SD} \approx \alpha_j^{E} c_{ji}^{E\Theta}. \tag{4.11}$$

4.1.2 Thermoelastic damping in BAW resonators

If a solid is under compression, some of its mechanical energy will get converted into thermal energy, this way compressed parts of the solid will become warmer than the expanded parts (Figure 4.2). In adiabatic conditions, the heat that increases due to the compression of the solid under harmonic excitation is reabsorbed later by the solid expansion. Since the heat stays locally in the solid no energy losses are accounted. If

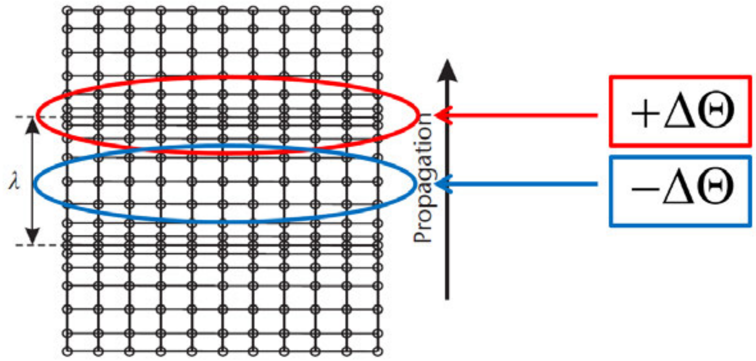

Figure 4.2: Longitudinal wave, the changes of temperature (Θ) at the compressed and expanded regions are illustrated [3].

the local adiabatic conditions are broken, heat can flow between the hot and the cold parts, extracting energy from the vibration [12].

Neglecting pyroelectricity from the constitutive relations (4.7)-(4.9) and supposing displacement only in the z-direction, they end up as:

$$T_3 = c_{33}^{D\Theta} S_3 - h_{33}^{\Theta} D_3 - \lambda_3^{SD} d\Theta \tag{4.12}$$

$$E_3 = \beta_{33}^{S\Theta} D_3 - h_{33}^{\Theta} S_j \tag{4.13}$$

$$d\sigma = \lambda_3^{SD} S_3 + \frac{\rho_m C_v^{\Theta}}{\Theta} d\Theta. \tag{4.14}$$

From (4.14), the quasi-static heat density in the body can be derived:

$$\delta Q = \Theta d\sigma = \Theta \lambda_3^{SD} S_3 + \rho_m C_v^{\Theta} d\Theta, \tag{4.15}$$

where δ is an imperfect differential [16]. This heat will propagate following the Fourier law:

$$\mathbf{q} = -k \nabla \Theta \tag{4.16}$$

here, $\mathbf{q}$ is the heat flux, and k is the heat conductivity of the solid. The heat conservation law imposes that

$$\delta \dot{Q} = -\nabla \cdot \mathbf{q}. \tag{4.17}$$

Identifying the strain contribution of (4.15) as $\delta Q_S = \Theta \lambda_3 S_3$ and using (4.15)-(4.17), the heat equation is derived:

$$\rho_m C_v^{\Theta} \frac{\partial \Theta}{\partial t} = k \frac{\partial^2 \Theta}{\partial z^2} - \frac{\partial Q_S}{\partial t}. \tag{4.18}$$

The rate of heat production on (4.18) will be simply calculated as

$$\frac{\partial Q_S}{\partial t} = \lambda_3 \frac{\partial (\Theta S_3)}{\partial t}. \tag{4.19}$$

The strain and the temperature are functions of time, while the thermal coefficient of stress remains time independent. Since we are interested in the small variations of temperature in function of time, the total temperature Θ can be represented as the following:

$$\Theta = \Theta_0 + d\Theta = \Theta_0(1+\theta) \tag{4.20}$$

here θ represents the small harmonic variations of temperature due to the thermoelastic effect. Applying (4.20) to (4.19), the rate of hate production ends as

$$\frac{\partial Q_S}{\partial t} = \lambda_3 \frac{\partial(\Theta S_3)}{\partial t} = \lambda_3 \frac{\partial(S_3\Theta_0 + S_3\Theta_0\theta)}{\partial t} = \lambda_3\Theta_0 \left(\frac{\partial S_3}{\partial t} + \frac{\partial(S_3\theta)}{\partial t}\right). \tag{4.21}$$

Since we are dealing with small harmonic motions, we can neglect the higher order contribution $\left(\frac{\partial(S_3\theta)}{\partial t}\right)$. Finally after a few manipulations we arrive to the heat equation for a thermoelastic body:

$$\rho_m C_v^\theta \frac{\partial\theta}{\partial t} = k\frac{\partial^2\Theta}{\partial z^2} - \lambda_3\frac{\partial S_3}{\partial t}. \tag{4.22}$$

The injected heat will flow to cooler areas, generating an energy loss of the mechanical wave and its consequent attenuation. This attenuation takes part mainly in longitudinal modes due to its changes in volume, for higher frequencies, the path between the solid's compressed and extended parts gets shorter, and become easier to the heat to get propagated. Because of that the attenuation per unit of length becomes proportional to the square of the frequency, being the main attenuation source at high frequencies [12].

4.2 Mason based model for TED

On [18], Rocas et. al. presented a circuital model of a BAW resonator based on the Mason model. Their model was able to model thermal effects and the nonlinearities arising in BAW resonators, but TED was not included into the model. In Rocas' model the piezoelectric effect is modeled by a discrete Mason model made by lumped components, and it is coupled to a thermal network that models the heat propagation along the thickness direction of the resonator (Figure 4.3). In order to simulate a multilayered resonator, each cell of each material is connected between them in a similar way as it is done for Mason model in Chapter 2.

In that paper, no heat was injected nor subtracted from the thermal network when the solid was expanded or contracted. The model only took into account the temperature of the medium, and the heat dissipated by the viscoelastic effect.

[redacted]

Figure 4.3: Block diagram of a piezoelectric cell coupled to the thermal network. For the thermoelastic damping case: $\Delta T = -\lambda d\Theta$ [18].

4.2.1 Non-piezoelectric layers

In order to model the non-piezoelectric layer, Hooke's law and the Newton's second law, need to be developed leading to similar expressions than those of the Telegrapher's equations. From these equations a lumped circuital model for a transmission line can be derived. The term T_C, modeling an additional stress source, is added to Hooke's law in order to model the thermoelastic effect.

[redacted] (4.23)

[redacted] (4.24)

Notice how $v_3 = \dot{u}_3$ stands for the particles velocity on the thickness direction while V stands for the electric potential, and I stands for the electric current intensity. The equivalent circuit cell is shown in Figure 4.4.

The values of the lumped components are calculated by:

[redacted], (4.25)

[redacted]. (4.26)

Here Δz is a small length along thickness direction, $\Delta z \to 0$. And can be defined as:

$$\Delta z = \frac{\text{thickness}}{N}, \tag{4.27}$$

[redacted]

Figure 4.4: Lumped transmission line model for acoustic waves with an added VCVS for modeling the TED [18].

where N is the number of discretizations per material layer. The value of the voltage controlled voltage source (VCVS) T_C, goes really straight forward looking at the constitutive relation (4.7):

$$[redacted] \tag{4.28}$$

4.2.2 Piezoelectric layer

For the piezoelectric layer the Mason lumped model is used. It is derived in the same way that the non-piezoelectric one, but adding another term for the piezoelectric effect taking into account the electro-acoustic coupling (see (2.42) to (2.45)). In the piezoelectric case and due to the piezoelectric stiffening, the lumped capacitance is calculated as:

$$[redacted] \tag{4.29}$$

where

$$[redacted] \tag{4.30}$$

The equivalent circuit cell for the piezoelectric layers can be seen on Figure 4.5. Here, a transformer with the turn ratio $-Ae/\Delta z : 1$, and the distributed static capacitance $C_0 = A\varepsilon/\Delta z$ are added. Each of these cells represents a tiny portion of the piezolayer thickness.

4.2.3 Thermal network

For the thermal network, an equivalence between the heat equation (4.22) and the differential equation of a lumped RC transmission line can be done:

$$[redacted], \tag{4.31}$$

[redacted]

Figure 4.5: Lumped Mason model for the piezolayer with an added VCVS for modeling the TED [18].

Where temperature Θ can be related with the electric potential V, and the electric current intensity I with heat rate $\mathbf{q}$ (4.17). It is clear then, that we can introduce heat to our thermal network by using a current controlled current source (CCCS).

[redacted]

Figure 4.6: Implemented thermal network. The current source $Q_{\Delta z}$ models the current added to the mode [18].

The equivalent network for the heat equation can be seen on Figure 4.6. The values of the resistor and the capacitor can be calculated with:

[redacted] (4.32)

[redacted] (4.33)

To calculate the injected heat $Q_{\Delta z}$, we should go back to expression (4.22), since we are interested in harmonic variations of the temperature ($\Theta = \Theta_0 + d\theta$), and we are also assuming harmonic variations of the strain, expression (4.22) ends up in phasor form as:

[redacted]. (4.34)

Where Θ is the room temperature, and the dynamic variations of temperature are driven by the strain induced temperature changes. Since the last equation is per unit of volume it must be multiplied by the thin-slab volume $A \cdot \Delta z$. Using $v_3 = \dot{u}_3$ and the normal strain definition, after a few simplifications it will become:

[redacted] (4.35)

Therefore, the heat source will be defined as:

[redacted], (4.36)

being $dv_3 = v_3(n+1) - v_3(n)$, the current flowing through the central branch of the Mason model. If dv_3 is negative, it means that there is a compression on the solid and heat is injected to the thermal network.

4.2.4 Model implementation

To model the full resonator, the different material layers are discretized in N cells. Those cells correspond to different sections of the thickness z-direction. Each of these cells are connected acoustically and also electrically for the piezoelectric layers. Finally, the different layers are connected as shown in Figure 4.7.

[redacted]

Figure 4.7: Block diagram that illustrates the circuit implementation of three layers of the BAW resonator. Each layer is constructed as a cascade of electro-thermo-mechanical cells. The electric losses are implemented as lumped resistors and their dissipated heat is coupled to the thermal domain [18].

In order to connect the acoustic/piezoelectric model with the thermal network, voltage controlled voltage sources (VCVS) and current controlled current sources (CCCS) can be used (Figure 4.8).

On Figure 4.8, T_C can be identified as the VCVS and the temperature Θ is measured at the central branch of the thermal network. Since the reference temperature specified at the thermal boundaries is zero, the temperature at the central branch can be assumed as $d\Theta$. On the other hand, the added heat $Q_{\Delta z}$ can be identified as the CCCS that is sensing the difference of particle velocities dv_3 at the central branch of the Mason model.

Figure 4.8: Piezoelectric cell showing the connection between the lumped Mason model and the thermal network.

4.3 Calculation of the temperature coefficient of the stress

In Chapter 2, a way of obtaining the temperature coefficient of stress with the stiffness tensor and the linear coefficient of thermal expansion (4.11) was described. It can be demonstrated (see Appendix B), that for a Hexagonal crystal and an Isotropic one, the previous expression can be simplified for each material to:

$$\lambda_3 = \alpha_3^E (c_{33}^{E\Theta} + 2c_{13}^{E\Theta}). \tag{4.37}$$

4.4 TED model on an AlN piezolayer

In order to see some effects that the thermal constants have on the TED model, a thin film AlN layer was simulated with our model on ADS. Both the resonant frequency and the maximum Q factor were plotted in order to evaluate its frequency shift and its Q factor degradation.

4.4.1 Effect of the room temperature and the coefficient of thermal expansion

The first test was the room temperature dependence of the model (Fig. 4.9), where it can be seen that increasing the room temperature produces a frequency shift increasing both the resonance and antiresonance frequency. Also Q factor decreases as the room temperature increases.

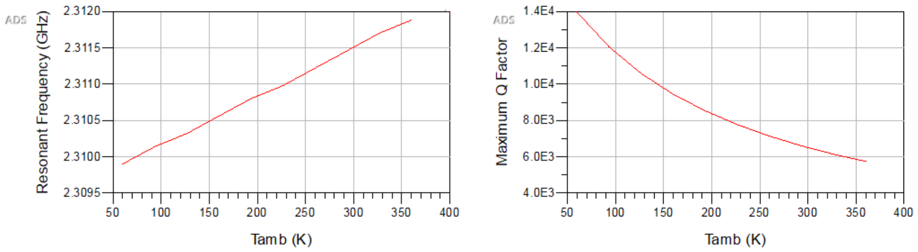

Figure 4.9: The left plot shows the resonant frequency at different ambient temperatures. The right plot shows the maximum Q factor at different ambient temperatures.

In TED the increasing of the coefficient of thermal expansion α_3, produces an increase of the resonance frequency and an accentuated degradation of the Q factor (Fig. 4.10).

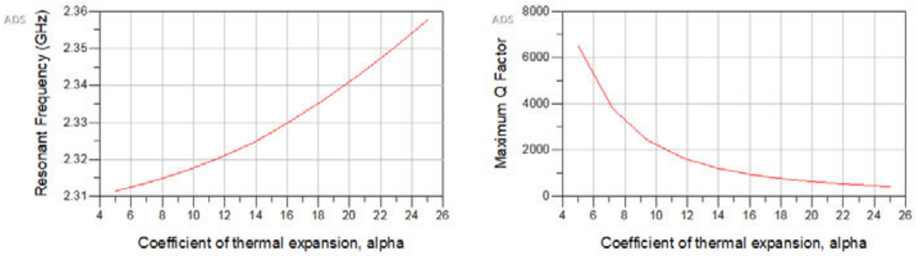

Figure 4.10: The left plot shows the resonant frequency at different coefficient of thermal expansion α_3. The right plot shows the maximum Q factor at different coefficient of thermal expansion α_3.

4.4.2 Effect of the heat capacity

A decrease of heat capacity implies that less heat is required to increase the temperature of the solid, so the thermoelastic effect that produces the damping is greater and consequently the Q factor decreases. It also reduces the stiffness constant c_{33} increasing both the resonance and antiresonance frequency. On Fig. 4.11 some plots about the behavior of an AlN single layer resonator can be seen.

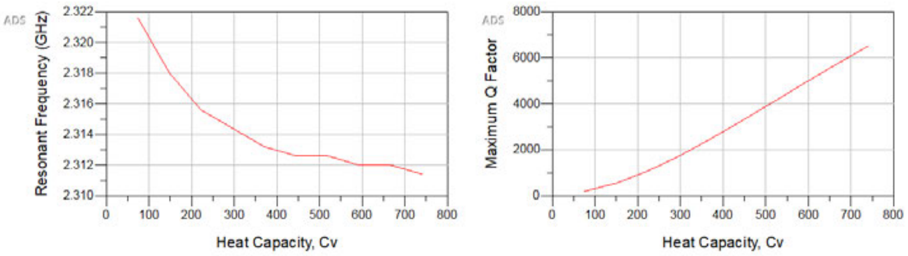

Figure 4.11: The left plot shows the resonant frequency at different heat capacities C_v. The right plot shows the maximum Q factor at different heat capacities C_v.

4.4.3 Effect of the thermal conductivity

Thermal conductivity regulates the flow of heat that propagates along the body. An increase of the thermal conductivity implies that more energy is propagating to other parts of the vibration increasing the TED. In Fig. 4.12 the impedance and the Q factor of an AlN single layer resonator are plotted at different thermal conductivity values. Note that thermal conductivity has no effect on the resonant frequency.

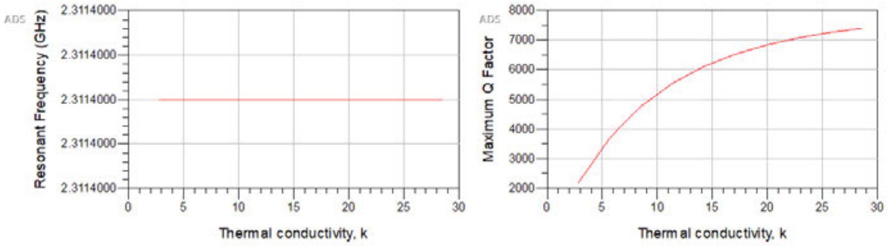

Figure 4.12: The left plot shows the resonant frequency at different thermal conductivities k. The right plot shows the maximum Q factor at different thermal conductivities k.

4.5 Temperature dependence of the BAW resonator

Static temperature variations, i.e. changes in the ambient temperature, result in changes on the materials characteristics beyond the changes described in the constitutive relations (4.12) to (4.14). These changes need to be taken into account in our model in order to correctly represent the device behavior.

The aim of that section is explaining the changes that will occur on that material properties with their phenomenological approach and present qualitatively the changes that they impose to the resonator behavior.

4.5.1 Thermal expansion and material density

The thermal expansion on the z-direction, can be expressed with the following formula concerning the change of dimension in each material layer

$$th = th_0(1 + \alpha_3 \cdot \Delta\Theta), \tag{4.38}$$

where th is the thickness of the layer.

When having thin films of material deposited in a thick substrate, the in-plane expansion is dominated by the substrate [18]. This lateral expansion of the substrate will generate a vertical dimension change according to the material Poisson ratio ν. This can be modeled by the following expression for the effective thermal expansion coefficient:

$$\alpha_{3,N,eff} = \frac{1}{1-\nu_N}(\alpha_{3,N} - \nu_N(2\alpha_{3,sub} - \alpha_{3,N})), \tag{4.39}$$

here the subscript N stands for each material layer on the resonator, and α_{sub} stands for the coefficient of thermal expansion of the silicon substrate.

In Figure 4.13, it can be seen the isolated effect of thermal expansion and also the effect considering the clamping. At first sight it cannot be seen any difference when treating the thermal expansion separately.

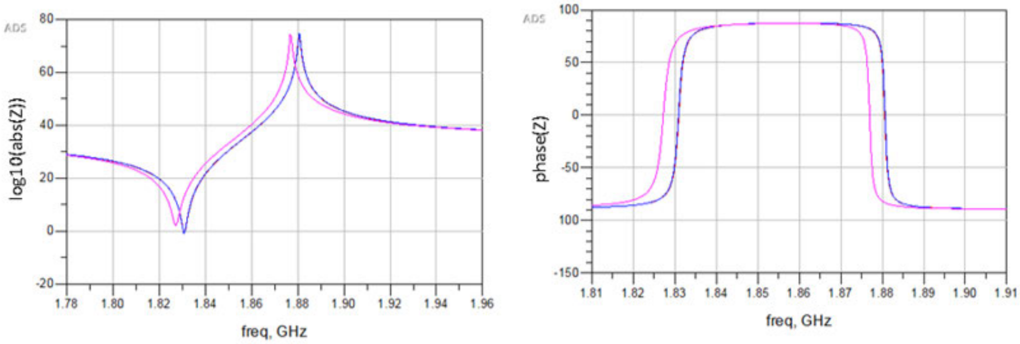

Figure 4.13: Plots of the impedance of a BAW resonator. The magenta trace corresponds to the Mason model of a resonator at room temperature. Both red and blue traces are superposed, blue is the impedance at 100 K taking into account thermal expansion, and red taking into account the substrate clamping.

From the thermal expansion phenomena, it can be clearly seen that maintaining the same mass for each layer, its mass density is going to change. If the same temperature is supposed both for the layer and the substrate, the next expression can be obtained [18]

$$\rho_{m,N} \approx \rho_{m,N,\Theta_0}(1 - (2\alpha_{sub} + \alpha_{N,eff})\Delta\Theta). \tag{4.40}$$

In Figure 4.14 the effect of the material density on the resonant frequency can be seen.

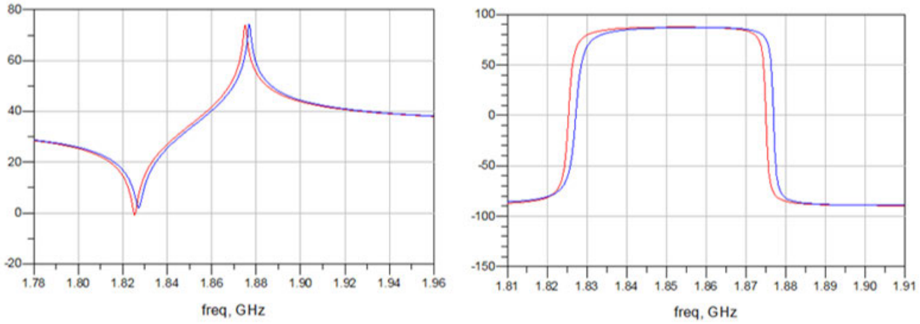

Figure 4.14: Impedance of a BAW resonator, blue trace is the impedance at room temperature, while the red one is the impedance at 100 K taking only into account the change of mass density.

4.5.2 Temperature dependence of the piezoelectric constant

The temperature dependence of the piezoelectric constant e_{33}, follows the next expression

$$e_{33} = e_{33,\Theta_0}(1 + T_e \cdot \Delta\Theta). \tag{4.41}$$

T_e corresponds to the temperature derivative of the piezoelectric constant, and it is obtained by experimental results. In Figure 4.15 the effect of the temperature decrease on the piezoelectric constant can be seen:

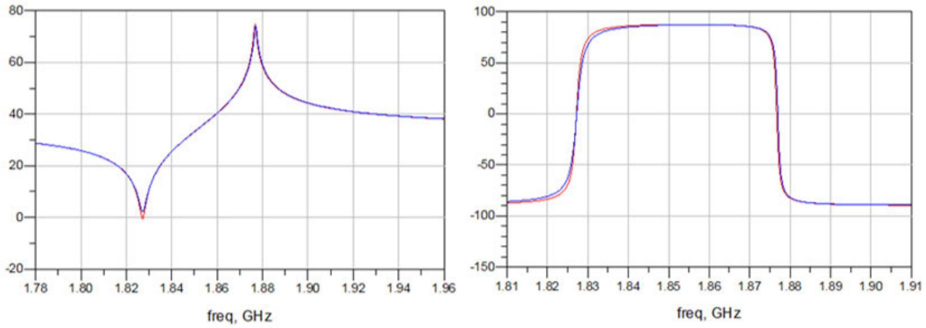

Figure 4.15: Impedance of a BAW resonator, blue trace is the impedance at room temperature, while the red one is the impedance at 100 K taking only into account the temperature derivative of the piezoelectric constant.

4.5.3 Temperature dependence of the electric permittivity

The expression for the temperature dependence of the electric permittivity ε_{33}, is the same that the one used for the piezoelectric constant

$$\varepsilon_{33} = \varepsilon_{33,\Theta_0}(1 + T_\varepsilon \cdot \Delta\Theta). \tag{4.42}$$

In this case T_ε corresponds to the temperature derivative of the electric permittivity, and it is also obtained in an experimental way. In Figure 4.16, the effect of the temperature on the electric permittivity is plotted.

4.5.4 Temperature dependence of the heat capacity

Unlike the other parameters, theoretical models exist to predict the heat capacity as a function of the temperature. These models are derived from the phonon's theory and the density of states, being rather cumbersome and difficult to deal with. For the temperature range of our measurements, the Debye's model [58] is the best suited.

$$C_v^\Theta = 9N_A k_B \left(\frac{\Theta}{\theta_D}\right)^3 \int_0^{x_D} \frac{x^4 e^x}{(e^x - 1)^2} dx, \tag{4.43}$$

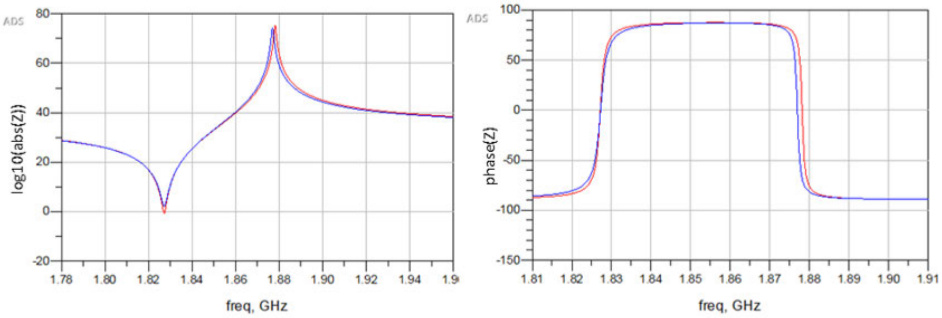

Figure 4.16: Impedance of a BAW resonator, blue trace is the impedance at room temperature, while the red one is the impedance at 100 K taking only into account the temperature derivative of the electric permittivity.

$$x_D \equiv \theta_D/\Theta. \tag{4.44}$$

where N_A is the Avogadro number, k_B the Boltzmann constant, and θ_D the Debye temperature characteristic of every material, e. g. 400 K for tungsten, 645 K for silicon. In Figure 4.17 the heat capacity is plotted as a function of the temperature normalized by the Debye temperature. It can be seen how heat capacity increases with temperature.

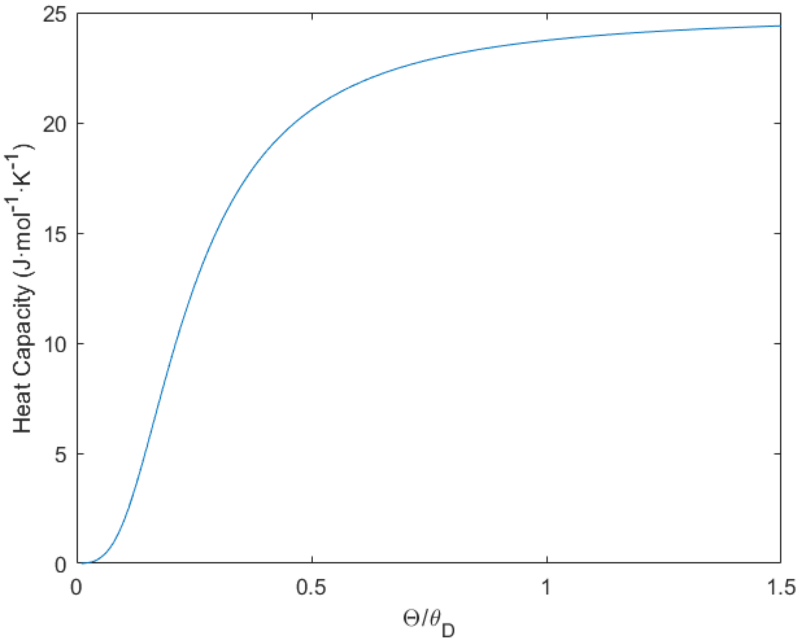

Figure 4.17: Heat capacity in function of the normalized temperature.

4.5.5 Temperature dependence of the thermal conductivity

There also exists a theoretical model for thermal conductivity that is related with the material heat capacity [58]:

$$k = \frac{1}{3} C_v^{\Theta} \cdot v \cdot \ell. \tag{4.45}$$

Where v is the average particle velocity, and ℓ the mean free path of a particle between collisions. This expression, although being pretty simple does not provide enough information about the thermal conductivity behavior with temperature. The heat capacity can be obtained from the Debye model, but the dependence of the mean free path becomes more unpredictable when supposing anharmonic interactions between phonons, and Umklapp scattering arise.

However, it can be established a relation of inverse proportionality between the mean free path and temperature, $l \propto \frac{1}{\Theta}$; the higher the temperature, the higher number of excited phonons will be in the material, increasing the probability of anharmonic interactions between phonons and decreasing the material thermal conductivity.

Looking at the measurements of different materials at [59], it can be confirmed that the mean free path imposes, and thermal conductivity decreases while temperature increases (Figure 4.18).

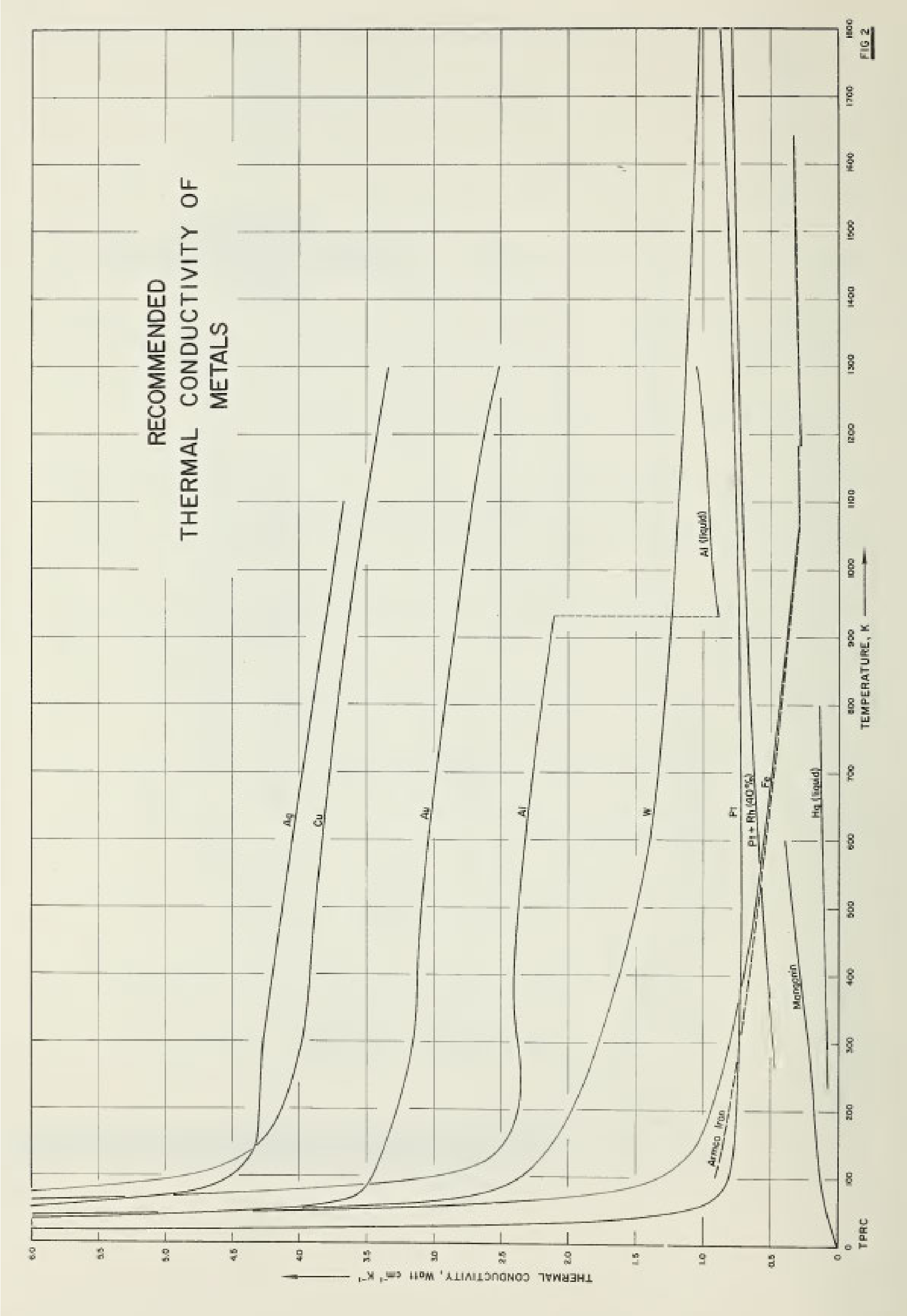

Figure 4.18: Thermal conductivity of different metals in function of temperature [59].

4.6 Temperature measurements of BAW resonators

To analyze the Q factor of the resonators, measures performed on the National Institute of Standards and Technology (NIST) were provided [60]. These measurements were performed on a set of BAW resonators provided by Qorvo, with the intention of characterizing its reflection coefficient at a wide range of temperatures.

The measurement setup consists in a cryogenic probe station, where the wafer containing the resonators was set in (Figure 4.19). A Cascade Microtech cryogenic probe was used, and the calibration substrate was designed at NIST in order to achieve the desired performance up to 20 GHz, and from the temperature range of 25K to 320K. The reflection coefficient was measured using a Vector Network Analyser (VNA).

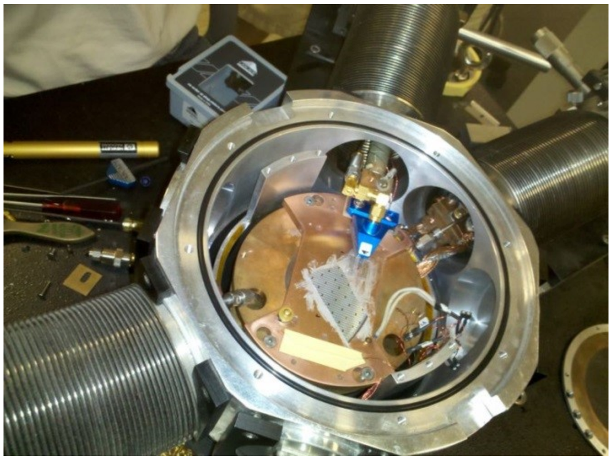

Figure 4.19: Measurement setup at NIST. It can be seen a fragment of the wafer and the Cascade Microtech probe in blue.

For this work, the measurements of two resonators where used, PBO400 and SBO400. PBO400 corresponds to the shunt resonator used in filters, with resonance frequency at 1.827 GHz, while SBO400 corresponds to the series resonator, with resonance frequency at 1.885 GHz. Both SBO400 and PBO400 are SMR resonators, they are designed for the same filter, and fabricated on the same stack.

The piezoelectric layer is made of aluminum nitride (AlN), and being the thicker layer of the resonator, it is around 1 μm of thickness. The electrodes are composed of aluminum copper (AlCu) and tungsten (W). The Bragg reflector is done interposing silicon dioxide (SiO_2) with tungsten. Other materials as silicon (Si) and silicon nitride (Si_3N_4) are used for the substrate and the passivation layer.

In order to achieve lower frequencies at the shunt resonator PBO400, the metalization of its upper electrode is increased (Figure 4.20)

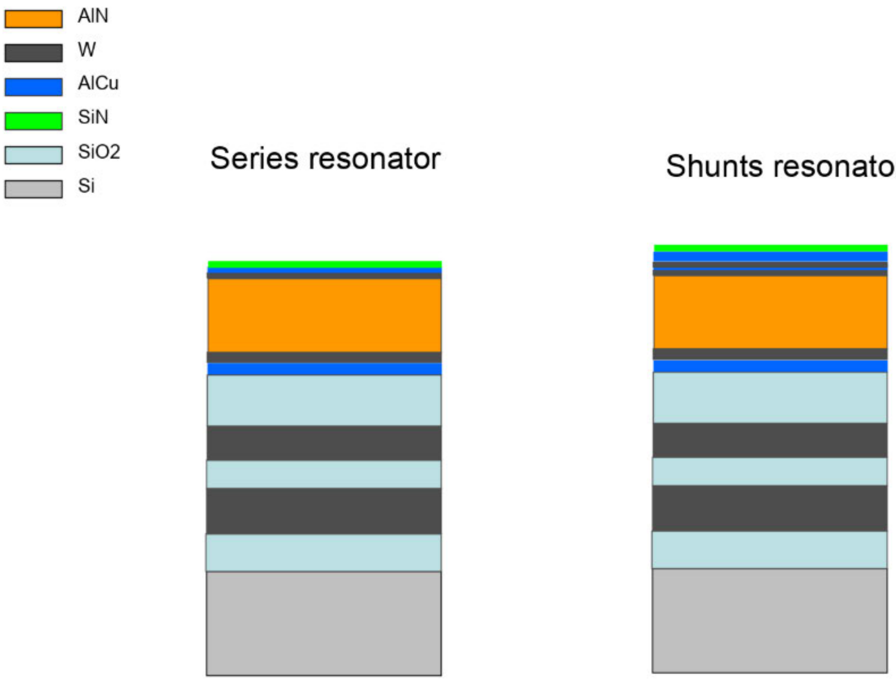

Figure 4.20: Cross section of the series resonator SBO400, and the shunt resonator PBO400. The proportions of the figures are not on scale, and only intended for illustrative purposes.

The input impedance of a resonator can be easily obtained from the reflection coefficient by the formula:

$$Z_{in} = \frac{1 + S_{11}}{1 - S_{11}} Z_0, \tag{4.46}$$

where Z_0 is the characteristic impedance set to 50Ω. We will work with impedance instead of reflection coefficient.

Two measurements at each temperature were performed to each of the resonators, one broadband measurement to obtain all the spurious resonances, and one narrowband to obtain a more detailed picture around resonance and antiresonance.

The measurements performed to the PBO400 were the following (Figure 4.24-4.26):

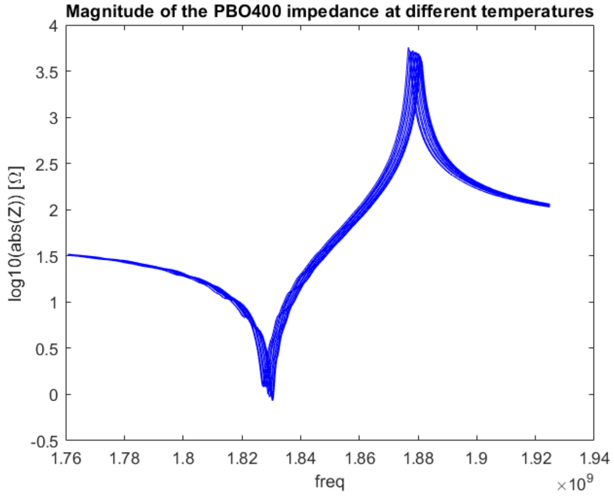

Figure 4.21: Plot of the narrowband measured magnitude of the PBO400 impedance. The different traces correspond to measurements done from 100K to 298K

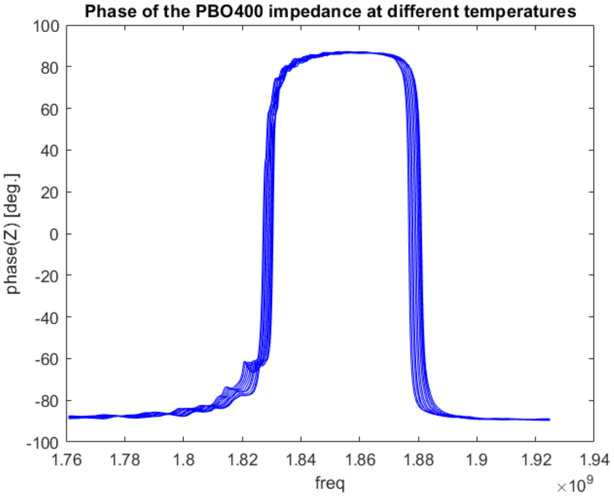

Figure 4.22: Plot of the narrowband measured phase of the PBO400 impedance. The different traces correspond to measurements done from 100K to 298K.

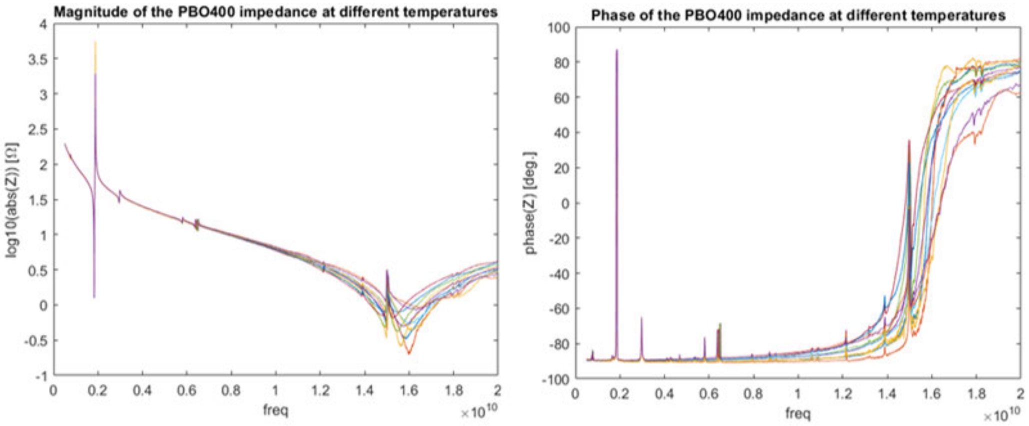

Figure 4.23: Plotted broadband measurements of the PBO400 impedance. The different traces correspond to measurements done from 100K to 298K.

Measurements of the SBO400 resonator can be seen from Figure 4.24-4.26.

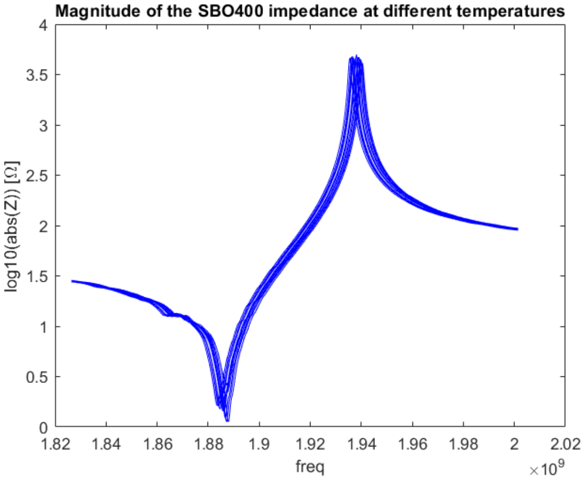

Figure 4.24: Plot of the narrowband measured magnitude of the SBO400 impedance. The different traces correspond to measurements done from 100K to 298K

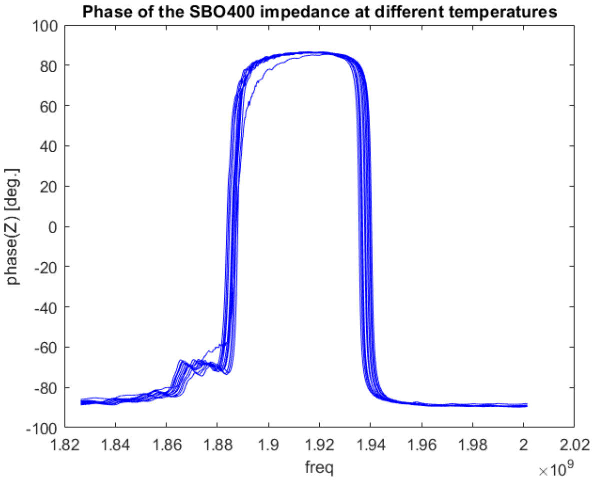

Figure 4.25: Plot of the narrowband measured phase of the SBO400 impedance. The different traces correspond to measurements done from 100K to 298K.

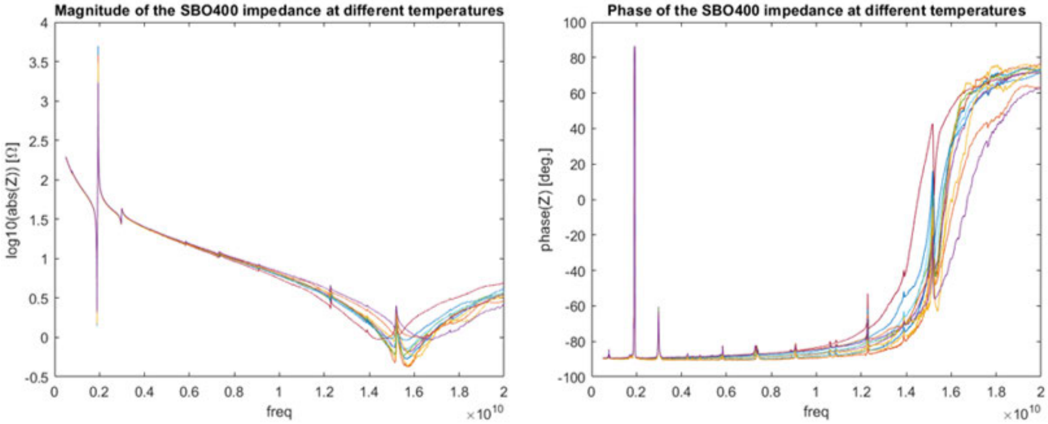

Figure 4.26: Plotted broadband measurements of the SBO400 impedance. The different traces correspond to measurements done from 100K to 298K.

In this measurements, it can be seen how as temperature decreases thermal expansion produces a thickness decrease on each layer of the resonator, thus resulting in a frequency increase of both resonance and antiresonance frequencies.

It the broadband measurements, it can be seen a huge phase shift of the impedance around 15 GHz. This is mainly due to the electric length of the resonator's pads and need to be also considered in our model. It can be easily modeled by adding an ideal transmission line at the electric terminals of the Mason model, the electric length of that line will be adjusted to match the measurements.

The Q factor of the measurements can be obtained from the (2.34), but using the reflection coefficient of the measurements directly, results in a very noisy Q factor. To solve this, a Mason model was fitted to the measurements and its simulated reflection coefficient was used to obtain the Q values at resonance at antiresonance (Figure 4.27).

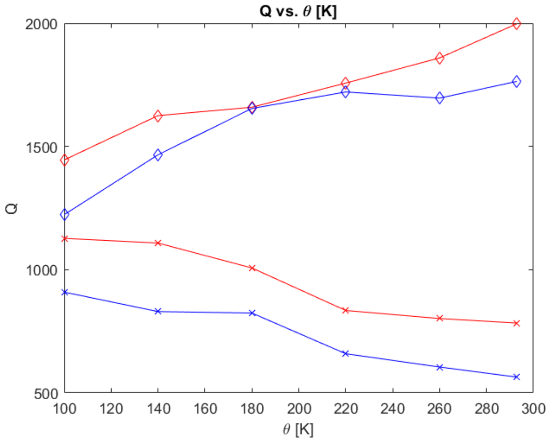

Figure 4.27

The increase of Q factor at resonance when the temperature diminishes could be explained with the electric conductivity increase of both the electrodes and the pads. But there was no clue about what phenomena could be degrading the Q factor at the antiresonance, before considering the TED effects.

4.6.1 Q factor degradation due to Bragg reflector

The first hypothesis managed was that the Q factor degradation was induced by the ineffectiveness of the Bragg reflector caused by the thermal expansion coefficient of the materials.

To evaluate this hypothesis, the measurements of the PBO400 were selected. The Q factor was evaluated using the Mason model implemented on Advanced Design System (ADS), taking into account the material thermal properties explained in Section 4.5 (Figure 4.28). Since the TED model is not being used for this hypothesis, the temperature dependence for the stiffness constant is also added:

$$c_{33}^{E} = c_{33,\Theta_0}^{E}(1 + T_c \Delta\Theta), \tag{4.47}$$

in this case, T_c is the temperature derivative of the stiffness constant.

At ambient temperature (298 K), all the physical parameters were tuned to fit the measurement and the initial Q factor was adjusted with the electrode resistance R_s,

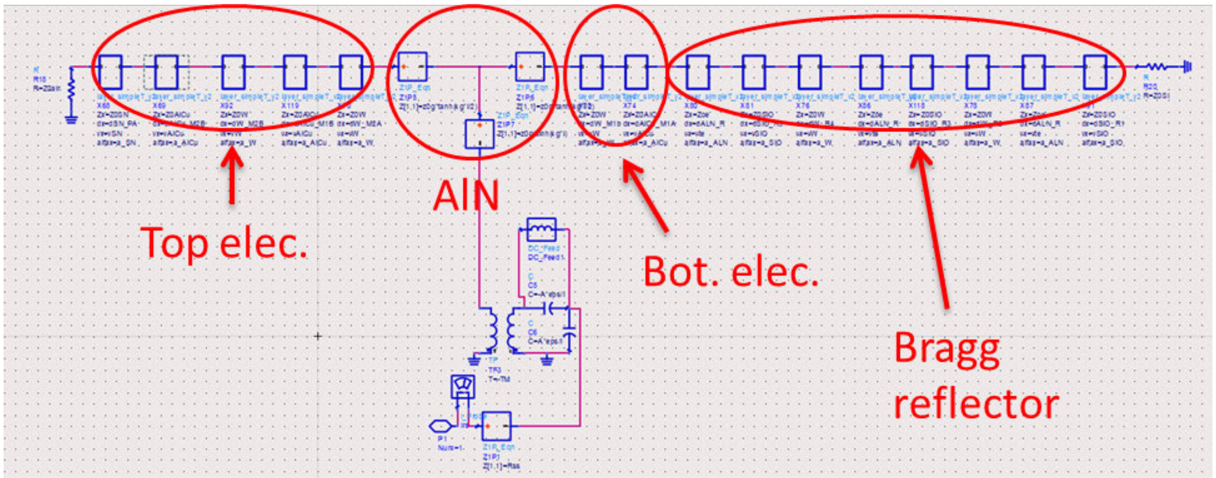

Figure 4.28: Mason model for the PBO400 resonator implemented on ADS.

and the viscosity of each layers. These adjustments where realized at the broadband measurements taking into account the spurious resonances.

To obtain the Q factor at the other temperatures, viscosity was maintained constant while the other material parameters were adjusted in function of its dependence with temperature (view Table 4.1). The R_s is expected to increase with temperature and was selected to fit the Q at the resonance.

Material	$T_c(10^{-6}/K)$	$T_\varepsilon(10^{-6}/K)$	$T_e(10^{-6}/K)$
AlCu	-300	-	-
AlN	-60	150	10
Si_3N_4	-24.4	-	-
Si	-75	-	-
SiO_2	239	-	-
W	-91	-	-

Table 4.1: Temperature derivatives for each material [18].

Comparing both measured Q values and simulated ones (Figure 4.29), it can be clearly seen that the temperature behavior of the resonator itself cannot be the cause for the Q factor degradation on antiresonance.

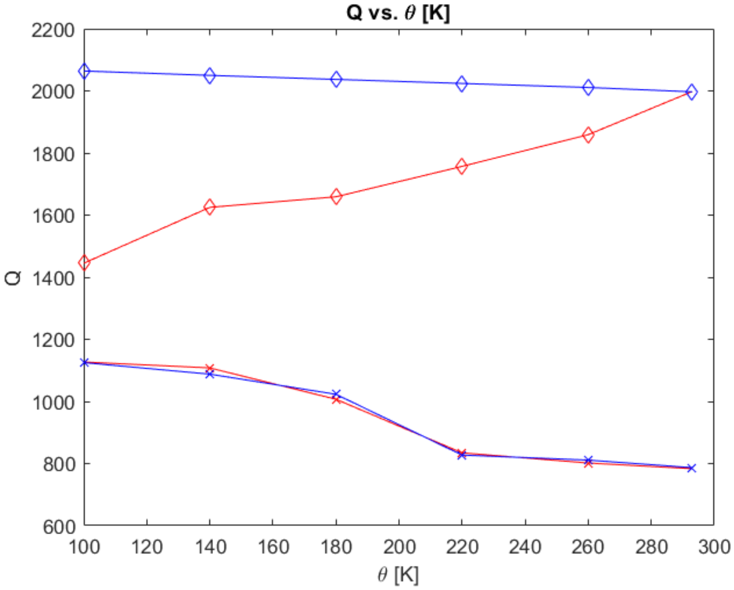

Figure 4.29: Q factor at different temperatures of the PBO400 resonator. Red traces correspond to the measurements, while blue traces to the simulations. Crosses stand for resonances and diamonds for antiresonances.

More simulations were realized regarding the effect of all of these phenomena separately. Each of the parameters was tuned to match the frequency variation at 100 K (Table 4.2).

Effect	Value	Q resonance	Q antiresonance
Thermal expansion (α)	x2	1096	1998
Thermal expansion w. substrate clamping (α_ν)	x4	1086	1977
Temperature derivative c	x0.85	1119	2054
Material density (ρ_m)	x0.993	1098	1996

Table 4.2: Results of the simulations.

In the previous table, it can be seen that although some parameters were slightly tuned to match the frequency drift, e.g. material density. None separately, or altogether can explain the Q factor degradation.

4.6.2 Q factor degradation due to thermoelastic damping (TED)

Once it has been discarded that the Q degradation is due to the thermal effects in the Bragg reflector, a new hypothesis is proposed: The degradation of the Q factor at the antiresonance, is due to thermoelastic damping.

Looking at the heat equation (4.18), and knowing the temperature dependence of both heat capacity and thermal conductivity, it can be seen that when temperature decreases the heat propagation increases. This way the energy injected to the thermal network will be higher and the dynamic temperature of the solid will increase.

For these simulations, the thermoelastic damping model was also implemented on ADS (Figure 4.30) for both the PBO400 resonator and the SBO400 resonator. In order to isolate the TED from other damping sources, viscosity was set to zero and no viscoelastic losses were simulated.

[redacted]

Figure 4.30: Implementation of the TED model on ADS.

The first resonator simulated was the PBO400 resonator; it was first adjusted at room temperature (298 K). Due to setting the viscoelastic damping to zero, the initial heat capacity need to be 35 % of the value at room temperature and the thermal conductivity 1.85 times higher to fit the Q factor at room temperature. Later it was adjusted taking into account the change of the materials properties. Heat capacity and thermal conductivity were adjusted to fit the frequencies and the Q factor at different temperatures.

In Figure 4.31 can be seen that the Q factor can be approximated by our model, by diminishing the heat capacity and increasing the thermal conductivity when going down in temperature. On Figure 4.32 the comparison of the measured impedance and the simulated can be seen.

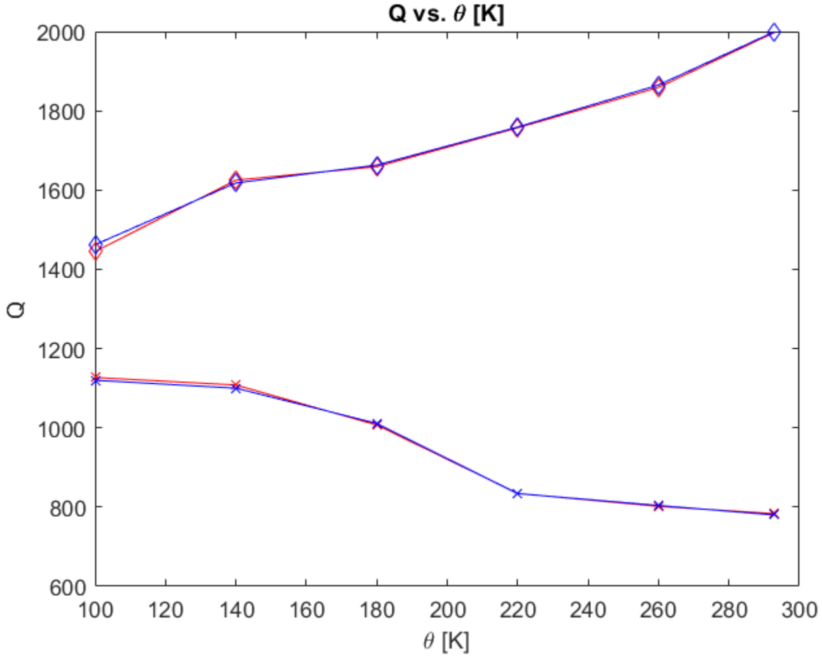

Figure 4.31: Q factor at different temperatures of the PBO400 resonator. Red traces correspond to the measurements, while blue traces to the TED simulations. Crosses stand for resonances and diamonds for antiresonances.

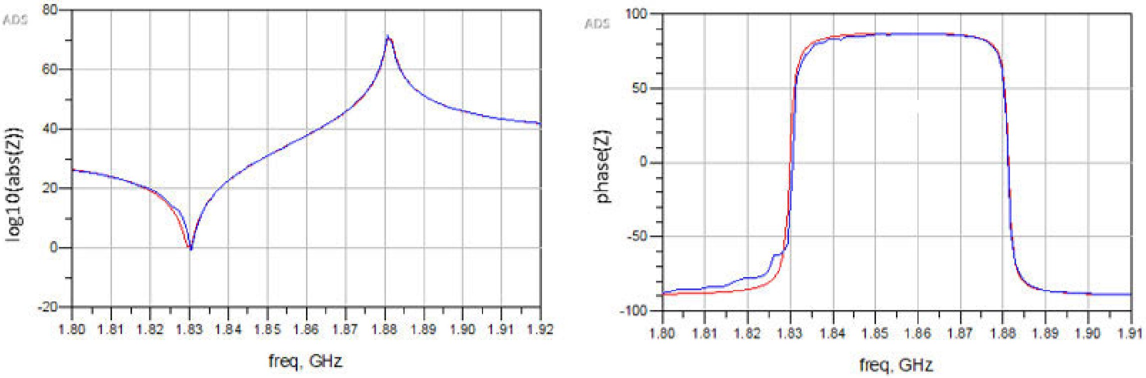

Figure 4.32: Measurements (red) versus simulated TED model (blue) plots of the magnitude (right) and the phase (blue) of the impedance at 100 K.

The model is adjusted at each temperature, slopes of the temperature behavior were obtained for both the heat capacity and thermal conductivity. In order to acquire the temperature derivatives, a linear regression was performed with Matlab (Figure 4.33).

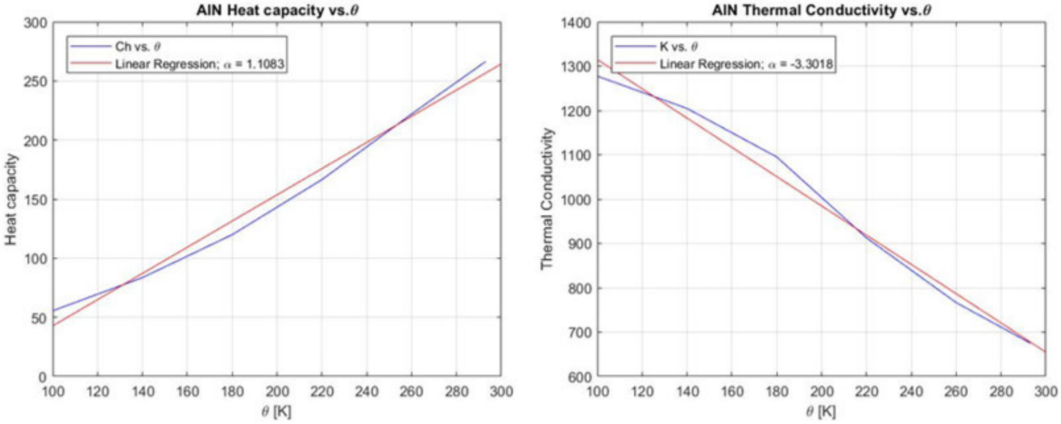

Figure 4.33: Adjustments of the heat capacity (right) and the thermal conductivity (left) of AlN layer in PBO400 on blue, in red it is plotted its linear regression.

Once done for the PBO400 resonator, the same values of heat capacity and thermal conductivity were tried on the SBO400. Since they are fabricated on the same wafer, little variation of the materials characteristics was expected.

However in order to fit the measurements and obtain the measurement Q factors (Figure 4.34), the heat capacity and the thermal conductivity were slightly adjusted.

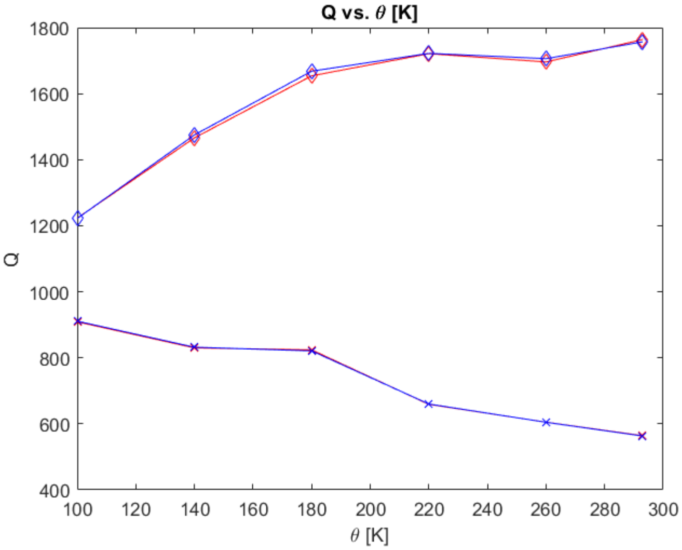

Figure 4.34: Q factor at different temperatures of the SBO400 resonator. Red traces correspond to the measurements, while blue traces to the TED simulations. Crosses stand for resonances and diamonds for antiresonances.

On Table 4.3 a comparison of the heat capacity and thermal conductivity slopes at both PBO400 and SBO400 is shown.

Material	$\alpha_{C_v}(K^{-1})$		$\alpha_k(K^{-1})$	
	PBO400	SBO400	PBO400	SBO400
AlCu	1.43	1.37	-1.9	-1.25
AlN	1.1	0.99	-3.3	-2.17
Si_3N_4	0.92	0.84	-0.22	-0.14
Si	0.933	0.87	-1.44	-0.95
SiO_2	0.99	0.91	-0.012	-0.008
W	0.2	0.197	-1.57	-1

Table 4.3: Slopes of the linear regressions of heat capacity and thermal conductivity.

Comparing both results, it can be observed that the heat capacity variation from each resonator is slightly different, but the thermal conductivity has a more notable difference.

The variation of the heat capacity C_v and the thermal conductivity k with temperature, are obtained through the fitting of the model. The intrinsic variation of this parameters is not found in literature for thin films, so further experiments are necessary to validate this behavior.

Also, having only analyzed the thermoelastic damping, and having not taken into account viscoelasticity and other damping phenomena that exists in acoustic waves, it is difficult at this point to confirm the thermoelastic damping is the unique cause of the Q factor degradation at antiresonance at low temperatures. Although, it seems clear than thermoelastic damping can be identified as a possible contributor to this phenomenon.

4.7 TED on the outband spurious resonances

In order to validate the Mason based TED model, more experiments were performed. The SMR-BAW devices usually show highly coupled, out of band spurious resonances (See Figure 4.35). These spurious are generated in the Bragg reflector and are located at frequencies above resonance.

Looking at the standing wave patterns of some of these resonances, one can see that the acoustic energy is confined in the different layers of the reflector. The loss mechanism of this resonances is usually attributed to the viscoelastic losses (See

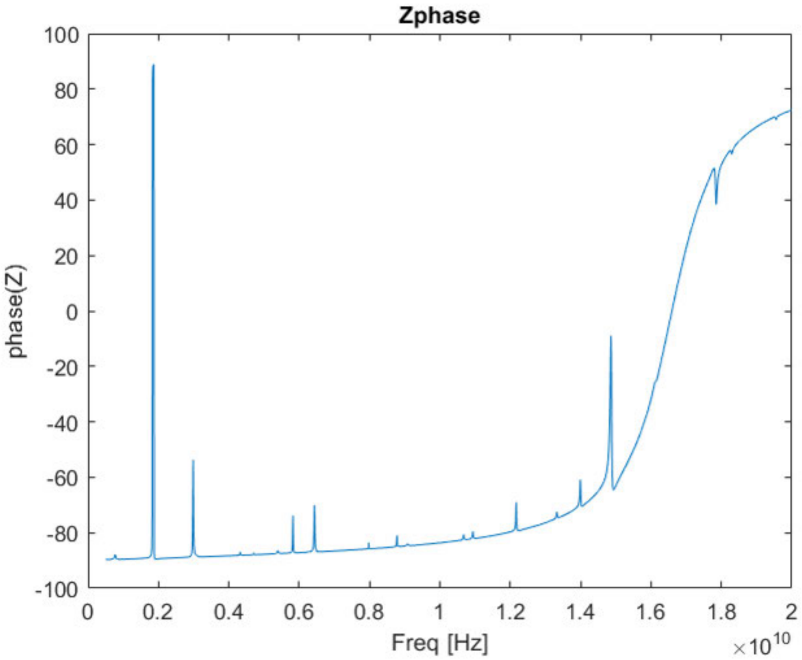

Figure 4.35: Phase of the impedance of a BAW resonator. The spurious resonances can be seen as spikes above the fundamental resonance at about 1.8 GHz

Section 2.4) of the different materials comprising the Bragg reflector. Nevertheless, the viscoelasticity of the materials, although offering a good estimation of losses near the resonant frequency, fails to explain the loss behavior at those higher frequency spurious.

The Q factor of a BAW resonator can be obtained from (2.34). Although, the formula presents some inconsistencies at some of these spurious [62]. For the sake of this analysis a fitting of the Q circle to a series RLC model was used (Figure 4.36) [63].

[redacted] (4.48)

here, $\Delta\omega$ is the resonator -3 dB bandwidth, and the subscript 0 refers to the resonant frequency. A shunt resistor can be added the same way as done in [24], to take into account the departure from a circular impedance locus.

[redacted]. (4.49)

Finally, a phase change ($e^{-j\beta}$) was also added before obtaining the fitted Q circle:

[redacted] (4.50)

[redacted]

Figure 4.36: Circuit model of a RLC resonator.

The Q values were extracted directly from the fitting (Figure 4.37), although the extracted Q values are not the exact ones. Nevertheless, the application of the same procedure for each resonance gives the method consistency.

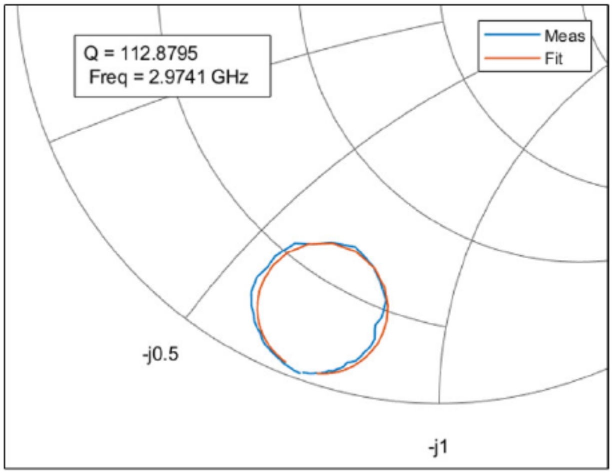

Figure 4.37: Fitting of the Q circle for a spurious resonance. The extracted Q values can be seen on the inset.

In order to detect the source of the damping, two main sources were taken into account separately, viscous damping, and thermoelastic damping. The viscoelastic effect was taken into account with the Mason model. the viscoelastic constant for each material layer was adjusted to fit the Q factor at the fundamental frequency.

On the outband spurious resonances, their viscoelastic damping will depend on:

- The attenuation coefficient (α), defined on (2.32). It scales with ω^2 and depends on material parameters, the phase velocity (v_p), and the viscosity (η).

- For each spurious resonance, the predominant α will correspond to the ones of the resonator's layers where the displacement is maximum.

On the other hand, thermoelastic damping also increases with frequency. In Section 4.1.2 was seen that when the adiabatic assumption of the solid is broken, heat flow to other material regions. Assuming a plane longitudinal wave, compressed areas become warmer while extended cooler (Figure 4.2).

The heat generated at compressed regions will flow to the cooler expanded region, this will extract energy from the acoustic wave generating losses. At high frequencies, the thermal path for a longitudinal wave its reduced. This causes more heat propagation to cooler areas and increases the thermoelastic damping. For the thermoelastic damping, the resonator layer where the spurious is generated also plays an important role. Since the phase velocity is different for each material, the thermal path can be reduced for some resonances in particular.

4.7.1 Fitting of the spurious resonances

The spurious resonances of three different resonators were fitted to the RLC model in order to obtain its Q factor. The results were compared with the TED Mason model and the mason model with viscoelastic losses dependent of the material.

4.7.1.1 PBO400 Analysis

Several spurious resonances are selected from the PBO400 (Figure 4.38), ranging from the 3 GHz to 15 GHz.

The thermal conductivity k of each material, and the viscoelasticity η of SiO_2 and AlN, are adjusted for the spurious resonance of the highest frequency independently. These two materials are the ones fitted since they are the main responsible of viscoelastic losses at the selected resonances. The Q factors are also obtained from the Mason model with the viscoelasticities of each material provided by Qorvo.

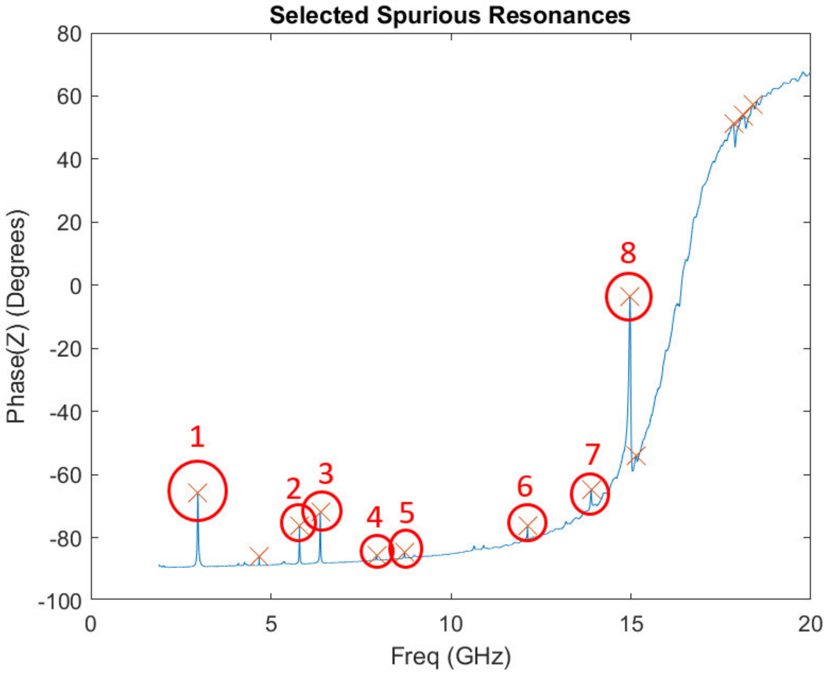

Figure 4.38: Phase of the impedance of the PBO400 resonator at high frequencies.

Resonance	Q Meas	Q TED	Q η AlN $= 0.023$	Q η $SiO_2 = 0.011$	Q η Qorvo
Fund.	2101	6719	2809	4271	2106
1	112.5	185.9	221.6	168.8	174.2
2	360.3	481	767.36	287.3	285
3	330	309.6	1226.6	1958	360.6
4	610.1	1103	2717.3	375.8	408.3
5	738.7	638.9	484.9	1222.27	643.17
6	842.3	664.4	371.4	1281.5	554.9
7	551.9	715	1980.3	280	279.8
8	463.5	470.2	483.7	462.8	281.7

Table 4.4: Fitting of the spurious resonances of the PBO400 for different loss mechanisms.

The previous results show that the TED gives better explanation of the loss mechanisms at higher frequencies, meanwhile viscoelastic losses adjusted are not able to explain the different Q factors of these resonances.

Looking at resonances number 7 and for in Table 4.4, we can observe that TED by its own it is not able to explain all this losses. For that reason, additional viscoelastic losses are added to the SiO_2 layer (Table 4.5)

Resonance	Q Meas	Q TED + η $SiO_2 = 0.0035$
Fund.	2101	2809
1	112.5	162.5
2	360.3	345.5
3	330	297.4
4	610.1	505.8
5	738.7	595.8
6	842.3	587.7
7	551.9	393.4
8	463.5	378.3

Table 4.5: Fitting of the spurious resonances of the PBO400 with TED and η SiO_2.

4.7.1.2 SBO400 Analysis

The same procedure was repeated for the SBO400 resonator with the values obtained for the PBO400. This time, nine spurious resonances are analyzed (Figure 4.39).

The Q factors of each resonance can be seen on Table 4.6. At the measurement of the first spurious resonance the Q factor appears in red, at resonances 6 and 7 no fitting of the Q circle has been obtained. For the first case, the obtained Q factor is putted in doubt since the measured Q circle seems to have other resonances and the fitting procedure is not able to obtain the correct Q factor (Figure 4.40). For the other cases, the Q circle was to small for obtaining a proper fitting, meaning that the Q factor at that resonances is too low.

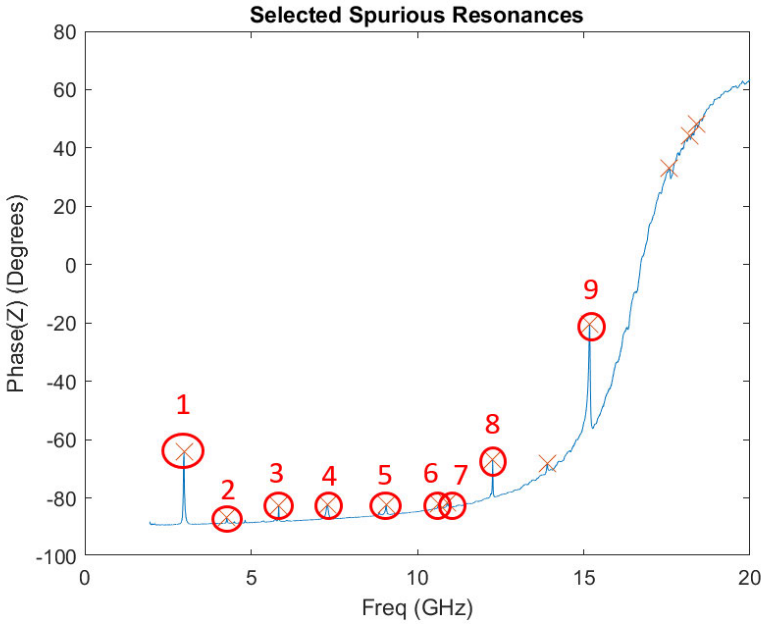

Figure 4.39: Phase of the impedance of the SBO400 resonator at high frequencies.

Resonance	Q Meas	Q TED	Q η AlN $= 0.023$	Q η SiO$_2$ $= 0.011$	Q η Qorvo
Fund.	1683	6326	4548	4045	2079
1	97.8	171	200.7	156.6	161.3
2	266	257.3	284.3	229.5	222.3
3	374.4	572.9	793.2	308.3	290.5
4	116.1	323	1563.4	5333.8	368.4
5	305.2	312.2	360.3	300.5	270
6	386	489.2	714.6	No meas.	No meas.
7	357.4	623.8	963.2	No meas.	319.6
8	812.7	678.1	356.4	1133.3	554.4
9	386.3	546.3	460.2	476.1	303.4

Table 4.6: Fitting of the spurious resonances of the SBO400 for different loss mechanisms.

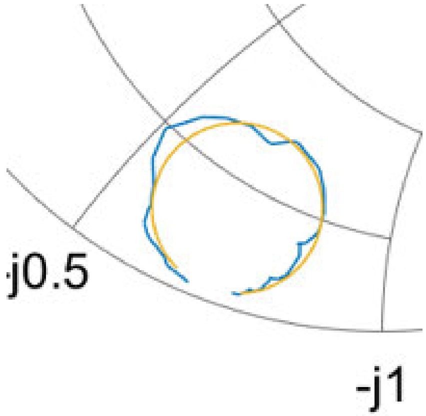

Figure 4.40: Fitting of the Q circle. The measurement can be seen in blue, the RLC fitting is shown in yellow.

As done with the PBO400, the viscoelastic losses of the SiO_2 are added to the TED (Table 4.7)

Resonance	Q Meas	Q TED + η $SiO_2 = 0.0035$
Fund.	1683	2360
1	97.8	155.9
2	266	248.8
3	374.4	364.6
4	116.1	310.5
5	305.2	259.9
6	386	314.4
7	357.4	319.6
8	812.7	551.1
9	386.3	410.8

Table 4.7: Fitting of the spurious resonances of the SBO400 with TED and η SiO_2.

4.7.1.3 B30 Resonator Analysis

Another resonator with a totally different stack was also analyzed, in this case a resonator for the B30 band, operating at 2.3 GHz. For this resonator eight spurious resonances were analyzed (Figure 4.41).

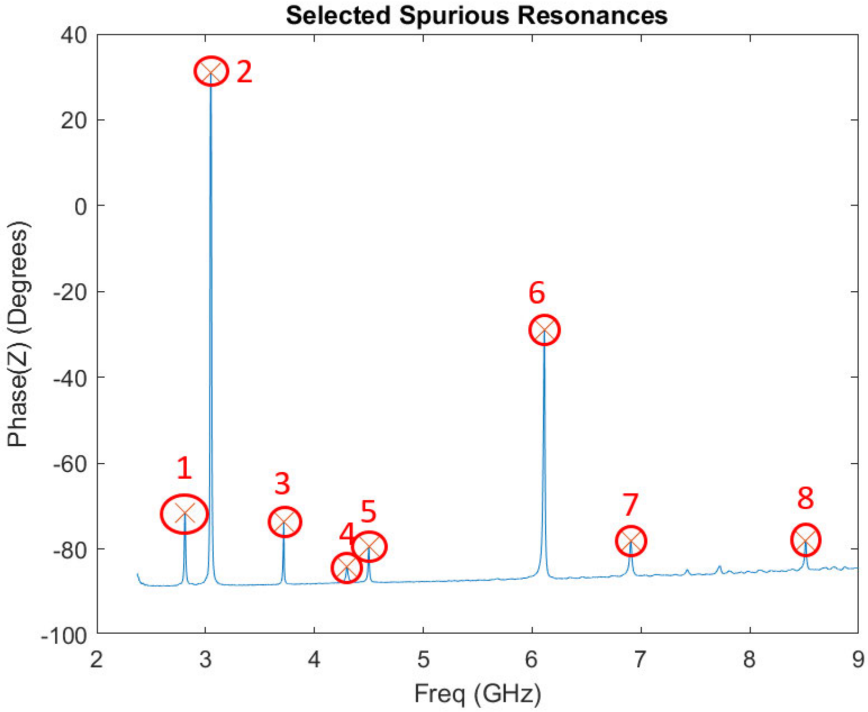

Figure 4.41: Phase of the impedance of the B30 resonator at high frequencies.

This resonator shows higher Q factor spurious than the PBO400 and SBO400. Using the same material parameters than the ones used on previous analysis, will give validation of the independence of the model to the device's stack. The Q factors of the spurious resonances in the B30 resonator appear on Table 4.8.

Resonance	Q Meas	Q TED	Q η AlN $= 0.023$	Q η $SiO_2 = 0.011$	Q η Qorvo
Fund.	1440	7534	2834	1212	1210
1	222	352	344	202	237
2	439	1154	2051	435	545
3	490	720	1071	481	445
4	218	281	281	169	180
5	373	507	597	230	277
6	502	671	1620	788	397
7	327	515	778	236	273
8	534	1005	2041	201	234

Table 4.8: Fitting of the spurious resonances of the B30 resonator for different loss mechanisms.

For this case the viscoelastic losses of SiO_2 were added as well to the TED model (Table 4.9).

Resonance	Q Meas	Q TED + η $SiO_2 = 0.0035$
Fund.	1440	2731
1	222	282
2	439	670
3	490	563
4	218	220
5	373	358
6	502	544
7	327	346
8	534	365

Table 4.9: Fitting of the spurious resonances of the B30 resonator with TED and η SiO_2.

4.8 Conclusions

Through this chapter a comprehensive explanation of thermoelastic damping in BAW resonators is given to the reader. The thermo-electro-mechanical constitutive relations are derived from the electric Gibbs potential. These constitutive relations are the fundamental blocks for deriving an equivalent model of this phenomenon.

Applying the thermo-electro-mechanical constitutive relations to the Mason model, we are able to reproduce the thermoelastic damping in a BAW resonator. On this Mason model, an RC transmission line is used to model the heat propagation across the resonator's stack. This RC transmission line is used to model the thermal domain of the resonator, and it becomes coupled to the Mason model by the constitutive relations. To validate this circuital model different analysis were performed.

The first analysis, performed only on the fundamental resonance at cryogenic temperatures, showed a good agreement with the trend of the experimental data. Although, it was not sufficient to validate the model.

The experiments performed on the spurious resonances give additional validation to the thermoelastic model. Since for these resonances the acoustic energy is confined in different layers of the resonator, we expect that the losses will occur at the correspondent layer. The TED model shows good agreement with the experimental data for the majority of these spurious resonances.

The main drawback for the application of this model is the determination of the correct thermal material characteristics for thin film materials. In the literature thermal conductivities and heat capacities can be found for bulk materials, although they are not easily found for thin films. The determination of these parameters supposes a challenge to overcome in future work.

Chapter 5

Conclusions and Future Work

BAW technology has become the key for achieving RF filters at high frequencies, necessary for the next generations of mobile networks.This thesis is centered in modeling the effects that degenerate the Q factor, the ones involving spurious lateral resonances, and the loss mechanisms due to thermal effects.

In Chapter 2, the basic physics of a BAW resonator are explained. There, the piezoelectric effect is explained and how the electromechanical transduction plays a role in an electroacoustic resonator. The impedance of a simple BAW resonator constituted of a single piezolayer is defined. The Q factor of a resonator is introduced, relating it to the losses of the device. The two main circuital models used for BAW resonators are presented. Those are the Butterworth van Dyke model, commonly used for filter design, and the Mason model which gives a more accurate physics of the BAW resonator.

Chapter 3 deals with the Lamb wave originated at the piezolayer. The physical derivation of the Lamb wave modes is given to the reader. Departing from that, an explanation of the unwanted effects on a real device presented (spurious modes) as well as the used methods for its suppression, the Border Ring (BR) and the apodization. The BvD model is expanded for the modeling of these spurious resonances. Once the theoretical basis is established, new models for the spurious modes generated by the Lamb waves. It first introduces a Mason based model with a dispersive transmission line to take into account the lateral dimension of the resonator.

The Mason model with the lateral transmission line is then used to predict the spurious modes that appear on SMR resonators with a BR. Showing that they are generated by a dispersive mode other than the TE_1. This explains the different spurious appearing due to the BR. The ability to accurately predict these resonances opens new doors for optimizing the resonator design in order to minimize their impact on the filter response.

The effect of the spurious resonances on the H2 emissions of a BAW resonator are treated in the following section. The Mason based model with the dispersive line is expanded with the nonlinear constitutive relations for piezoelectricity. The results for two different SMR resonators are shown. The ripple in the H2 response can become a problem on filters. The common practice to reduce the level of H2 emissions is doubling the resonators in counterphase. A mismatch on the spurious resonances will become a bad cancellation of H2 in the filter response. For this reason a good modeling of this effect is needed.

On the next section the Transmission Line Matrix (TLM) method is presented for modeling 2D and 3D acoustic cavities. The novelty of this method is his capability to model any electrode in-plane geometry and the BR as well. It shows a significant speed up than other methods usually used such as FEM. This speed up becomes really important when designing a filter. The selection of the electrode shape plays an important role in suppressing the spurious resonances. The correct suppression of these resonances also plays a role in the Q factor ob the resonator.

The lower computational time of TLM compared to FEM enables the use of optimization algorithms for the electrode shape at the filter level design. Giving the filter designer more tools to achieve the targeted performance.

The last chapter, Chapter 4, is focused in the thermal effects of the resonator and the role they play in the Q factor degradation. The physics underlying the interaction between the thermal, the electrical, and the mechanical domain are presented to the reader. From these physics the thermoelastic damping effect is derived for an acoustic plane wave.

Departing from the thermo-electro-mechanical constitutive relations, a Mason based model for thermoelastic damping (TED) is proposed. The model is firstly tested by cryogenic measurements of BAW resonators. Here the model is putted into comparison with a Mason with viscoelastic losses. This comparison, is performed to see if the abnormal behavior of the Q factor at the antiresonant frequency with temperature can be explained by TED. The model is able to explain the degradation of the Q factor of the antiresonant frequency at cryogenic temperature, but the determination of the material parameters needs further investigation.

In order to provide more experimental evidence for the proposed model, the high frequency outband spurious resonances are analyzed. These resonances operating at a higher frequency are more prone to experience TED. This is mainly due to the shorten of the wavelength's thermal path, since it is shorter that the fundamental frequency one.

These spurious modes are fitted to a RLC circuit to obtain its Q factor. Comparisons between measurements, viscoelastic damping, and TED are provided, showing a good agreement between the experimental data and TED.

The models derived in this thesis open the possibility for a faster resonator design, and also open the possibility of further resonator optimization. Nevertheless more work is needed in order to expand the capabilities of these models.

5.1 Future work

The main limitation of the Quasi-3D TLM model is the characterization of the stack acoustic characteristic impedance Z_0. The analytical expression derived in [30] is only valid for isotropic electrode-less resonators, that is the reason why it is scaled for SMRs.

The characteristic impedance depends of the standing wave of the particle velocity in the thickness direction v_3 and the force F_3. These standing wave patterns will change depending of the stack layers configuration for the TE_1 mode. Deriving an analytical expression for these field magnitudes in an SMR will help having a better initial approach of the characteristic impedance.

Also, the Quasi-3D TLM model may be modified to reflect the nonlinear behavior of all the lateral spurious modes, as done in Section 3.4 for the Mason model with lateral transmission lines. To achieve it, some sources adding the nonlinear terms will need to be introduced in the model.

On the other hand, more validation of the TED Mason model needs to be performed. The model has a great correlation with the losses happening at the different experiments, but the material parameters need to be adjusted in order to fit the measurement responses.

A determination of the thermal material parameters of thin films need to be performed. In order to do so, material characterization needs to be performed outside the resonator level. Also, the Fourier heat propagation equation needs to be paid more attention on the TED Mason model. Since we are working with thin films, the approximation of thermal waves having infinite propagation velocity may not be valid.

Chapter 6

List of Author's Contributions

6.1 Journals & Symposia Publications

- C. Udaondo, C. Collado, J. Mateu and R. Aigner, "Analysis of Border Ring Modes on SMR-BAW Resonators," *2019 IEEE International Ultrasonics Symposium (IUS)*, Glasgow, UK, 2019, pp. 1703-1706, doi: 10.1109/ULTSYM.2019.8925601.
- C. Udaondo, C. Collado, J. Mateu and D. Garcia-Pastor, "An Equivalent Model for Lateral Modes on the H2 Response of Bulk Acoustic Wave Resonators," *2020 IEEE International Ultrasonics Symposium (IUS)*, Las Vegas, NV, USA, 2020, pp. 1-4, doi: 10.1109/IUS46767.2020.9251801.
- C. Udaondo et al., "Out of Band Improved Performance Into a Measured 5G N77 Band Transversal Filter," *2021 IEEE International Ultrasonics Symposium (IUS)*, Xi'an, China, 2021, pp. 1-4, doi: 10.1109/IUS52206.2021.9593322.
- C. Udaondo, C. Collado and J. Mateu, "Fast modeling of lateral modes in BAW resonators with arbitrary in-plane geometry," *2022 IEEE International Ultrasonics Symposium (IUS)*, 2022, pp. 1-4, doi: 10.1109/IUS54386.2022.9957924.
- C. Udaondo, C. Collado and J. Mateu, "Fast Analysis of Border Ring Suppression on BAW Resonators," *2023 IEEE International Ultrasonics Symposium (IUS)*, Montreal, QC, Canada, 2023, pp. 1-4, doi: 10.1109/IUS51837.2023.10306477.
- C. Udaondo, C. Collado, and J. Mateu, “Quasi-3D Model for Lateral Resonances on Homogeneous BAW Resonators,” *Micromachines*, vol. 14, no. 11, p. 1980, Oct. 2023, doi: 10.3390/mi14111980.

6.2 Student works related to the research activities

- C. Udaondo, "Analysis and modeling of lateral modes in electroacoustic resonators," *Bachelor's Degree Thesis*, Universitat Politècnica de Catalunya, 2017.
- C. Udaondo, "Thermoelastic damping losses in BAW resonators," *Master's Degree Thesis*, Universitat Politècnica de Catalunya, 2018.

Bibliography

[1] R. Ruby, "A Snapshot in Time: The Future in Filters for Cell Phones," *IEEE Microwave Magazine*, Vol.16, no. 7, pp. 46-59, 2015.

[2] J. Brown, "RF/Microwave filters fit surface-mount needs," *Microwaves and RF*, June 2010.

[3] K. -y. Hashimoto, "RF Bulk Acoustic Wave Filters For Communications," *Artech House*, 2019.

[4] M. Ueda, and Y. Satoh, "FBAR and SAW Technologies and Their Applications for Mobile Communications," *Asia-Pacific Microwave Conference Workshops & Short Courses Digest*, p. 426, 2006.

[5] R. Aigner, et al., "BAW Filters for 5G Bands," *2018 IEEE International Electron Devices Meeting (IEDM)*, pp. 14.5.1-14.5.4, 2018.

[6] K. M. Lakin, J. S. Wang, G. R. Kline, A. R. Landin, Y. Y. Chen and J. D. Hunt, "Thin Film Resonators and Filters," *1982 Ultrasonics Symposium*, San Diego, CA, USA, 1982, pp. 466-475, doi: 10.1109/ULTSYM.1982.197870.

[7] R. Ruby, "Review and Comparison of Bulk Acoustic Wave FBAR, SMR Technology," *Proc. IEEE Ultrasonics Symp*, p. 1029, 2007.

[8] A. Hagelauer et al., "From Microwave Acoustic Filters to Millimeter-Wave Operation and New Applications," *IEEE Journal of Microwaves*, vol. 3, no. 1, pp. 484-508, Jan. 2023, doi: 10.1109/JMW.2022.3226415.

[9] A. Tag et al., "Next Generation Of BAW: The New Benchmark for RF Acoustic Technologies," *2022 IEEE International Ultrasonics Symposium (IUS)*, Venice, Italy, 2022, pp. 1-4, doi: 10.1109/IUS54386.2022.9958625.

[10] A. Hagelauer, G. Fattinger, C. C. W. Ruppel, M. Ueda, K. -y. Hashimoto and A. Tag, "Microwave Acoustic Wave Devices: Recent Advances on Architectures, Modeling, Materials, and Packaging," *IEEE Transactions on Microwave Theory and Techniques*, vol. 66, no. 10, pp. 4548-4562, Oct. 2018, doi: 10.1109/TMTT.2018.2854160.

[11] R. Aigner, M. Handtmann, US patent US2006/0290446 A1, December 28, 2006.

[12] W. P. Mason, “Physical Acoustics and the Properties of Solids,” *Van Nostrand*, 1958.

[13] D. Royer, and E. Dieulesaint, ”Elastic waves in solids: Free and Guided Propagation,” *Springer Science and Business Media*, Vol. 1, 1999.

[14] D. A. Berlincourt, D. R. Curran, and H. Jaffe, ”Piezolelectric and Piezomagnetic Materials and Their Function in Transducers,” *Physical Acoustics*, Vol. 1-A, ed. W.P. Mason, Academic Press, New York, 1964.

[15] R. Thalhammer, G. Fattinger, M. Handtmann and S. Marksteiner, ”Ohmic effects in BAW-resonators,” *2006 IEEE MTT-S International Microwave Symposium Digest*, pp. 390-393, 2006.

[16] H. B. Callen, ”Thermodynamics and an Introduction to Thermostatistics,” *John Wiley & Sons*, 2nd Edition, 1985.

[17] R. Aigner, N. -H. Huynh, M. Handtmann and S. Marksteiner, ”Behavior of BAW devices at high power levels,” *IEEE MTT-S International Microwave Symposium Digest*, 2005., Long Beach, CA, USA, 2005, pp. 429-432, doi: 10.1109/MWSYM.2005.1516620.

[18] E. Rocas, C. Collado, J. Mateu, N. D. Orloff, J. C. Booth and R. Aigner, ”Electro-thermo-mechanical model for bulk acoustic wave resonators,” *IEEE Transactions on Ultrasonics, Ferroelectrics, and Frequency Control*, Vol. 60, No. 11, pp. 2389-2403, 2013.

[19] Feld, D. A., R. Parker, R. Ruby, P. Bradley and S. Dong, ”After 60 years: A new formula for computing quality factor is warranted,” *2008 IEEE Ultrasonics Symposium*, pp. 431-436, 2008.

[20] D. Kajfez and W. P. Wheless, ”Invariant Definitions of the Unloaded Q Factor (Short Paper),” in *IEEE Transactions on Microwave Theory and Techniques*, vol. 34, no. 7, pp. 840-841, Jul 1986, doi: 10.1109/TMTT.1986.1133452.

[21] R. Jin, Z. Cao, M. Patel, B. Abbott, D. Molinero and D. Feld, ”An Improved Formula for Estimating Stored Energy in a BAW Resonator by its Measured S11 Parameters,” *2021 IEEE International Ultrasonics Symposium* (IUS), Xi’an, China, 2021, pp. 1-5, doi: 10.1109/IUS52206.2021.9593620.

[22] J. F. Rosenbaum, ”Bulk Acoustic Wave Theory and Devices”, *Artech House*, 1988.

[23] K. S. Van Dyke, ”The Piezo-Electric Resonator and Its Equivalent Network,” *Proceedings of the Institute of Radio Engineers*, Vol. 16, no. 6, pp. 742-764, 1928.

[24] J. D. Larson, P. D. Bradley, S. Wartenberg and R. C. Ruby, ”Modified

Butterworth-Van Dyke circuit for FBAR resonators and automated measurement system," *2000 IEEE Ultrasonics Symposium. Proceedings. An International Symposium*, Vol. 1, pp. 863-868, 2000.

[25] W. P. Mason, W.P. "Piezoelectric Crystals and Their Application to Ultrasonics," *Van Nostrand*, 1950.

[26] C. Hakoda, J. Rose, P. Shokouhi, and C. Lissenden , "Using Floquet periodicity to easily calculate dispersion curves and wave structures of homogeneous waveguides," in *AIP Conference Proceedings 1949*, 020016, 2018, doi: 10.1063/1.5031513.

[27] T. Makkonen, A. Holappa, J. Ella and M. M. Salomea, "Finite element simulations of thin-film composite BAW resonators," in *IEEE Transactions on Ultrasonics, Ferroelectrics, and Frequency Control*, vol. 48, no. 5, pp. 1241-1258, Sept. 2001, doi: 10.1109/58.949733.

[28] R. K. Thalhammer, J. D. Larson, III, "Finite-Element Analysis of Bulk-Acoustic-Wave Devices: A Review of Model Setup and Applications," in *IEEE Transactions on Ultrasonics, Ferroelectrics, and Frequency Control*, Vol. 63, No. 10, pp. 1624-1635.

[29] T. Jamneala, P. Bradley, U. B. Koelle and A. Chien, "Modified Mason model for bulk acoustic wave resonators," in *IEEE Transactions on Ultrasonics, Ferroelectrics, and Frequency Control*, vol. 55, no. 9, pp. 2025-2029, September 2008, doi: 10.1109/TUFFC.893.

[30] C. Collado, E. Rocas, J. Verdú, J. Mateu, A. Hueltes and R. Aigner, "A lateral modes model for BAW resonators" *2014 IEEE International Ultrasonics Symposium*, Chicago, IL, 2014, pp. 1497-1500.

[31] T. Jamneala, P. Bradley, A. Shirakawa, R. K. Thalhammer and R. Ruby, "An Investigation of Lateral Modes in FBAR Resonators," in *IEEE Transactions on Ultrasonics, Ferroelectrics, and Frequency Control*, vol. 63, no. 5, pp. 778-789, May 2016, doi: 10.1109/TUFFC.2016.2531744.

[32] T. Jamneala, C. Kirkendall, B. Ivira, R. K. Thalhammer, P. Bradley and R. Ruby, "The Main Lateral Mode Approximation of a Film Bulk Acoustic Resonator With Perfect Metal Electrodes," in *IEEE Transactions on Ultrasonics, Ferroelectrics, and Frequency Control*, vol. 65, no. 9, pp. 1703-1716, Sept. 2018, doi: 10.1109/TUFFC.2018.2846559.

[33] J. W. Strutt, (3rd Baron Rayleigh), "On the Free Vibrations of an Infinite Plate of Homogeneous Isotropic Elastic Matter," *Proc. London Math. Soc.*, Vol. 20, p. 225, 1889.

[34] H. Lamb, "On Waves in an Elastic Plate," *Proc. Roy. Soc. London*, Ser. A 93, pp. 114-128, 1917.

[35] B. A. Auld, "Acoustic Fields and Waves in Solids," *Wiley-Interscience*, Vol. II, 1973.

[36] R. Marks, A. Clarke, C. Featherston, C. Paget, and R. Pullin, "Lamb Wave Interaction with Adhesively Bonded Stiffeners and Disbonds Using 3D Vibrometry," *Applied Sciences*, Vol. 6, no. 6, p. 12, Jan. 2019.

[37] Clorennec, Dominique, Prada, Claire, Royer, Daniel. (2007). Local and noncontact measurements of bulk acoustic wave velocities in thin isotropic plates and shells using zero group velocity Lamb modes. *Journal of Applied Physics*. 101. 034908 - 034908. 10.1063/1.2434824.

[38] G. G. Fattinger, S. Marksteiner, J. Kaitila, and R. Aigner, "Optimization of Acoustic Dispersion for High Performance Thin Film BAW Resonators," *Procedings of IEEE Ultrasonics Symposium 2005*, Rotterdam.

[39] W. Shockley, D. R. Curran, and D. A. Koneval, "Energy Trapping and Related Studies of Multiple Electrode Filter Crystals," *IEEE Frequency Control Symp. Proceedings*, pp. 88-126, 1963.

[40] W. Shockley, D. R. Curran, and D. A. Koneval, "Trapped-Energy Modes in Quartz Filter Crystals," *Journal of the Acoustical Society of America*, No. 41, pp. 981-993, 1967.

[41] R. Ruby, J. Larson, C. Feng, and S. Fazzio, "The Effect of the Perimeter Geometry on FBAR Resonator Electrical Performance," *Proc. IEEE Internationsl Microwave Symposium*, 2005.

[42] J. Kaitila, M. Ylilammi and R. Aigner, "Spurious Resonance Free Bulk Accoustic Wave Resonators," *Proc. IEEE Ultrasonics Symposium*, 2005.

[43] T. Pensala, and M. Ylilammi, "Spurious Resonance Suppression in Gigahertz-Range ZnO Thin-Film Bulk Acoustic Wave Resonators by the Boundary Frame Method: Modeling and Experiment," *IEEE Transactions on Ultrasonics, Ferroelectrics, and Frequency Control*, Vol. 56, No. 8, pp. 1731-1744, 2009.

[44] C. Udaondo, C. Collado, J. Mateu and R. Aigner, "Analysis of Border Ring Modes on SMR-BAW Resonators," in *2019 IEEE International Ultrasonics Symposium (IUS)*, 2019, pp. 1703-1706, doi: 10.1109/ULTSYM.2019.8925601

[45] D. A. Feld, D. S. Shim, S. Fouladi and F. Bayatpur, "Advances in nonlinear measurement & modeling of bulk acoustic wave resonators (invited)," *2014 IEEE International Ultrasonics Symposium*, Chicago, IL, 2014, pp. 264-272.

[46] T. Yang, Z. Cao and D. A. Feld, "An H2 emissions model for piezoelectric devices exhibiting strong lateral mode resonances," *2017 IEEE International Ultrasonics Symposium (IUS)*, Washington, DC, 2017, pp. 1-7.

[47] C. Collado et al., ”Nonlinear Effects of SiO2 Layers in Bulk Acoustic Wave Resonators,” in *IEEE Transactions on Microwave Theory and Techniques*, vol. 66, no. 4, pp. 1773-1779, April 2018, doi: 10.1109/TMTT.2017.2783377.

[48] D. S. Shim and D. A. Feld, ”A general nonlinear Mason model of arbitrary nonlinearities in a piezoelectric film,” *2010 IEEE International Ultrasonics Symposium*, San Diego, CA, 2010, pp. 295-300.

[49] D. Garcia-Pastor, C. Collado, J. Mateu and R. Aigner, ”Third-Harmonic and Intermodulation Distortion in Bulk Acoustic-Wave Resonators,” in *IEEE Transactions on Microwave Theory and Techniques*, vol. 68, no. 4, pp. 1304-1311, April 2020, doi: 10.1109/TMTT.2019.2955135.

[50] C. Udaondo, C. Collado and J. Mateu, ”Fast modeling of lateral modes in BAW resonators with arbitrary in-plane geometry,” in *2022 IEEE International Ultrasonics Symposium (IUS)*, 2022, pp. 1-4, doi: 10.1109/IUS54386.2022.9957924.

[51] D. Royer, E. Dieulesaint, “Elastic Waves in Solids II, Generation, Acousto-optic Interaction, Applications”, Springer, 2000.

[52] C. Christopoulos, The Transmission Line Modeling Method: TLM, Piscataway, NY, IEEE Press, 1995.

[53] W. J. R. Hoefer, ”The Transmission-Line Matrix Method - Theory and Applications,” in *IEEE Transactions on Microwave Theory and Techniques*, vol. 33, no. 10, pp. 882-893, Oct. 1985, doi: 10.1109/TMTT.1985.1133146.

[54] J. R. Whinnery, C. Concordia, W. Ridgway and G. Kron, ”Network Analyzer Studies of Electromagnetic Cavity Resonators,” in *Proceedings of the IRE*, vol. 32, no. 6, pp. 360-367, June 1944, doi: 10.1109/JRPROC.1944.231734

[55] C. Udaondo, C. Collado and J. Mateu, ”Fast Analysis of Border Ring Suppression on BAW Resonators,” *2023 IEEE International Ultrasonics Symposium (IUS)*, Montreal, QC, Canada, 2023, pp. 1-4, doi: 10.1109/IUS51837.2023.10306477.

[56] A. Tajic, A. Volatier, R. Aigner and M. Solal, ”Simulation of solidly mounted BAW resonators using FEM combined with BEM and/or PML,” *2010 IEEE International Ultrasonics Symposium*, San Diego, CA, USA, 2010, pp. 181-184, doi: 10.1109/ULTSYM.2010.5935769.

[57] K. Kokkonen, J. Meltaus, T. Pensala and M. Kaivola, ”Measurement of evanescent wave properties of a bulk acoustic wave resonator [Letters],” in *IEEE Transactions on Ultrasonics, Ferroelectrics, and Frequency Control*, vol. 59, no. 3, pp. 557-559, March 2012, doi: 10.1109/TUFFC.2012.2228.

[58] C. Kittel, “Introduction to Solid State Physics,” 7th ed., *NY: Wiley*, 1996.

[59] R. W. Powell, C. Y. Ho, and P. E. Liley, “Thermal Conductivity of Selected Ma-

terials," *National Standard Reference Data Series – National Bureau of Standards – 8*, 1966.

[60] E. Rocas, et al., "Performance of BAW resonators at cryogenic temperatures," *2013 IEEE International Ultrasonics Symposium (IUS)*, pp. 1672-1675, 2013.

[61] N. D. Orloff et al., "A Compact Variable-Temperature Broadband Series-Resistor Calibration," in *IEEE Transactions on Microwave Theory and Techniques*, vol. 59, no. 1, pp. 188-195, Jan. 2011, doi: 10.1109/TMTT.2010.2091200.

[62] R. Jin, Z. Cao, Y. He, B. Jiang and D. Feld, "A Procedure to Correct for Anomalies in Estimating the Time Averaged Stored Energy of a BAW Resonator from its S11 Parameters," *2022 IEEE International Ultrasonics Symposium (IUS)*, Venice, Italy, 2022, pp. 1-5, doi: 10.1109/IUS54386.2022.9957551.

[63] D. M. Pozar, "Microwave Engineering," 4th ed., *Wiley*, 2001.

ij

Appendix A

Calculation of the temperature coefficient of stress by the thermal expansion

In Chapter 2, the temperature coefficient of stress at constant electric displacement λ_i^{SD} appeared on the constitutive relations. Since the λ_i^{SD} values for different materials are not found on literature, and is not possible to measure it with our resources, a theoretical approximation from known parameters needs to be done.

In order to get the λ_i^{SD} values from the thermal expansion, the constitutive relations need to be derived from the Gibbs function (with T, E, and Θ as independent variables). The following constitutive relations are obtained (the entropy equation will be omitted since it is not necessary for this procedure):

$$S_i = s_{ij}^{E\Theta} T_j - d_{ik}^{\Theta} E_k - \alpha_i^E d\Theta \tag{A.1}$$

$$D_l = d_{lj}^{\Theta} T_j + \varepsilon_{lk}^{T\Theta} E_k + p_l^T d\Theta. \tag{A.2}$$

From these expressions we will get T as an independent variable:

$$T_i = \frac{1}{s_{ij}^{E\Theta}} S_j - \frac{d_{ik}^{\Theta}}{s_{ij}^{E\Theta}} E_k - \lambda_i^E d\Theta \tag{A.3}$$

$$D_l = \frac{d_{lj}^{\Theta}}{s_{ij}^{E\Theta}} S_j + \left(\varepsilon_{lk}^{T\Theta} - \frac{d_{lk}^{\Theta^2}}{s_{ij}^{E\Theta}} \right) E_k + \left(p_i^T - \frac{d_{lj}^{\Theta} \alpha_3^E}{s_{ij}^{E\Theta}} \right) d\Theta. \tag{A.4}$$

knowing that $c_{ij}^{E\Theta} \equiv \dfrac{1}{s_{ij}^{E\Theta}}$, and $d_{nj}^{\Theta} \equiv \dfrac{e_{ni}^{\Theta}}{c_{ij}^{E\Theta}}$, expressions A.3 and A.4 can be simplified to

$$T_i = c_{ij}^{E\Theta} S_j - e_{ik}^{\Theta} E_k - \lambda_i^E d\Theta \tag{A.5}$$

$$D_l = e_{lj}^{\Theta} S_j + \varepsilon_{lk}^{S\Theta} E_k + p_l^S d\Theta, \tag{A.6}$$

where $\varepsilon_{nm}^{S\Theta} = \varepsilon_{nm}^{T\Theta} - \dfrac{e_{ni}^{\Theta} e_{mj}^{\Theta}}{c_{ji}^{E\Theta}}$, $\lambda_i^E = c_{ij}^{E\Theta} \alpha_j^E$, and $p_i^S = p_i^T - e_{ij}^{\Theta} \alpha_j^E$.

As done in Chapter 2, D is needed as an independent variable too, leading to the following constitutive relations

$$T_i = c_{ij}^{D\Theta} S_j - h_{ik}^{\Theta} D_k - \lambda_i^D d\Theta \tag{A.7}$$

$$E_l = \beta_{lk}^{S\Theta} D_k - h_{lj}^{\Theta} S_j - p_l^{SD} d\Theta, \tag{A.8}$$

with the following constants: $h_{nj}^{\Theta} = \dfrac{e_{mj}^{\Theta}}{\varepsilon_{mn}^{S\Theta}}$, $c_{ij}^D = c_{ij}^E + e_{mj}^{\Theta} h_{mi}^{\Theta}$, $\lambda_i^{SD} = \lambda_i^E - p_m^{SE} h_{mi}^{\Theta}$, $p_i^{SD} = \dfrac{p_i^S}{\varepsilon_{ij}^{S\Theta}}$, and $\beta_{ij}^{S\Theta} = \dfrac{1}{\varepsilon_{ij}^{S\Theta}}$. This λ_i^{SD} expression is the one used in Section 4.1.1 to derive the relation between λ and α.

Appendix B

Temperature coefficient of stress on different class crystals

The temperature coefficient of stress can be calculated as

$$\lambda_3^{SD} = \alpha_1 c_{13}^{E\Theta} + \alpha_2 c_{23}^{E\Theta} + \alpha_3 c_{33}^{E\Theta} + \alpha_4 c_{43}^{E\Theta} + \alpha_5 c_{53}^{E\Theta} + \alpha_6 c_{63}^{E\Theta}. \tag{B.1}$$

Assuming that thermal expansion α_i is equal in each direction and applying the stiffness tensors for hexagonal (B.2) and isotropic crystals (B.3) [13]:

$$\begin{pmatrix} c_{11} & c_{12} & c_{13} & 0 & 0 & 0 \\ c_{12} & c_{11} & c_{13} & 0 & 0 & 0 \\ c_{13} & c_{13} & c_{33} & 0 & 0 & 0 \\ 0 & 0 & 0 & c_{44} & 0 & 0 \\ 0 & 0 & 0 & 0 & c_{44} & 0 \\ 0 & 0 & 0 & 0 & 0 & \dfrac{c_{11} - c12}{2} \end{pmatrix} \tag{B.2}$$

$$\begin{pmatrix} c_{11} & c_{12} & c_{12} & 0 & 0 & 0 \\ c_{12} & c_{11} & c_{12} & 0 & 0 & 0 \\ c_{12} & c_{12} & c_{11} & 0 & 0 & 0 \\ 0 & 0 & 0 & \dfrac{c_{11}-c12}{2} & 0 & 0 \\ 0 & 0 & 0 & 0 & \dfrac{c_{11}-c12}{2} & 0 \\ 0 & 0 & 0 & 0 & 0 & \dfrac{c_{11}-c12}{2} \end{pmatrix}, \tag{B.3}$$

we end up with the following expression for calculating the thermal stress in the thickness direction:

$$\lambda_3^{SD} = \alpha_1 c_{13}^{E\Theta} + \alpha_2 c_{13}^{E\Theta} + \alpha_3 c_{33}^{E\Theta} = \alpha_1 \left(c_{33}^{E\Theta} + 2c_{13}^{E\Theta} \right). \tag{B.4}$$